Karlsruhe Institute of Technology

Efficiency Studies of the Background Suppression by a Liquid-Nitrogen Cooled Baffle System in the KATRIN Experiment

Master's Thesis of

Florian Robin Müller
born 7 May 1989 in Villingen-Schwenningen

At the Department of Physics
Institute for Experimental Nuclear Physics
Karlsruhe Institute of Technology

Reviewer:	Prof. Dr. Guido Drexlin
Second reviewer:	Prof. Dr. Thomas Müller
Advisor:	Dr. Klaus Schlösser

Submission Date: 16 June 2015

I declare that I have developed and written the enclosed thesis completely by myself, and have not used sources or means without declaration in the text.

Karlsruhe, 16 June 2015

. . . . . .

(Florian Müller)

Zusammenfassung

Die Beobachtung von Neutrino-Oszillationen lässt den Schluss, dass Neutrinos eine endliche Masse haben, zu. Dies hat weitreichende Konsequenzen in der Kosmologie und auch für Modelle, die die Masse von Elementarteilchen erklären. Die Kenntnis der absoluten Neutrinomasse erlaubt es diese Modelle einzuschränken. Deshalb ist es wichtig, die absolute Massenskala der Neutrinomasse direkt und modell-unabhängig zu bestimmen. Die Neutrinomassen-Experimente in Mainz und Troitsk haben die beste obere Grenze der Neutrinomasse in den 1990er Jahren bestimmt $m_{\bar{\nu}_e} < 2\,\mathrm{eV/c^2}$. Beide nutzen MAC-E[1] Filter zur Energiebestimmung.

Das **Ka**rlsuher **Tr**itium **N**eutrino (KATRIN) Experiment ist ihr Nachfolge-Experiment und benutzt einen MAC-E Filter mit unerreichter Genauigkeit. Die Sensitivität soll auf $m_{\bar{\nu}_e} < 0.2\,\mathrm{eV/c^2}$ ($90\,\%$C.L.) erhöht werden. Diese ambitionierte Zielsetzung erfordert insbesondere einen niedrigen Untergrund von weniger als 1 Ereignis in 100 Sekunden ($10\,\mathrm{mcps}$). Ein Teil des vorhandenen Untergrundes wird von Elektronen, die bei dem α-Zerfall von Radon entstehen, verursacht. Die NEG[2] Drähte, welche den Druck im Spektrometer auf den Ultrahochvakuumbereich reduzieren, ($10^{-11}\,\mathrm{mbar}$) wurden als Quelle von $^{219}\mathrm{Rn}$ identifiziert. Außerdem ist es möglich, dass zusätzlich $^{220}\mathrm{Rn}$ von den Schweißnähten des Hauptspektrometers emaniert. Um diesen Untergrund zu reduzieren, wurden mit flüssigem Stickstoff gekühlte Kupfer-Baffles in das Spektrometer eingebaut. Sie fungieren als Kühlfalle, was zu einer Reduktion der Radon-Zerfälle im sensitiven Flussschlauchvolumen führt. Da die mittlere Verweildauer des Radon-Atoms auf dem Baffle stark temperaturabhängig ist, sind über lange Zeit stabile tiefe Betriebstemperaturen erforderlich, um das Baffle effizient als Kühlfalle für Radon betreiben zu können.

Im Rahmen dieser Arbeit wurde das System, das die Baffle mit flüssigem Stickstoff versorgt für den Betrieb bei $18.6\,\mathrm{keV}$ einsatzbereit gemacht. Des Weiteren, wurde die Abhängigkeit der Unterdrückungseffizienz von Radon-induziertem Untergrund von der mittleren Verweildauer simuliert. Abschließend wurden Messungen der Unterdrückungseffizienz des Radon-induzierten Untergrundes durch die stickstoffgekühlten Kupfer-Baffles ausgewertet.

In Kapitel 3 werden die Hochspannungs-Trenner für die Stickstoffversorgung der Baffles wurden erfolgreich in den Aufbau des Spektrometers integriert. Damit ist es möglich die Kupfer-Baffles auch während Hochspannungsmessungen bis $-18.6\,\mathrm{kV}$ kontinuierlich mit flüssigem Stickstoff zu kühlen.

In Kapitel 4 wird die Numerische Simulation und die Monte-Carlo-Simulation erlauben es, den

[1] **M**agnetic **A**diabatic **C**ollimation combined with an **E**lectrostatic
[2] **N**on-**E**vaporable **G**etter

Einfluss der mittleren Verweildauer auf die Unterdrückungseffizienz von Radon durch die Baffles zu untersuchen. Die beiden Modelle liefern vergleichbare Ergebnisse.

In Kapitel 5 wurde die Unterdrückungseffizienz von Radon-induziertem Untergrund durch stickstoffgekühlte Kupfer-Baffles untersucht. Hierfür wurden während der zweiten SDS[3] Inbetriebsetzung sowohl Untergrundmessungen als auch Messungen mit einer zusätzlichen $^{220}\mathrm{Rn}$ Radon-Quelle bei erhöhtem Druck ($10^{-8}\,\mathrm{mbar}$) vorgenommen. Dies erlaubt es den Radon-induzierten Untergrund von anderen Einflüssen zu trennen. Die NEG-Drähte sind die dominante Quelle von Radon im Hauptspektrometer. Außerdem ist der verbleibende Radon-induzierte Untergrund bei erhöhtem Druck $(27 \pm 3)\,\mathrm{mcps}$. Außerdem verbleibt ein Untergrund von $(564 \pm 2)\,\mathrm{mcps}$, der nicht auf Radon zurückzuführen ist. Die Identifizierung und Entfernung dieses Untergrundes ist von außerordentlicher Bedeutung. Im Moment untersucht die KATRIN-Gruppe, ob Wasserstoff-Atome in hochangeregten Rydberg-Zuständen die Ursache dieses Untergrundes sind. Die Messungen mit einer zusätzlichen Radon-Quelle bestätigen den von den Simulationen bereits erwarteten Zusammenhang zwischen Temperatur und Unterdrückungsrate.

Der Vergleich zwischen Simulationen und Messergebnissen zeigt nur geringe Abweichungen unter der Annahme einer mittleren Verweildauer von $(60 \pm 20)\,\mathrm{s}$. Diese Übereinstimmung bestätigt insbesondere die Korrektheit der Simulationen.

[3] **S**pectrometer and **D**etector **S**ection

Abstract

With the observation of neutrino oscillations it was established that neutrinos are not massless. This has not only far-reaching consequences for cosmology but also for the nature of mass as the neutrino mass is small compared to the masses of other elementary particles. The absolute neutrino mass allows to restrict mass models. Therefore, it is of importance to determine the absolute neutrino-mass scale in a direct and model-independent way. To date, the best upper limits are given by experiments performed in Mainz and Troitsk in the 1990s: $m_{\bar{\nu}_e} < 2\,\mathrm{eV/c^2}$. Both utilised the MAC-E[4] filter technique.

The **Ka**rlsruhe **Tri**tium **N**eutrino (KATRIN) experiment is their successor and utilises a spectrometer based on the MAC-E filter technique with unprecedented accuracy. Its goal is the improvement of the sensitivity to $m_{\bar{\nu}_e} < 0.2\,\mathrm{eV/c^2}$ (90 %C.L.). This ambitious goal requires, in particular, a background level lower than 0.01 events per second. A part of the currently observed background originates from electrons accompanying the α-decay of radon. The NEG[5] strips which provide the required ultra-high vacuum ($10^{-11}\,\mathrm{mbar}$) in the spectrometer have been identified as a source for $^{219}\mathrm{Rn}$. Moreover, it is possible that the welds of the spectrometer emanate $^{220}\mathrm{Rn}$. In order to suppress this background liquid-nitrogen cooled copper baffles have been incorporated in the KATRIN design. They are able to cryosorb radon, thus, reducing the fraction of radon decays in the sensitive spectrometer volume. The mean desorption time is dominated by the operating temperature which makes liquid-nitrogen temperatures under stable long-term conditions necessary.

In the scope of this thesis the liquid-nitrogen supply system was implemented for permanent operation at high voltage of up to $-18.6\,\mathrm{kV}$. Secondly, simulations which study the dependency of the radon suppression of the mean desorption time are investigated. Lastly, measurements of the suppression efficiency of the radon-induced background by the liquid-nitrogen cooled copper baffles are evaluated.

In chapter 3 the technical setup of the high-voltage separators of the liquid-nitrogen supply system for the baffles is discussed. It is shown that they were implemented successfully for retarding potentials of up to $-18.6\,\mathrm{kV}$. This allows continuous high-voltage measurements with the baffle system operating at liquid-nitrogen temperatures.

In chapter 4 simulations and analyses of the radon-induced background and its suppression are evaluated. The Numerical Simulation and the test-particle Monte-Carlo simulation allow to study the dependency of the suppression efficiency on the mean desorption time. The models yield similar results.

[4] **M**agnetic **A**diabatic **C**ollimation combined with an **E**lectrostatic

[5] **N**on-**E**vaporable **G**etter

In chapter 5 the suppression efficiency of radon-induced backgrounds by the liquid-nitrogen cooled copper baffles is studied. During the second SDS[6] commissioning phase both background measurements and measurements with an additional $^{220}\mathrm{Rn}$ source were taken at elevated pressures ($10^{-8}\,\mathrm{mbar}$). This allows to separate radon-induced backgrounds from other background components.

It is shown that the dominant radon source are the NEG strips mounted in the pump ports of the spectrometer. Furthermore, the maximal suppression of radon-induced decays is $97^{+2}_{-3}\,\%$ with two of three getters integrated into the system. The remaining radon-induced background is $(27 \pm 3)\,\mathrm{mcps}$ which is still a factor of 3 more than the design limit. At elevated pressure the remaining background which does not originate from radon is $(564 \pm 2)\,\mathrm{mcps}$. The identification of this background is of the utmost importance. At the moment hydrogen atoms excited into high-energetic Rydberg states are considered by the KATRIN collaboration. The measurements with an additional radon source confirm the expected characteristics of the cryosorption. Lastly, a comparison between the simulations and the analysis shows little deviations for desorption times on the order of $(60 \pm 20)\,\mathrm{s}$.

[6] **S**pectrometer and **D**etector **S**ection

Contents

List of Figures

List of Tables

1. Neutrino Physics

This chapter is a short overview of the field of neutrino physics. Firstly, the discovery of radioactivity, the postulation of the neutrino by Pauli and its discovery are discussed (see section 1.1). Secondly, neutrino oscillations are explained and the consequences for neutrino masses are discussed (section 1.3). As the mass is still unknown, experiments try to determine the neutrino mass with different approaches (see section 1.4). This thesis is a part of one of these experiments, the KATRIN experiment.

1.1 Radioactivity and the discovery of the neutrino

1.1.1 Discovery of the β-decay

The discovery of radioactivity by Antoine Henry Becquerel in 1896 followed up by research of Marie and Pierre Curie earned them a Nobel Prize in 1903 [Nob03]. Soon, Ernest Rutherford discerned two dissimilar kinds of radioactivity due to different penetration depths and ionization characteristics and labelled them α- and β-decay [Rut99]. Furthermore, Becquerel discovered that the particles emitted by β-decays are electrons [Bec00]. Eventually, Soddy and Fajans discovered the transition of the parent radionuclide to another element during decays [Sod13] [Faj13]. When all this knowledge is put together a first concept for β-decays can be established:

$$ {}^{A}_{Z}X \rightarrow {}^{A}_{Z+1}Y + e^{-}. \tag{1.1} $$

1.1.2 Postulate of the neutrino

However this formula is not complete yet since the β-decay has a continuous spectrum [Cha14]. This is a huge problem because energy and momentum conservation demand that the energy of the electron should be discrete for a decay into one additional particle. Furthermore, the angular momentum is not conserved either. The ensuing three decades of discussion included the correct solution by Pauli in 1930. As a desperate way out of this dilemma, he proposed the existence of an additional spin-$\frac{1}{2}$-particle that is produced during the β-decay and is not detected easily [Pau30].

$$ {}^{A}_{Z}X \rightarrow {}^{A}_{Z+1}Y + e^{-} + \bar{\nu_e} \tag{1.2} $$

This allows both energy conservation and a continuous spectrum of the electron because of the kinematics of the decay into three particles. Neutrino, the final name for this new particle, was popularised by Fermi which means the little neutron. Fermi also formulated a theory describing the interaction as a point-like interaction between four fermions. He also discussed the mass of the neutrino and concluded that its mass is small and assumed that it vanishes [Fer34]. The very low probability of neutrino interactions makes the direct detection of neutrinos very challenging [BP34].

1.1.3 Evidence of neutrinos

The electron-anti-neutrino

The technological progress during the Second World War included the development of a novel technology: the development of nuclear reactors by Fermi, Szilárd and co-workers [Fer46]. This opened up new possibilities to detect neutrinos originating from the abundance of nuclear decays in the reactor. As a means to detect neutrinos the detector was shielded against other particles originating from the reactor. The Hanford experiment by Cowan and Reines was promising but despite the good suppression of background originating from the reactor, the signal was superimposed by background due to cosmic particles [RC97]. So Cowan and Reines began to work on project Poltergeist which included a measurement technique to get rid of the cosmological background [RC97]. Their setup is based on the detection of inverse beta decay via the interaction with a proton:

$$\mathrm{p} + \bar{\nu_e} \rightarrow \mathrm{n} + \mathrm{e}^+ \tag{1.3}$$

Their setup is based on three chambers filled with liquid scintillator. There were water tanks between those chambers in which cadmium chloride was dissolved. The general detection process consists of three steps:

- The incoming neutrinos interacts with the hydrogen in water because the two hydrogen atoms of a water molecule have a comparatively large cross section for neutrino reactions.
- The produced positron (e^+) annihilates with an electron within a fraction of a microsecond and produces two mono-energetic γ-rays which are detected via the scintillators at the top and the bottom of the water tank. If they arrive less than $0.2\,\mu\mathrm{s}$ apart and match the expected energy (between 200 and $600\,\mathrm{keV}$) they are accepted as signal and the search for a neutron capture is initiated for $30\,\mu\mathrm{s}$.
- Cadmium has a high cross section for neutron capture. This process results in an excited state. The disexcitation is accompanied by the emission of several γ rays which are again detected by the scintillators.

With this setup it was finally possible to gain a sufficient signal to background ratio and to prove the existence of the neutrino.

The myon-neutrino and the tau-neutrino

The myon-neutrino ν_μ was first postulated in the early 1940s (as neutretto) [AH38]. It was discovered in 1962 by Ledermann, Steinberger and Schwartz at the Alternating Gradient Synchrotron (AGS) [Dan62].

After the discovery of the τ in 1975 by [Per75] the existence of the τ-neutrino ν_τ was already implied. The evidence for τ-neutrinos was found with the DONUT-experiment at the Tevatron [Kod01].

1.2 Neutrinos in the standard model

The standard model (SM) uses relativistic quantum field theory to describe the composition and interaction of matter and is based on the idea of indivisible elementary particles. It incorporates three of the fundamental interactions: the strong, the electromagnetic and the weak interaction but fails to include the gravitation. The elementary particles can be divided into gauge bosons and fermions. Gauge bosons are the carriers of the interactions: The gluon (g) transfers the strong force between particles with colour, the photon (γ) transfers the electromagnetic force between charged particles, and the $\mathrm{W}^\pm$ and the Z^0 transfer the weak interaction between fermions. Fermions can be

separated into quarks and leptons based on the interactions in which they can participate. Quarks behave according to both the strong and the electroweak interaction while the leptons only interact via the electro-weak interaction. Additionally, there are corresponding antiparticles for all fermions. In order to allow for non-zero masses of the gauge bosons $\mathrm{W}^{\pm}$ and Z^0 the Higgs mechanism was introduced [And63] [Hig64] [EB64] [Gur64]. This theory includes the prediction of (at least) one massive scalar boson - the Higgs boson. A candidate with mass $(125.6 \pm 0.3)\,\mathrm{keV}$ was found with the detectors CMS and ATLAS at the LHC [Ber12].

In the standard model the neutrinos ν_e, ν_μ and ν_τ are included as massless, uncharged fermions with spin $\frac{1}{2}\hbar$ which can only interact via the weak interaction. Neutrinos have a helicity h which describes the orientation of the spin relative to the momentum. The helicity of neutrinos was first measured by Goldhaber to be $h = -1.0 \pm 0.3$ [Gol58]. In fact all experiments performed are consistent with $h = -1$ for neutrinos and $h = +1$ for antineutrinos [Pov14].

$$h = \frac{\vec{s} \cdot \vec{p}}{|\vec{s}| \cdot |\vec{p}|} = \begin{cases} -1, & \nu \\ +1, & \bar{\nu} \end{cases} \tag{1.4}$$

If the neutrino was massive a reference system could be found in which the direction of the momentum would be opposite and thus helicity would change its sign. Only for particles with very small or even vanishing masses the occurrence of only one helicity is expected. Since Goldhaber found only one helicity the neutrino mass was assumed to be zero. Based on these findings a the V-A-theory was developed which was later incorporated into the SM [FGM58].

Furthermore, there is no additional SM fourth neutrino with a mass $m_\nu < \frac{m(Z^0)}{2}$ which can interact via the weak interaction. The reason is the width of the Z^0-peak measured by ALEPH which constricts the neutrino number to 2.9840 ± 0.0082 [ALE06]. However, the SM neutrinos have one flaw: Neutrino oscillations have proven that they have mass.

1.3 Discovery of neutrino oscillations

Neutrino oscillations have been first discussed by Pontecorvo [Pon57]. Proof of this theory however was difficult. A first indication of neutrino oscillations were the discrepancies between the data taken at Homestake and the calculations from the solar model. Neutrino oscillations were first observed by detecting atmospheric neutrinos at Super-Kamiokande. In order to allow for neutrino oscillations neutrinos need to have mass. This implies that the minimal SM is not correct and has to be modified. These modifications may lead to new physics such as the addition of particles or dimensions.

1.3.1 A model for neutrino oscillations

The first model for neutrino oscillations was developed by Maki, Nakagawa and Sakata [Mak62]. Their concept is based on the idea that the eigenstates of the weak interaction ν_e,ν_μ and ν_τ are not equal to the mass eigenstates ν_1,ν_2 and ν_3. They proposed that the eigenstates of the weak interaction are admixtures of the mass eigenstates:

$$\begin{pmatrix} \nu_e \\ \nu_\mu \\ \nu_\tau \end{pmatrix} = U \cdot \begin{pmatrix} \nu_1 \\ \nu_2 \\ \nu_3 \end{pmatrix} \tag{1.5}$$

$$U = \begin{pmatrix} c_{12}c_{13} & s_{12}c_{13} & s_{13}e^{-i\delta_{CP}} \\ -s_{12}c_{23} - c_{12}s_{23}s_{13}e^{i\delta_{CP}} & c_{12}c_{23} - s_{12}s_{23}s_{13}e^{i\delta_{CP}} & s_{23}c_{13} \\ s_{12}s_{23} - c_{12}c_{23}s_{13}e^{i\delta_{CP}} & -c_{12}s_{23} - s_{12}c_{23}s_{13}e^{i\delta_{CP}} & c_{23}c_{13} \end{pmatrix} \cdot \begin{pmatrix} 1 & 0 & 0 \\ 0 & e^{i\frac{\alpha_{21}}{2}} & 0 \\ 0 & 0 & e^{i\frac{\alpha_{31}}{2}} \end{pmatrix} \tag{1.6}$$

Here c_{ij} signifies $cos\theta_{ij}$ for $i,j \in \{1,2,3\}$ and $s_{ij} = sin\theta_{ij}$ for $i,j \in \{1,2,3\}$. U is called the PMNS matrix and can be described with three mixing angles θ_{12}, θ_{13} and θ_{23} and additional CP-violating phases δ_{CP}, α_{21} and α_{31} [Oli14]. If the neutrinos are dirac particles only δ_{CP} is used in order to describe CP-violating processes. It is possible that neutrinos are their own anti-particles. Particles with this property are called Majorana particles after Ettore Majorana [Maj37]. If neutrinos are Majorana particles all three CP-violating phases are needed.

The most simple case of neutrino oscillations describes the mixture of two neutrinos without CP-violation. Then 1.5 and 1.6 become simple:

$$\begin{pmatrix} \nu_\alpha \\ \nu_\beta \end{pmatrix} = \tilde{\mathrm{U}} \cdot \begin{pmatrix} \nu_1 \\ \nu_2 \end{pmatrix} \tag{1.7}$$

$$\tilde{\mathrm{U}} = \begin{pmatrix} cos\theta & sin\theta \\ -sin\theta & cos\theta \end{pmatrix} \tag{1.8}$$

where $\tilde{\mathrm{U}}$ is the modified mixing matrix and $\alpha, \beta \in \{e, \mu, \tau\}$. This simplification makes it easy to calculate the transition probability between two states ([Zub11])

$$P(\nu_\alpha \to \nu_\beta) = 1 - P(\nu_\alpha \to \nu_\alpha) = \sin^2(2\theta) \cdot \sin^2\left(\frac{\Delta m^2}{4}\frac{L}{E}\right) \tag{1.9}$$

with the transition probability P, $\Delta m^2 = m_2^2 - m_1^2$, the energy of the particle E, and the oscillation length L. Within this model neutrino oscillations can only occur if $\theta \neq 0$ and at least $m_1 \neq 0$ or $m_2 \neq 0$. This means that the existence of neutrino oscillations within this model requires massive neutrinos.

1.3.2 Neutrino oscillations in experiments

The Homestake experiment

The observation of the oscillations however was not simple and included the idea of utilizing the sun as a source of ν_e and reliable calculations of the expected solar neutrino production [Bah63] [BD76].

The first indication of neutrino oscillations was observed at the Homestake experiment [Dav79] [Cle98]. The detection principle is based on the inverse β-decay induced by neutrinos originating from the sun. The experiment utilized the chlorine from $615\,\mathrm{t}$ of tetrachlorethylene (C_2Cl_4) for this process.

$$\nu_e + n \to e^- + p \qquad (E_{\nu_e} \geq 0.814\,\mathrm{MeV}) \tag{1.10}$$

$$\nu_e + {}^{37}\mathrm{Cl} \to e^- + {}^{37}\mathrm{Ar} \tag{1.11}$$

When the number of ^{37}Ar reaches equilibrium it is purified and put into a proportional counter. There the electron capture of ^{37}Ar is detected.

$$e^- + {}^{37}\mathrm{Ar} \to {}^{37}\mathrm{Cl}^* + \nu_e \qquad \left(T_{\frac{1}{2}} = 35.011\,\mathrm{d}\right) \tag{1.12}$$

$${}^{37}\mathrm{Cl}^* \to {}^{37}\mathrm{Cl} + e^- \tag{1.13}$$

However other processes such as muons from cosmic rays can produce ^{37}Ar, too. A low background in order to observe the signal is needed. Both passive shielding and criteria for the signal function to be accepted were used to suppress this contribution [DHH68] [Cle98]. The measurements compared to the theories yielded [Bah95] [Cle98].

$$R = (2.56 \pm 0.32) \cdot 10^{-36}\,\frac{1}{\mathrm{s\,target\ atoms}} \qquad (\text{Homestake Experiment}) \tag{1.14}$$

$$R = (9.3 \pm 1.3) \cdot 10^{-36}\,\frac{1}{\mathrm{s\,target\ atoms}} \qquad (\text{Prediction}) \tag{1.15}$$

The results showed a significant deficit of the ν_e flux of about 70%. This difference can either be explained by mistakes in the experimental setup and the model of the sun or by neutrino oscillations.

Super-Kamiokande

Super-Kamiokande is an underground Čerenkov detector with a fiducial volume of $22.5\,\mathrm{kt}$ of purified water surrounded by about 11000 photomultiplier tubes (PMTs) [Fuk98a]. On the one hand Super-Kamiokande was able to confirm the solar neutrino deficit already observed by the Homestake experiment [Fuk98b]. On the other hand Super-Kamiokande was able to detect atmospheric neutrinos via charged current interactions [Fuk98a].

$$\nu_e + N \to e^- + X \qquad \bar{\nu}_e + N \to e^+ + X \tag{1.16}$$

$$\nu_\mu + N \to \mu^- + X \qquad \bar{\nu}_\mu + N \to \mu^+ + X \tag{1.17}$$

Here N denotes a nucleus and X represents hadronic components resulting from the interaction. Atmospheric neutrinos are neutrinos which are produced in the atmosphere during the decay of pions which are produced by an interaction between hadrons of cosmic rays and nuclei of the atmosphere [Fuk98a].

$$\pi^+ \to \mu^+ + \nu_\mu \to e^+ + \bar{\nu}_\mu + \nu_e + \nu_\mu \tag{1.18}$$

Neutrinos traversing the detector downwards have only passed the atmosphere ($15\,\mathrm{km}$) while neutrinos moving upward have traversed the earth ($13\,000\,\mathrm{km}$). For neutrino oscillations on the length of the diameter of the earth a upward-downward asymmetry of the neutrino-induced events is expected. The Super-Kamiokande detector was indeed able to detect such an asymmetry [Fuk98a]. The results can be seen on the bottom left hand side of figure 1.1. The up-down-asymmetry is only significant for higher momenta of the myons because the correlation between the direction of the neutrino and the produced myon gets better for increasing momentum. No corresponding surplus can be seen for electron-like events (top of figure 1.1) which means that $\nu_\mu \to \nu_e$ oscillations are not responsible for this reduction. This was interpreted as ν_μ oscillations into either ν_τ or sterile neutrinos [Fuk98a].

Neutrino oscillation parameters

Many experiments have measured neutrino oscillation parameters since then. The resulting parameters are compiled in table 1.1.

Table 1.1: **Oscillation parameters.** The oscillation parameters for normal hierarchy are summarised. The results are taken from [Cap14].

Parameter	Best fit and 1σ interval
Δm^2_{21}	$\left(7.54^{+0.26}_{-0.22}\right) \cdot 10^{-5}\,\mathrm{eV}^2$
Δm^2_{32}	$\left(2.43^{+0.06}_{-0.06}\right) \cdot 10^{-3}\,\mathrm{eV}^2$
$sin^2\theta_{12}$	$0.308^{+0.017}_{-0.017}$
$sin^2\theta_{13}$	$0.0234^{+0.0020}_{-0.0019}$
$sin^2\theta_{23}$	$0.437^{+0.023}_{-0.033}$

Neutrino mass scale

In spite of the advances in neutrino physics several issues remain and are not answered yet. Two problems are the order of the neutrino masses and the absolute mass scale. This cannot be determined by oscillation experiments because the square of the mass differences of two neutrinos determines the oscillations. The sign of the mass difference on the other hand does not impact the

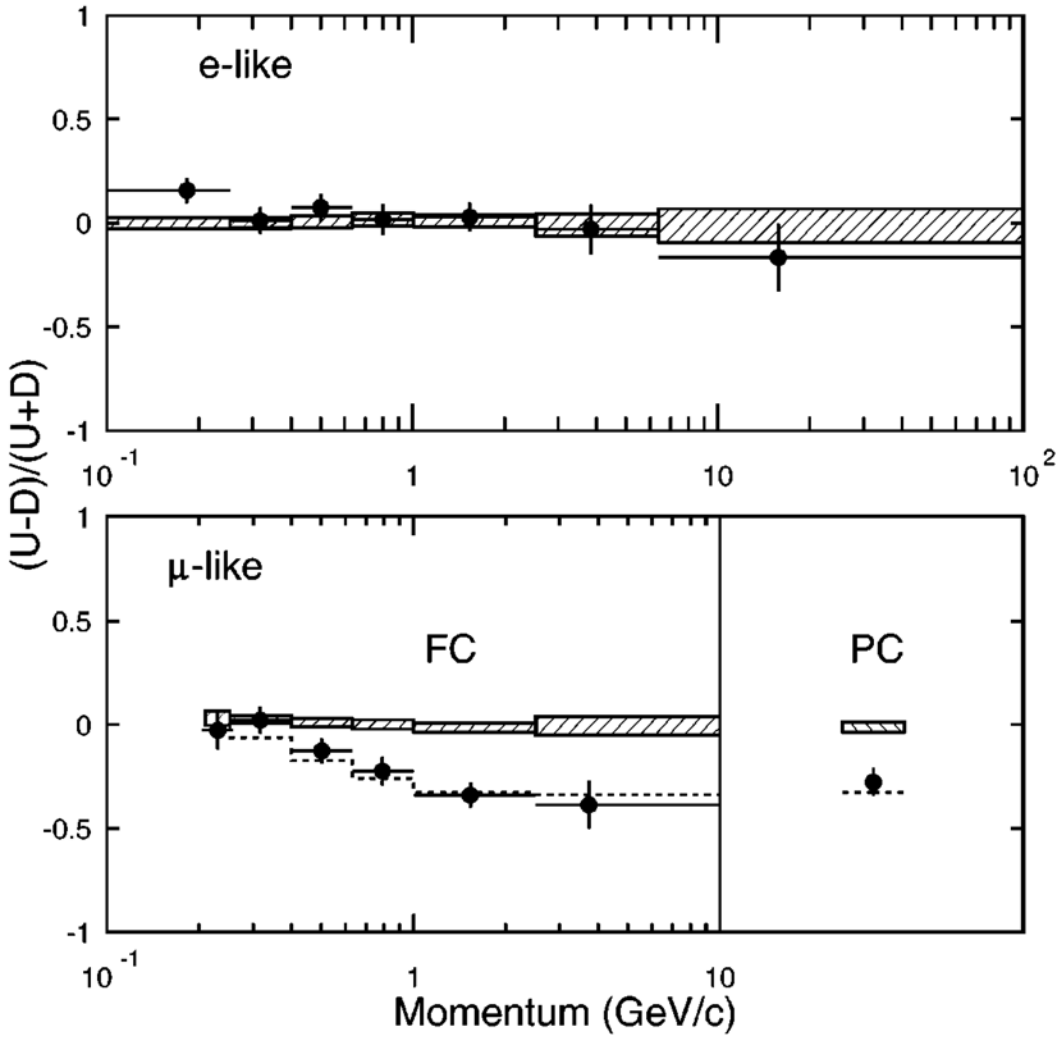

Figure 1.1: **Data for neutrino oscillations at Super-Kamiokande** The dots with error bars are measurement points, the hatched regions are the expectation without neutrino oscillations and the dashed line is the expectation for neutrino oscillations with $\Delta m^2 = 2.2 \cdot 10^{-3}\,\mathrm{eV}^2$ and $\theta = 45°$. The asymmetry $\frac{U-D}{U+D}$ is plotted against the momentum of the particle. U is the number of upwards going particles while D is the number of downwards going particles. At the **top** electron-like events are plotted. In the **bottom left** fully contained myon-like events are plotted while in the **bottom right** partially contained events are plotted. Picture taken from [Fuk98a].

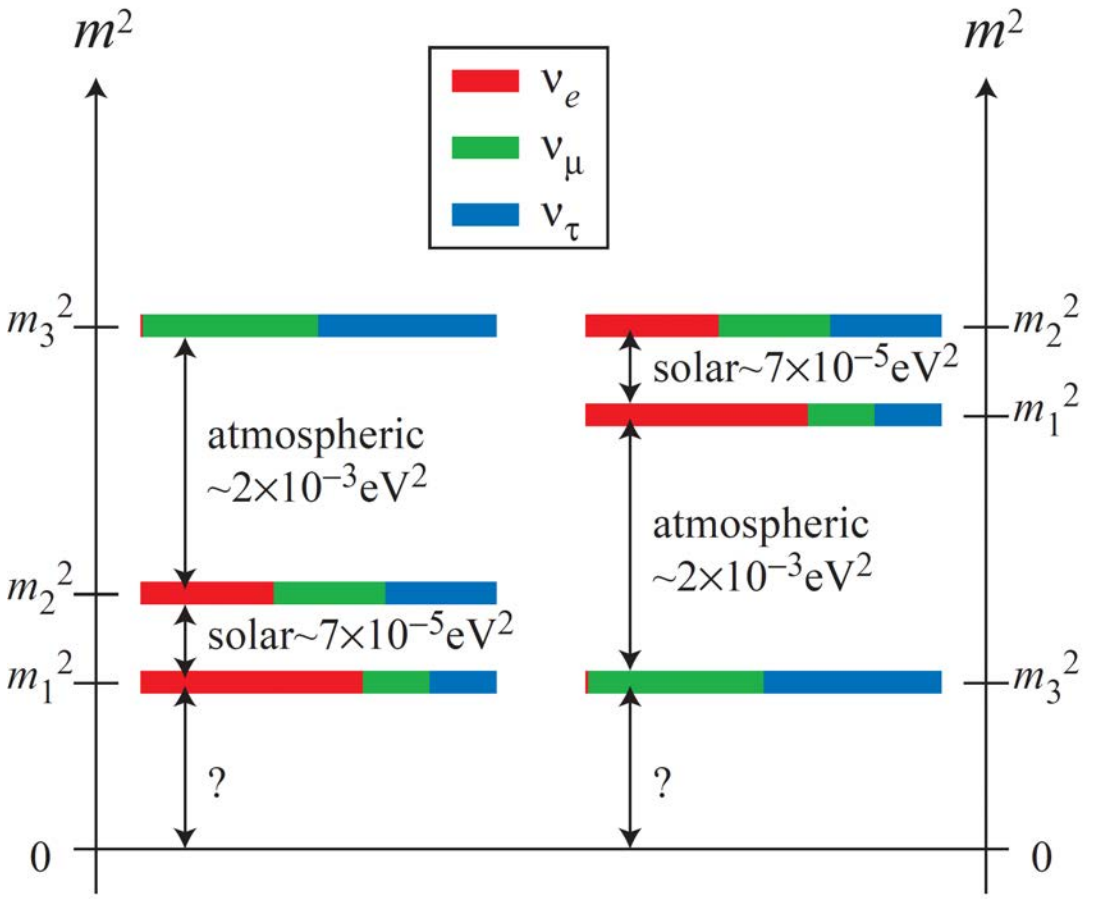

Figure 1.2: **Hierarchical model of neutrino masses** On the **left hand side** the normal mass hierarchy can be seen. On the **right hand side** the inverted mass hierarchy can be seen. The absolute scale of lowest mass is not known yet. Picture taken from [KL13].

oscillations and thus cannot be measured via oscillations. Three different scenarios are possible: the normal hierarchy, the inverted hierarchy and the quasi-degenerate mass hierarchy. Quasi-degenerate order implies that the neutrino masses are similar: $m_{\nu_1} \approx m_{\nu_2} \approx m_{\nu_3}$ while hierarchical order implies that the masses differ significantly. The normal hierarchy is the scenario in which $m_1 < m_2 \ll m_3$ holds. The inverse of this order is $m_3 \ll m_1 < m_2$ and is called the inverse mass hierarchy. The normal and inverted scenarios are depicted in figure 1.2.

1.3.3 Implications for the SM

Neutrino masses can in principle be added to the SM by treating neutrinos like the other fermions. However, this requires a chiral right handed neutrino singlet. Additionally, because of the tiny neutrino mass the Yukawa coupling of the neutrinos to the Higgs field would have to be much smaller than the other couplings [Zub11].

An alternative are neutrinos with Majorana character. However the resulting term cannot be normalized and does not conserve $B - L$ with the baryon number B and the lepton number L [Kli13]. Additionally neutrino masses can be explained by new physics such as extra dimensions [Ark01] or SUSY [Cas00].

Within the SM it remains difficult to explain why the mass of the neutrinos is so small. This is possibly related to "a new fundamental mass scale and thus to new physics beyond the Standard Model" [Oli14]. Therefore, neutrino physics is a promising candidate to gain insight into physics beyond the SM.

1.4 Determination of the neutrino mass

In addition to giving insight into the generation of mass and probing the available models, the neutrino mass is of interest to cosmology. One example is the structure formation because its mass influences the creation of large scale structures [AF11]. The absolute neutrino masses cannot be measured with neutrino oscillations which makes other measurement techniques necessary. One possibility is to use indirect constraints on the neutrino mass by cosmological observations in combination with model assumptions (section 1.4.1). A way which is less dependant on model assumptions is the utilisation of β-decays (section 1.4.2, 1.4.3 and 1.4.4).

1.4.1 Cosmological approach

There are several observations in cosmology which can be utilized to give borders on the neutrino mass. Neutrinos from supernovae, the CMB spectrum, polarization measurements, baryonic acoustic oscillations and lensing studies can be used for this.

Supernova SN 1987A

About 25 neutrinos from the supernova SN 1987A were detected by the Kamiokande II [Hir87] [Hir88], Irvine-Michigan-Brookhaven (IMB) [Bio87] [Bra88] and also by the Baksan detectors [Ale87] [Ale88]. Using the time differences between those events and the energy of the events the neutrino mass can be obtained [Zub11]. Using models for the neutrino production in supernovae and the detection efficiency of the detectors a model dependant upper limit on the neutrino mass could be found [LL02]:

$$m_{\bar{\nu}_e} < 5.7\,\mathrm{eV} \qquad (95\%\mathrm{C.L.}) \tag{1.19}$$

This upper limit can be improved by looking at data concerning the structure formation of our universe.

Structure formation of the universe

Neutrinos with a mass of about $0.1\,\mathrm{eV}$ can affect the development of large scale structures [Elg02]. Inversely, this enables the constraint of the neutrino mass by observing the scale of the structures in our universe.

The theory of the evolution of the universe includes that our universe is expanding and as a consequence is cooling down during its evolution. Right after the beginning of our universe the temperature and density was high enough for neutrinos to interact so frequently, that they were in equilibrium with other particles [Lid13]. These interactions included

$$\nu + \bar{\nu} \leftrightarrow e^+ + e^- \leftrightarrow \gamma + \gamma \tag{1.20}$$

$$p + e^- \leftrightarrow n + \nu_e \tag{1.21}$$

The process in (1.20) is possible as long as each step has a total energy greater than $2{\cdot}m_e \approx 1\,\mathrm{MeV}$. When the energy drops below this threshold ($k_B \cdot T < m_e \cdot c^2$) the conversion into $e^- + e^+$ is forbidden by energy conservation. Additionally, the rate of weak interaction becomes smaller than the expansion rate at $1\,\mathrm{MeV}$. This is called the freeze-out of the weak interaction. The neutrinos are no longer in equilibrium with matter which means that the universe becomes transparent to neutrinos. The neutrinos can stream freely from structures which are smaller than their free-streaming length [Zub11].

$$\lambda_{FS} \approx 1230 \cdot \left(\frac{\mathrm{eV}}{m_\nu}\right) \mathrm{Mpc} \tag{1.22}$$

Neutrinos in more dense areas of the universe can move to areas with smaller density without interactions if the areas are smaller than the free-streaming length. This means that structures smaller than the free-streaming length can be damped or removed entirely [Zub11].

To find a limit on the sum of the neutrino masses $\sum m_\nu$ the Planck Collaboration added $\sum m_\nu$ to the standard model of cosmology [1]. They combined the cosmic microwave background (CMB) measurements by the Planck satellite [Ade14a], polarisation measurements from WMAP [Ben13], measurements of baryonic acoustic oscillations [Bla12] [Beu11] [Pad12] [And12], CMB lensing data from Planck [Ade14b] and the South Pole Telescope (SPT) [Eng12], galaxy lensing measurements from the Canada-France-Hawaii Telescope Lensing Survey (CFHTLenS) [Kil13] and galaxy cluster counts [Ade14c]. This analysis constrains the sum of the neutrino masses to [Ade14b]

$$\sum m_\nu < (0.32 \pm 0.08)\,\mathrm{eV} \tag{1.23}$$

However, this result is dependant on the data used and depends on the validity of the cosmological standard model. Additionally, Battye et al. point out that there is tension between CMB measurements and lensing and cluster measurements [BM14]. Also, the neutrino mass limits derived from the shape of the power spectrum are smaller than the value obtained here [RPD14] [Sha]. However, the biggest problem is the model dependency of this approach. Measurements which provide results with less model dependencies utilise the kinematics of the β-decays.

1.4.2 Neutrinoless double β-decay

The double β-decay ($2\nu\beta\beta$-decay) is a process of higher order. It describes two simultaneous β-decays (see figure 1.3 a) [GM35]. The $2\nu\beta\beta$-decay is dominant when the β-decay is suppressed. This is observed in even isobaric mass chains where the nuclei are either odd-odd or even-even. The binding energy of the even-even atoms can be higher than both of the neighbouring odd-odd nuclei so that no β-decay is not possible. However, the $2\nu\beta\beta$-decay is possible. The binding energy is described well by the Bethe-Weizsaecker model [Wei35]. The pairing energy in this formula predicts that even-even nuclei lie on a parabola of lower energy than odd-odd nuclei (left hand side of figure 1.4). Therefore, experiments use even-even-nuclei with energetically forbidden β-decays.

There may exist another decay which is even rarer than the $2\nu\beta\beta$-decay. Majorana was the first to describe the possibility of a particle being its own anti-particle [Maj37]. It is possible to apply this theory to neutrinos. This results in the Majorana neutrinos $\nu_M \equiv \bar{\nu}_M$. This enables the neutrino-less double β-decay ($0\nu\beta\beta$-decay) [Fur39]. This decay is made possible by the exchange of a virtual Majorana neutrino (see the right hand side of figure 1.3). The probability for this decay would be even smaller and can be seen as a small peak near the endpoint of the $2\nu\beta\beta$-decay spectrum (see the right hand side of figure 1.4). The Majorana mass is calculated from the measured half-life with (1.24) [Oli14]. The Majorana mass however is a mixture of three superposed mass states with majorana phases contained within the matrix elements U_{ei}. These phases can lead to (partial) cancellations of the addends [Oli14].

$$\left(T^{0\nu}_{\frac{1}{2}}\right)^{-1} = G^{0\nu} \cdot \left|M^{0\nu}\right|^2 \cdot < m_{\beta\beta} >^2 \tag{1.24}$$

$$< m_{\beta\beta} >^2 = \left|\sum_i U_{\mathrm{ei}} m_{\nu_i}\right|^2 \tag{1.25}$$

where $T^{0\nu}_{\frac{1}{2}}$ is the half-life of the isotope, $G^{0\nu}$ is the face space factor, $M^{0\nu}$ is the matrix element and $< m_{\beta\beta} >$ is the effective majorana mass.

[1] sometimes referred to as $\Lambda\mathrm{CDM} - \mathrm{model}$

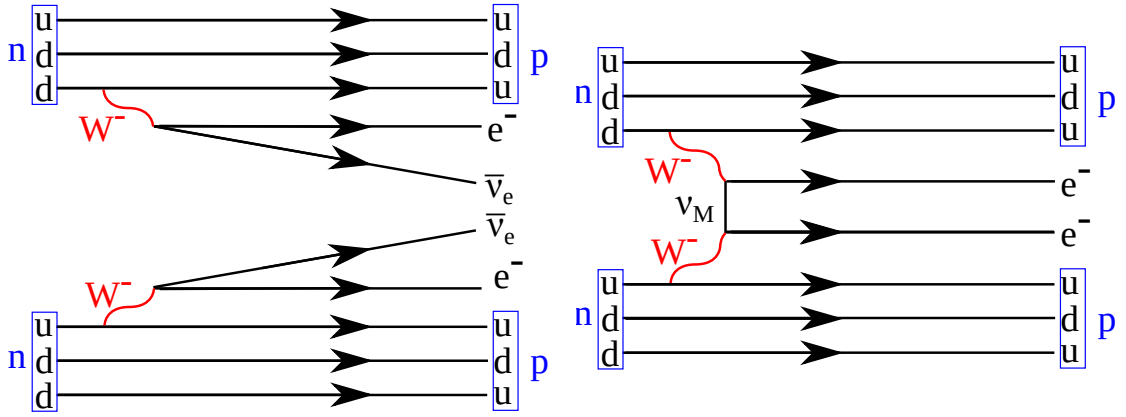

Figure 1.3: **Double β-decay. Left hand side:** $2\nu\beta\beta$-decay: Two neutrons decay simultaneously into a proton, an electron and an electron anti-neutrino. **Right hand side:** $0\nu\beta\beta$-decay: Two neutrons convert into two protons and two electrons (e^-) and exchange a Majorana neutrino.

$0\nu\beta\beta$-experiments with ^{76}Ge and ^{136}Xe have been performed. Both Kamland-Zen and EXO-200 did not observe the $0\nu\beta\beta$-decay of ^{136}Xe and give a lower limit of $T^{0\nu}_{1/2} >= 3.4 \cdot 10^{25}$ y (90% C.L.) corresponding to $< m_{\beta\beta} >< 0.150\,\text{eV} - 0.250\,\text{eV}$ [Gan13]. Recent results of GERDA, which searches for the $0\nu\beta\beta$-decay of ^{76}Ge, reveal that the half-life is $T^{0\nu}_{1/2} > 2.1 \cdot 10^{25}$ y (90% C.L.). The upper limit of the $0\nu\beta\beta$ neutrino mass is between $m_{\beta\beta} = 0.2\,\text{eV}$ and $0.4\,\text{eV}$ [Ago13]. The GERDA results show a discrepancy with the claim of the discovery of the $0\nu\beta\beta$-decay of ^{76}Ge made by a part of the Heidelberg-Moskow-collaboration which stated that the $0\nu\beta\beta$ neutrino mass is $< m_{\beta\beta} >= (0.32 \pm 0.03)\,\text{eV}$ [Kla01].

1.4.3 Electron capture

The electron capture can also be used to determine the ν_e energy.

$$e^- + ^{163}\text{Ho} \rightarrow ^{163}\text{Dy}^* + \nu_e \rightarrow ^{163}\text{Dy} + E_C + \nu_e \tag{1.26}$$

One experiment which pursues this is the electron capture on ^{163}Ho (ECHo) experiment. It uses metallic magnetic calorimeters at low temperatures. A first prototype used a gold adsorber with implanted ^{163}Ho which showed promising results [Gas14].

1.4.4 β-decay

A promising way to determine the $\bar{\nu}_e$-mass is the study of the β-decay (see (1.1)). The energy of the decay gets distributed among the electron, the electron antineutrino and the nucleus. The nucleus is heavy when compared to the electron and the neutrino. Due to energy and momentum conservation the energy distributed to the nucleus will remain nearly unchanged and is subtracted from the available energy for the neutrino and the electron [Dre13]. The energy of the electron antineutrino is

$$E_{\bar{\nu}_e} = \sqrt{m^2_{\bar{\nu}_e} \cdot c^4 + p^2_{\bar{\nu}_e} c^2} \geq m_{\bar{\nu}_e} \cdot c^2 \tag{1.27}$$

Consequently, the neutrino has at least its mass as energy. This missing energy can be observed in the electron spectrum (see figure 1.5). For high neutrino energies the missing energy is dominated by the momentum of the neutrino while for $p^2_{\bar{\nu}_e} c^2 \approx 0$ only the energy corresponding to the neutrino mass is missing. This means that measurements near the end-point of a β-spectrum

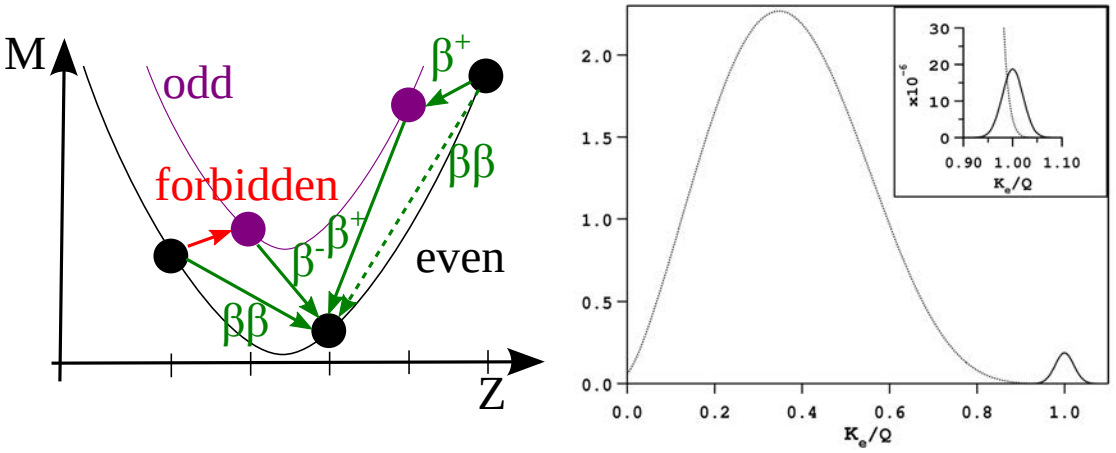

Figure 1.4: **Double β-decay. Left hand side** Sketch of mass parabolas for $A = const.$ The possible decays are indicated. In principle all instable nuclei can decay via 2β-decays, but observation is only possible for nuclei where the conventional (preferred) β-decay is forbidden (indicated in red). **Right hand side** Energy spectrum of the two emitted electrons of both $0\nu\beta\beta$ (dashed line) and $2\nu\beta\beta$ (solid line). Figure adapted from [EV02].

contain high quality information on $m_{\bar{\nu}_e}$ [Bor05]. This mass is a superposition of the three mass eigenstates.

$$m^2_{\bar{\nu}_e} = \sum_{i=1}^{3} \left|U^2_{ei}\right| \cdot m^2_{\nu_i} \tag{1.28}$$

In order to obtain the energy spectrum the decay rate can be calculated with Fermi's golden rule [Dre13] [Fer34]

$$\Gamma = \frac{2 \cdot \pi}{\hbar} \cdot \int_{all final states} |M|^2 \, \mathrm{d}f \tag{1.29}$$

Here Γ is the decay rate and M is the transition matrix element from an initial state to a final state f. Based on this the electron spectrum of a β-decay can be calculated[2]:

$$\begin{aligned} \frac{\mathrm{d}N}{\mathrm{d}E} =& \frac{G_F^2 \cdot \cos\theta_C}{2 \cdot \pi^3} \cdot |M_{\mathrm{nucl}^2}| \cdot F(E, Z') \cdot (E + m_e) \cdot \sqrt{(E + m_e)^2 - m_e^2} \\ & \cdot \sum_{i,j} \left|U^2_{ei}\right| \cdot P_j \cdot (\epsilon - V_j) \cdot \sqrt{(\epsilon - V_j)^2 - m^2_{\nu_i}} \cdot \theta\left(\epsilon - V_j - m_{\nu_i}\right) \end{aligned} \tag{1.30}$$

where G_F is the Fermi coupling constant, θ_C is the Cabbibo angle, M_{nucl} is the matrix element for the nuclear components, $F(E, Z-1)$ is the Fermi function which describes the interaction of the emitted electron with the daughter nucleus of the decay, E the kinetic energy of the electron, U_{ei} the matrix elements of the PMNS matrix (see (1.6)), where P_j and V_j are the excitation probabilities and energies of the final state[3], the endpoint energy E_0, the kinetic energy of the electron E, $\epsilon = E_0 - E$, $E_0 = Q - E_{rec}$, Q the nuclear Q-value, E_{rec} the recoil energy of the nucleus, $\hbar = 1$ and $c = 1$.

[2] For a more detailed explanation see [Dre13]

[3] Accounting for atomic excitations e.g. vibration and rotation.

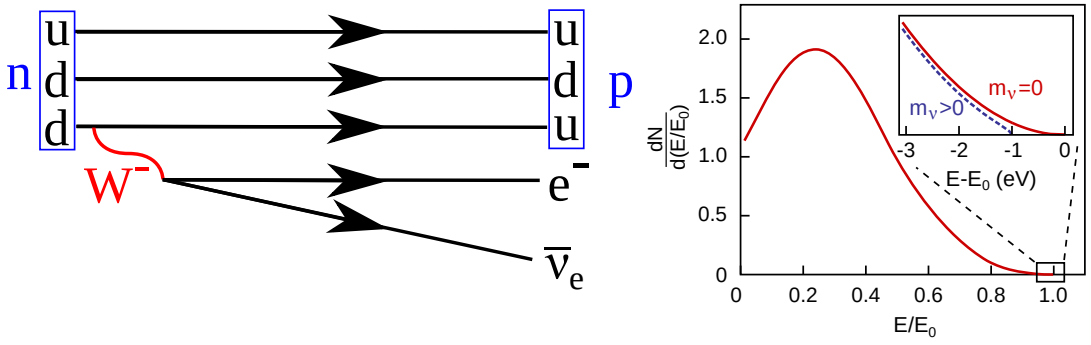

Figure 1.5: **The β-decay. Left hand side:** The Feynman diagram of the β-decay is shown. A neutron decays into a proton and emits an elecron and an electron antineutrino. **Right hand side:** The end-point of the energy spectrum of the β-decay is shown. Picture taken from [Sch09].

Rhenium source

The ^{187}Re-decay was used by the Milano experiment. The advantage of ^{187}Re is its low Q value $Q = 2.469 \pm 0.004\,\mathrm{keV}$. Its downside is a long life-time $T_{1/2} = 4.33 \cdot 10^7\,\mathrm{y}$ [Bas09]. As a detector thermal $AgReO_4$ micro-calorimeters were used. The inclusion of the source in the detector allows for full energy containment and final states as mentioned above do not need to be considered. The experimental constraint on the electron antineutrino mass is [Sis04]:

$$m_{\bar{\nu}_e} < 15\,\mathrm{eV} \qquad (90\%\mathrm{C.L.}) \tag{1.31}$$

Tritium source

The β-decay of tritium is also used to determine the electron antineutrino mass.

$$^3\mathrm{H} \rightarrow ^3\mathrm{He}^+ + e^- + \bar{\nu}_e \tag{1.32}$$

In order to measure the electron spectrum of the tritium in KATRIN, magnetic adiabatic collimation combined with an electrostatic (MAC-E) filters are used. The best constraints on the electron antineutrino mass until now are given by the Troitsk experiment $m_{\bar{\nu}_e} < 2.05\,\mathrm{eV}(95\%\mathrm{C.L.})$ and the Mainz experiment $m_{\bar{\nu}_e} < 2.3\,\mathrm{eV}(95\%\mathrm{C.L.})$ [Kra05] [Ase11]. The next generation of tritium experiment is the Karlsruhe Tritium Neutrino (KATRIN) experiment (see chapter 2).

2. The KATRIN experiment

The **KA**rlsruhe **TRI**tium **N**eutrino (KATRIN) [KAT05] experiment has the primary goal to determine the electron antineutrino mass $m_{\bar{\nu}_e}$ with a sensitivity of $200\,\mathrm{meV/c^2}$ ($90\,\%$ C.L.) by measuring the β-spectrum of tritium (see section 2.1). The measurement principle is based on magnetic adiabatic collimation combined with an electrostatic (MAC-E) filter (see section 2.2). The setup of the KATRIN experiment can be divided into four sections: the windowless gaseous tritium source, the transport section, the spectrometer section and the detector (see section 2.3). Section 2.4 discusses the KATRIN sensitivity as well as major background sources.

2.1 β-decay of tritium

The β-decay of tritium (^3H) is a most promising decay for the determination of the neutrino mass.

Tritium has a very low end-point energy ($Q = (18\,590.1 \pm 1.7)\,\mathrm{eV}$) [Dyc93]. The end-point energy is of interest because the number of electrons in an energy window including the endpoint depends on $1/E_0^3$. The endpoint energy is of additional interest because it determines the maximal voltage of the electrostatic filter which is needed to scan the whole spectrum. Higher voltages make the setup technically more challenging.

In principle $^{187}\mathrm{Re}$ has a lower endpoint energy ($2.47\,\mathrm{keV}$ [Gal00]). However, tritium has major advantages compared to $^{187}\mathrm{Re}$. However tritium has some major advantages :

- The first major advantage of tritium is its short half-life $T_{1/2} = (12.32 \pm 0.02)\,\mathrm{y}$. A shorter half-life means that the same mass of material will produce more decays per second. This is important because of two competing processes. In general more mass means higher luminosity which translates into higher statistics. However, the mass is limited due to scattering efects which ruin the energy resolution by allowing for scattering processes. Therefore the luminosity is limited by the lifetime.
- It has a low atomic number and the resulting simplicity of the atomic structure. This enables the easy calculation of the nuclear matrix element.
- Tritium is a super-allowed decay which yields an energy-independent matrix element for tritium [Bel03].
- Another advantage of tritium is the low charge. This translates to a low scattering probability [Bor08]. The low charge also implies a simple spectrum which enables the calculation of the transition probabilities [Sae00]

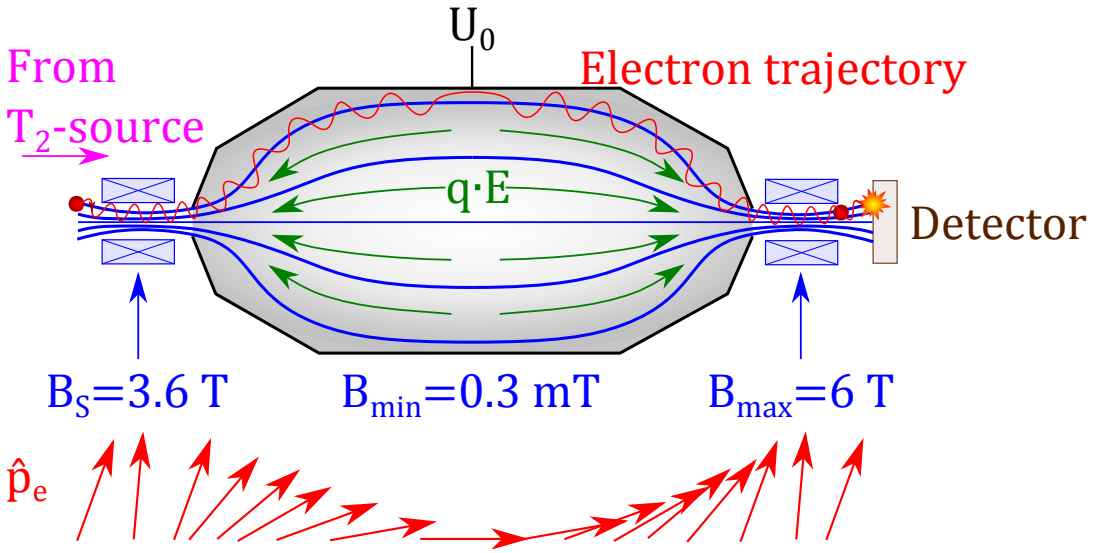

Figure 2.1: **Sketch of the electromagnetic fields in the KATRIN main spectrometer.** The KATRIN main spectrometer forms an electrode for the electric field (green). The magnets located next to the openings of the main spectrometer create strong magnetic fields (blue) in their centres. Electrons gyrate around the magnetic field lines (red). Because of the gradient of the magnetic field the orientation of the electron momentum is forced to be more parallel to the magnetic field at the centre of the spectrometer (red arrows at the bottom). The picture is inspired by [KAT05].

- The recoil correction for the decay product is nearly constant ($E_{\mathrm{rec}} = 1.72\,\mathrm{eV}$) [Mas07].
- Tritium is gaseous even at temperatures of 30 K. Therefore, no solid state corrections have to be considered reducing the systematic error [Bab12].

However, tritium forms molecules. Molecules have vibrational and rotational excitations which increases the number of final states resulting in an intrinsic uncertainty which cannot be circumvented by any experimental setup with a molecular gaseous tritium source.

The utilisation of a tritium source in combination with a MAC-E filter has had great success in the past and lead to the most stringent direct neutrino mass limits [Kra05] [Ase11].

2.2 Functionality of a MAC-E filter

The utilisation of a MAC-E[1] filter allows to analyse the a large flux of electrons with a high acceptance angle. The filter essentially works as an integrating high-pass filter for electrons with a tunable threshold energy.

Magnetic adiabatic collimation

The electrostatic filter is only sensitive to the longitudinal energy component. To achieve good resolutions it is necessary to align the momenta of the electrons in such a way that they are perpendicular to the analysing plane. In addition this change of direction must happen adiabatically which means that the electromagnetic fields do not change fast during one gyration of an electron and that the magnetic moment is conserved. One well-known way to redirect particles adiabatically is the utilisation of magnetic fields (see figure 2.1).

This is realised by two strong solenoids at both the entrance and the exit of the spectrometer. The resulting field lines are perpendicular to the analysing plane. The electron energies can now be

[1] **M**agnetic **A**diabatic **C**ollimation **C**ombined with an **E**lectrostatic

divided into a component perpendicular to the magnetic field $E_\perp$ and a component parallel to the magnetic field $E_\parallel$.

$$E = E_\perp + E_\parallel \tag{2.1}$$

The goal is to minimise $E_\perp$ thereby minimising the energy component which is lost in the electrostatic filter. This minimisation is achieved by a huge decline ($\approx 2 \cdot 10^{-5}$) of magnetic field strength from the entrances of the spectrometer vessel to the analysing plane. The decrease of the magnetic field at the centre of the spectrometer translates to an orientation of the electron momenta because of the conservation of the orbital magnetic moment μ of the electrons:

$$\gamma \cdot \mu = \frac{\gamma + 1}{2} \cdot \frac{E_\perp}{B} = \text{const.} \tag{2.2}$$

Here γ is the relativistic Lorentz factor. For non-relativistic [2] adiabatic motions the magnetic moment of the electron is conserved and (2.2) is reduced to

$$\mu = \frac{E_\perp}{B} = constant \tag{2.3}$$

From this simplified equation it can be seen that the drop of the magnetic field strength by $2 \cdot 10^{-5}$ forces an identical reduction of $E_\perp$. This results in an energy resolution of

$$\Delta E = 2 \cdot 10^{-5} \cdot E_0 = 0.93\,\text{eV}. \tag{2.4}$$

In conclusion, a small fraction of the energy can not be analysed. The fraction is defined by the magnetic field ratio.

Electrostatic filter

The electrostatic filter transmits electrons in dependence of their kinetic energy. This is realized by applying a retarding potential U between the electrodes and the ground electrodes at the entrance and exit of the spectrometer. As a consequence the voltage has a maximal value close to the center of the setup where the longitudinal energy is minimal. This plane is called analysing plane. It can only be passed by electrons with a longitudinal kinetic energy component which is greater than the retarding potential $-e \cdot U_0$. The electrons passing the analysing plane are then re-accelerated to their initial energy before they and leave the electrostatic filter. Because of the threshold all electrons with energies greater than the retarding potential are transmitted. Hence, the integrated spectrum of electrons with energies ranging from the threshold to the endpoint of the tritium β-spectrum can be observed by counting the number of electrons which pass the electrostatic filter.

Accepting angle

Another way for electrons to be reflected back is the reflection by the magnetic fields. This effect is called magnetic mirror effect and is discussed in more detail in section 3.1. This effect is dependent on the polar angle θ with which the particles were emitted from the source. When this angle surpasses a threshold $\theta_{\max}$ the particle is reflected in the MAC-E filter. In the simplified case of no electric fields the threshold angle is:

$$\sin(\theta_{\max}) = \sqrt{\frac{B_\text{S}}{B_{\max}}} \tag{2.5}$$

$$\theta_{\max} \approx 50.8^\circ \tag{2.6}$$

where $B_\text{S} = 3.6\,\text{T}$ is the magnetic field at the source and $B_{\max} = 6\,\text{T}$ is the maximum of the magnetic field [Wan13]. The influence of the electrostatic field is considered in [Wan13]. As the path length in the source tube increases with the starting angle, which leads to more energy losses due to scattering, it is advantageous for the sensitivity to exclude high starting angles [Wan13].

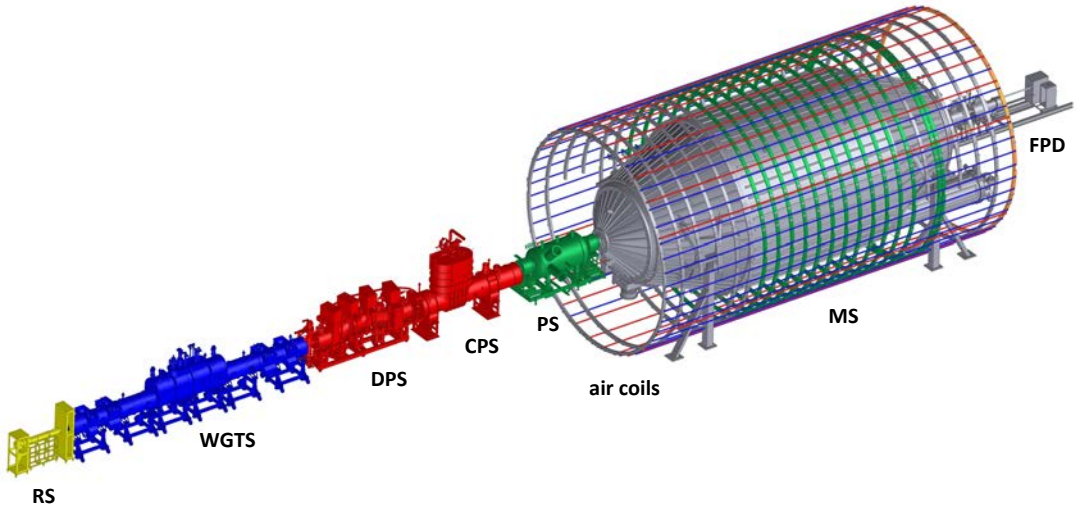

Figure 2.2: **Setup of the KATRIN experiment.** The setup of the KATRIN experiment can be divided into four subsections. The source section which consists of the rear section (RS) and the windowless gaseous tritium source (WGTS). The RS monitors the activity of the WGTs. The WGTS provides a stable column density of tritium molecules in the source. The resulting electrons are guided through the transport section consisting of the differential pumping section (DPS) and the cryogenic pumping section (CPS) by magnetic fields. The transport section transmits electrons but traps tritium. The electrons are transmitted to the pre-spectrometer (PS) and the main spectrometer (MS) which filter electrons with energies below a chosen energy threshold. The transmitted electrons originating from tritium β-decay are guided to the focal-plane detector (FPD) and detected. Picture taken from [Sch14].

2.3 Setup of the KATRIN experiment

The KATRIN experiment consists of a source section, a transport section a spectrometer section and a detector section (figure 2.2).

2.3.1 Source section

In the KATRIN experiment a windowless gaseous tritium source (WGTS) is used. It is designed as a source of electrons originating from the β-decay of tritium with a high luminosity and low systematic uncertainties [KAT05]. The main component of the WGTS is a $10\,\mathrm{m}$ long tube with a diameter of $d = 90\,\mathrm{mm}$ filled with tritium [Bor08]. The tritium is injected at the centre, then diffuses to the turbo molecular pumps at both of the sides, is pumped and eventually reprocessed in a closed inner loop. The setup does not include windows because they could introduce an energy loss of the electrons [Fis14].

The tritium density in the WGTS was chosen as an optimum between two competing requirements. The first requirement is the need for high statistics which translates to a high luminosity and thus a higher density. The second requirement is to minimise the scattering of β-decay electrons on T_2-molecules. As a result a density of $\rho \cdot d = 5 \cdot 10^{17}\,\frac{\text{molecules}}{\text{cm}^2}$ corresponding to an activity of $1.7 \cdot 10^{11}\,\frac{\text{Bq}}{\text{s}}$ is chosen. The tritium molecules need to be at low temperatures in order to avoid a significant contribution of Doppler broadening to the energy resolution [Bab12]. Hence, the WGTS is cooled to $30\,\mathrm{K}$ by a neon thermosiphon [Gro09]. Additionally, it is important to ensure the stability of the column density to a level of $0.1\,\%$ since the activity and therefore the systematic uncertainty depends on it. Therefore, all parameters influencing the column density such as the

[2] $\gamma \cdot m_e \cdot c^2 = E \leq Q + E_0 \leftrightarrow \gamma \approx 1.04$. For the argumentation above $\gamma \approx 1$ is used.

temperature, pressure,pumping speed and purity of the T_2 need to be controlled rigidly [Bab12]. The high purity reduces systematics because tritium and molecules resulting from the decay of tritium (e.g. DT) vary both in mass and thus recoil energy and in rotational and vibrational excitations after the tritium decay. In order to control this influence the gas composition is monitored with a Raman system [Fis14].

The electrons are guided to both ends of the WGTS by magnetic fields created by superconducting magnets. At the upstream-end of the source is the rear section. It continuously monitors the activity of the tritium source. At the downstream end of the WGTS is the transport section.

2.3.2 Transport section

The transport section connects the WGTS with the spectrometer section. The transport section reduces the tritium flow by a factor of 10^{12} while guaranteeing an adiabatic transport of electrons from the source to the spectrometer section. This allows to reach the required background level $1\,\mathrm{mcps}$ induced by tritium decays [KAT05].

The transport section can be divided in two components: the differential pumping section (DPS) and the cryogenic pumping section (CPS).

The DPS utilises five superconducting solenoids ($5.5\,\mathrm{T}$) which are tilted in such a way, that the beam tube is diverted by two mutually cancelling 20° tilts. This suppresses beaming effects [Luo06]. At each transition of those five solenoids is one TMP. These four TMPs pump the tritium gas. The DPS is designed to reduce the tritium flow by a factor of 10^5 [KAT05]. This has been tested by the tritium argon frost pump (TRAP) [Eic08] .

The CPS also introduces two mutually cancelling bends (15°) into the beam line [Jan15]. Its suppression of tritium gas flow is based on the cryo-sorption of tritium on argon frost at liquid helium temperatures which increases the adsorption probability of tritium. The CPS is designed to decrease the tritium gas flow by a factor of 10^7[KAT05]. The electrons are guided adiabatically through the transport section by the superconducting solenoids and are guided to the spectrometer section.

2.3.3 Spectrometer section

The spectrometer section has the goal to select the electrons with respect to their kinetic energy using the MAC-E filter technique (see section 2.2). The energy range close to the endpoint of the spectrum is of interest because here the neutrino mass has the most pronounced effect [KAT05]. The spectrometer section includes the pre-spectrometer and the main spectrometer in the beam line and the external monitor spectrometer which monitors the high voltage stability. The main spectrometer and the pre-spectrometer both include an inner-wire electrode to which the retarding potential ($-e \cdot U \approx E_0$) is applied. The surrounding vessel is operated at a slightly higher potential ($-e \cdot U \approx E_0 + 100\,\mathrm{eV}$). This allows to block low-energetic negatively charged particles originating from the vessel. The pre-spectrometer and the main spectrometer are operated at ultra high vacuum conditions ($10^{-11}\,\mathrm{mbar}$) to minimise the ionisation processes of residual gas. The vacuum setup consists of cascaded TMPs (*Leybold Turbovac MAG W 280*) and non-evaporable getter (NEG) strips of the type *SAES St707K* situated in the pump ports (right-hand side of figure 2.4).

Pre-spectrometer

The pre-spectrometer is located further downstream of the CPS. It is $3.38\,\mathrm{m}$ long and has an inner diameter of $1.68\,\mathrm{m}$. The pre-spectrometer can be used to reduce the electron flux as much as possible without loosing electrons near the endpoint. The high electron flux can be reduced by approximately seven orders of magnitude [Pra11]. This is important because the reduced electron

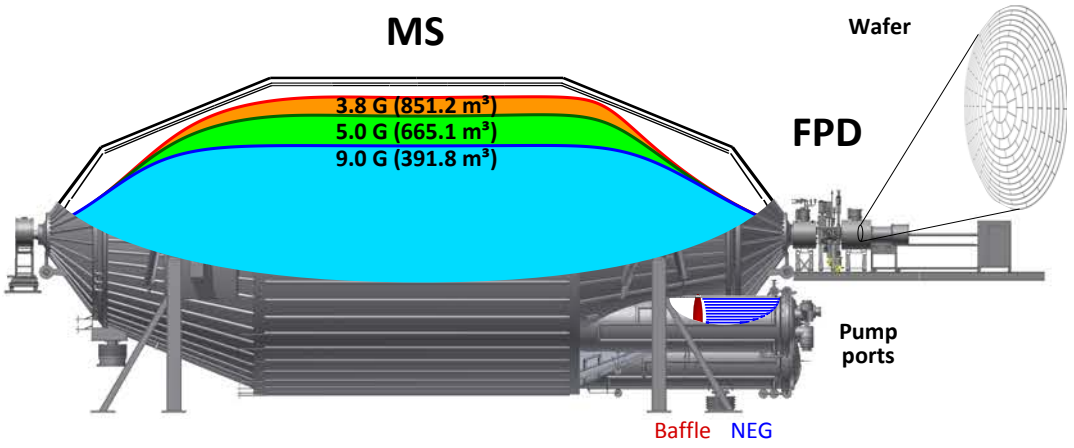

Figure 2.3: **Sketch of the KATRIN main spectrometer.** A schematic drawing of the KATRIN main spectrometer with the pump ports and the focal plane detector shows the sensitive volume for different magnetic settings denoted by the magnetic field B in the analysing plane (orange: 3.8 G, green: 5 G and light blue 9 G). Additionally, the position of the NEG strips (blue) and of the baffle (red) is shown exemplary. Modified version of a picture from [Sch14, p 43].

flux results in less ionisations of residual gas in the main spectrometer. The reduction is achieved by the utilisation of the MAC-E filter principle. The retarding potential is set to a value lower than the energy which is analysed, for example $e \cdot U = E_0 - 300\,\mathrm{eV}$. This way, only the electrons with high-quality information on the neutrino mass are transmitted. However this creates a Penning trap (see section 2.4.2).

Main spectrometer

The main spectrometer is downstream of the pre-spectrometer (see figure 2.3). The variation of the retarding potential allows to scan the region around the endpoint of the β-spectrum. The main spectrometer has a length of $23.3\,\mathrm{m}$ and a diameter of $10\,\mathrm{m}$. It is situated between two superconducting solenoids with a magnetic field strength of $4.5\,\mathrm{T}$ upstream and $B_{\mathrm{max}} = 6\,\mathrm{T}$ downstream respectively. The magnetic field strength of these solenoids decreases towards the analysing plane at the middle of the spectrometer and reaches a minimum of $B_{\mathrm{min}} = 0.3\,\mathrm{mT}$. The magnetic field is corrected with fourteen air coils coaxially arranged around the main spectrometer and two additional aircoils which compensate the earth magnetic field. They are used to correct earth's magnetic field and to shape the field at the analysing plane. With (2.3) an energy resolution of $\Delta E = 0.93\,\mathrm{eV}$ at $18.6\,\mathrm{keV}$ can be reached. This corresponds to an improvement of a factor of about 5 compared to previous experiments (Troitsk, Mainz).

Furthermore, the main spectrometer is equipped with inner wire electrodes to shield the sensitive volume from low energetic charged particles originating from the wall. The three NEG pumps situated in the three pump ports are a source of radon (see figure 2.4). Radon is a volatile gas which can desorb from the NEG material into the spectrometer volume and creates background. More details concerning the background production are given in section 2.4.2 and section 3.1.

Monitor spectrometer

The monitor spectrometer is not part of the KATRIN beamline. It is connected to the same voltage supply as the main spectrometer and monitors the high voltage stability of the main spectrometer by monitoring the conversion electrons from K-32 line ($E = 17.8\,\mathrm{keV}$) of a $^{83\mathrm{m}}\mathrm{Kr}$ source. In order to shift this line to the endpoint energy of the β-decay of tritium a potential of $U = -770\,\mathrm{V}$ is applied to the Krypton source resulting in electrons with an energy equal to the endpoint of the β-decay of tritium.

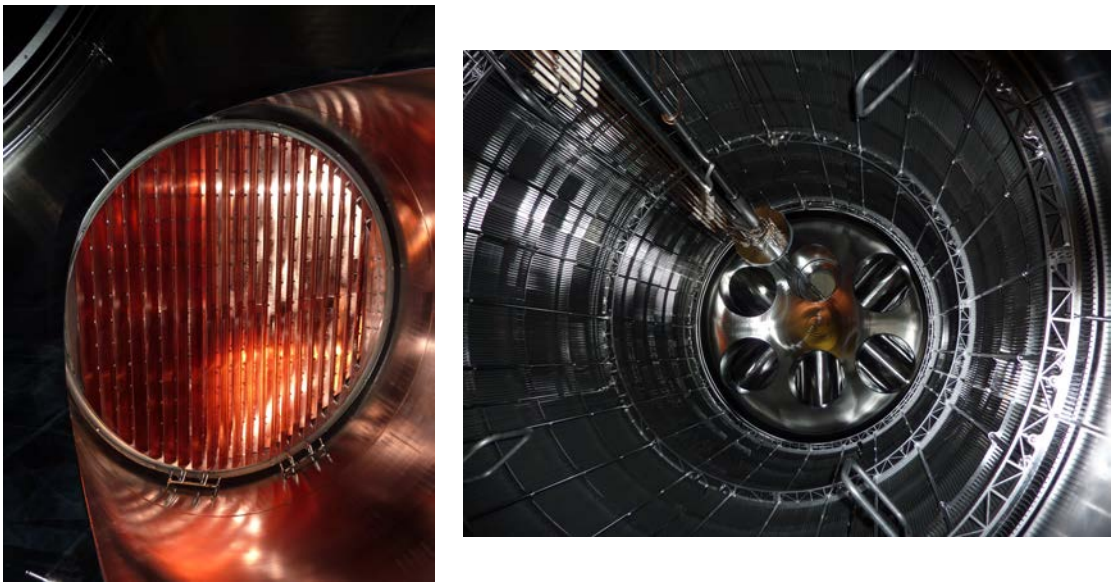

Figure 2.4: **Pictures of the baffle and the NEG strips.** On the left-hand side the pump port with a baffle consisting of V-shaped copper plates is shown. On the right-hand side the NEG strips of the getter are shown. The photographs are adapted from [Goe14].

2.3.4 Focal plane detector

The focal plane detector (FPD) is a silicon based positive-intrinsic-negative diode consisting of 148 pixels with equal area which are segments of coaxially arranged rings. Additionally, the FPD is shielded actively and passively. The FPD is downstream of the main spectrometer and counts the number of transmitted β-electrons. The energy resolution of the detector is approximately $1.5\,\mathrm{keV}$ [Sch14]. The passive shielding is realized by lead and copper blocks.The active shielding consists of plastic scintillators arranged to detect cosmic rays via coincidence measurements.

Between the main spectrometer and the focal plane detector is the post acceleration electrode (PAE). The PAE can be used to shift the energy of incoming electrons to a region with less background.

2.4 Sensitivity of the KATRIN experiment

In order to reach the design sensitivity of KATRIN $m_{\nu_e} = 200\,\mathrm{meV}$ at 90% C.L. both systematic and statistical errors have to be taken into account. The systematic uncertainties are expected to be $\sigma_{syst} \leq 0.017\,\mathrm{eV}^2$ [KAT05]. The statistical sensitivity was estimated to be $\sigma_{stat} \leq 0.018\,\mathrm{eV}^2$ [KAT05].

KATRIN needs a low background despite a tritium activity of $10^{11}\,\mathrm{Bq}$ provided by the WGTS. The reason is that only the fraction of electrons near the endpoint are of interest for the neutrino mass determination. In order to reach the design sensitivity of KATRIN $m_{\nu_e} = 200\,\mathrm{meV}$ at 90% C.L. the background must be a factor of two smaller than the signal [KAT05]. This corresponds to a background of only $10\,\mathrm{mcps}$. There are several possible background sources in MAC-E filters which can surpass the background limit.

2.4.1 Detector background

Cosmic muons, high energetic γ rays from radioactive decays in the vicinity of the detector and radioactive decays inside of the detector can contribute to the detector background. In order to prevent radioactive decays the detector material and the material surrounding it were examined and selected carefully[Sch14]. The cosmic muons are suppressed by coincidence measurements.

Additionally a multi-pixel cut can be applied to remove correlated events. For 146 pixels the remaining detector background during the first spectrometer and detector section (SDS-I) commissioning phase is $(10.34 \pm 0.44)\,\mathrm{mcps}$ in the complete region of interest [Leb10].

2.4.2 Background processes in the spectrometers of the KATRIN experiment

Penning traps

A Penning trap is a special configuration of electric and magnetic fields where the electric potential along a magnetic field line reaches a minimum. The potential well confines the electron motion with energies lower than the height of the potential well to one dimension. The magnetic field causes a cyclotron motion of the electron around the field line thus trapping it. This phenomenon has lead to huge backgrounds at the pre-spectrometer in the past which have been resolved [Fra14] [Fra10] [Mer12].

The operation of the pre-spectrometer and the main spectrometer with applied negative potentials separated by an area on ground potential forms a Penning trap. Adiabatically guided signal electrons cannot be trapped here since only electrons with energies lower than the potentials on either side can be trapped. These electrons can for example be signal electrons which have lost energy, secondary electrons from ionizations inside the trap or electrons produced in radioactive decays. These stored electrons can ionize residual gas and produce millions of positively charged ions which are not trapped. They can propagate in the main spectrometer and ionise residual gas molecules. The electrons liberated by these ionizations can contribute to the background. This Penning trap can have a significant influence on the background rate [Mer12]. One way to remove this Penning trap is to operate the pre-spectrometer at ground potential and accept the small increase of background due to the residual gas ionisation by the signal electrons in the main spectrometer. Another possibility might be the use of a wire scanner - a copper wire which wipes regularly through the trap and removes the stored electrons.

Background due to residual gas ionisation

Since the utilisation of two MAC-E filters next to each other creates a Penning trap the pre-spectrometer will be used at lower retarding potentials to avoid this. Therefore, a huge flux of β-decay electrons reaches the main spectrometer which makes ionisation processes in the spectrometers probable. The resulting positive ions are not affected by the analysing plane and can themselves ionise residual gas. The resulting electrons are accelerated due to the retarding potential, guided to the detector, and contribute to the background. This background can be reduced by using the pre-spectrometer to reduce the flux of electrons in the main spectrometer by approximately seven orders of magnitude.

Inner surfaces

The main spectrometer has a large inner surface of $690\,\mathrm{m}^2$, additionally the inner-wire electrode has a surface area of $650\,\mathrm{m}^2$ [Val10]. Two processes can be distinguished: secondary emission processes and field electron emission.

Secondary emission processes can occur if a high-energetic particle hits the vessel and produces secondary electrons which reach the inner spectrometer surface. Muons are a likely candidate. However, recent measurements have shown that muon-induced processes do not contribute significantly to the background of the KATRIN experiment [Lin15].

Field emissions occur when large electric fields arise near surfaces. Data of the first commissioning phase (SDS-I) has shown that field electron emission only occurs if the potential difference between the inner-wire electrode and the main spectrometer vessel is raised above $\Delta U \geq 270\,\mathrm{V}$ [Sch14].

Radioactive decays

Radioactive decays at the spectrometer surface are able to produce high energetic electrons. These electrons can penetrate the flux tube under specific circumstances and contribute to the background. Additionally there are two radioactive elements which can contribute to the background by producing stored electrons stemming from radioactive decays and the processes accompanying them. Tritium and radon are of special importance as they penetrate the sensitive volume of the main spectrometer.

Electrons can be stored in the spectrometers due to the magnetic bottle effect. Once trapped, these electrons can produce more electrons via a subsequent ionisation of residual gas molecules. The primary electrons are stored until the storage conditions are broken - for example by a reduction of energy under a MAC-E filter specific threshold. The cooled down electrons are then accelerated by the retarding potential and cannot be distinguished from the signal electrons any more.

Tritium which leaves the WGTS and passes through the transport section reaches the spectrometers where tritium β-decays occur. The produced electron can be stored and ionize residual gas atoms thus contributing to the background. This emphasizes the importance of the transport section for the retention of tritium.

The α-decay of radon is especially important because radon is a volatile noble gas. Hence, it can emanate from surfaces and move freely through the tank and penetrate the flux tube. Its motion is not influenced by the electromagnetic fields because it is neutral implying that electromagnetic shielding is irrelevant for its motion. When an α-decay of radon occurs while the radon atom resides inside of the flux tube the produced electrons can be stored and create additional electrons by ionisations.

The background induced by stored particles is not Poisson distributed. The reason for its non-Poissonian nature is the correlation of the occurrence of the secondary electrons which results in time-intervals of elevated background. The non-Poissonian nature of the background induced by stored particles causes the sensitivity to worsen more than for poisson-distributed backgrounds [Mer12] [Wan13]. This emphasizes the importance of the suppression of radon-induced backgrounds in particular. This thesis investigates the passive suppression of the radon-induced background by liquid nitrogen cooled copper baffles. Additional active measures considered by the KATRIN collaboration are the utilisation of electron cyclotron resonance [Mer13], or the utilization of static and pulsed electric dipoles or magnetic pulses [Wan13].

3. Passive Reduction of radon-induced backgrounds in the KATRIN main spectrometer

In order to achieve the sensitivity of $200\,\mathrm{meV}$ the KATRIN experiment needs a very low background rate. Previous analyses have shown that stored electrons are a major source of background in the KATRIN experiment [Sch14] [Goe14] (section 3.1). One source of stored electrons is the α-decay of radon isotopes [Mer12] (section 3.2). In the KATRIN main spectrometer there are several sources which emanate radon [Goe12] (section 3.3). As a means to suppress the radon-induced background, liquid-nitrogen cooled copper baffles were installed in the main spectrometer [Goe14] (section 3.4). The liquid-nitrogen supply needed for these baffles is complex due to the high voltage environment. Therefore special thermal and high voltage insulating feed-throughs have been developed (section 3.5).

3.1 Background induced by stored particles in a MAC-E filter

The movement of stored charged particles in a MAC-E filter can be split into three parts: the gyration, the magnetron drift and the movement within a magnetic bottle.

Gyration

Charged particles in magnetic fields experience the Lorentz force. The Lorentz force results in charged particles moving on a corkscrew path along the guiding centre which is parallel to the magnetic field. This motion is called gyration. The gyration is shown schematically on the right hand side figure 3.1.

Magnetron drift

The magnetron drift is a drift of the guiding centre. It doesn't vanish if either $\vec{E}$ or $\nabla\vec{B}$ are not perpendicular to $\vec{B}$. The resulting velocity $\vec{v}_{mag}$ of the electron can be calculated.

$$\vec{v}_{mag} = \vec{v}_{\vec{E}\times\vec{B}} + \vec{v}_{\nabla B} \tag{3.1}$$

$$= \frac{1}{B^2}\cdot\vec{E}\times\vec{B} + \frac{E_\perp + 2\cdot E_\parallel}{e\cdot B^3}\cdot\nabla\vec{B}\times\vec{B} \tag{3.2}$$

with the electric field $\vec{E}$, the magnetic field $\vec{B}$, the longitudinal energy of the electron $E_\parallel$, the transversal energy of the electron $E_\perp$ and the elementary positive charge e [Wan13]. In case of

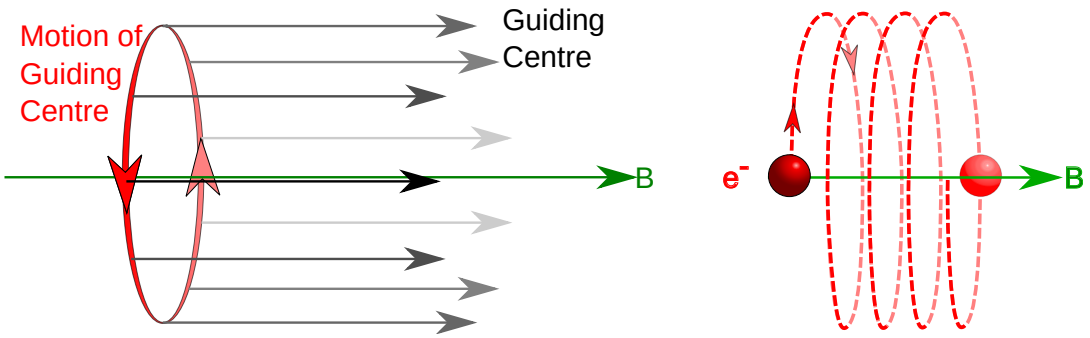

Figure 3.1: **Magnetron drift and gyration of an electron in a magnetic field. Left hand side:** The magnetron drift leads to a rotation of the guiding centre of the electron around the symmetry axis of the MAC-E filter. **Right hand side:** Electrons in a magnetic field gyrate due to the Lorentz force. With an additional drift the trajectory of the electron resembles a corkscrew.

axially symmetric fields only azimuthal drifts are possible. Without axial symmetry there is an additional radial drift. The magnetron drift of the guiding centre is visualized on the left hand side of figure 3.1.

Magnetic bottle

A MAC-E filter measures the energy of a particle with an electric retarding potential (see section 2.3.3). The alignment of the electron velocities is reached by a decrease of the magnetic field by four orders of magnitude from the entrances of the main spectrometer to its centre. This gradient also acts as a magnetic bottle which enables the storage of charged particles [Mer12]. It consists of two opposing magnetic mirrors which restrict the movement of charged particles in magnetic fields.[Hig08].

In the simplified case of an adiabatic motion the charged particles are guided by the Lorentz force. The part which is important for the magnetic mirror effect is the decelerating force $F_{\parallel}$.

$$\vec{F}_{\parallel} = -\frac{\partial}{\partial s}(\mu \cdot \vec{B}) \tag{3.3}$$

$$\mu = \frac{\frac{1}{2} \cdot m \cdot V_{\perp}^2}{B} = \frac{E_{\perp}}{B} \tag{3.4}$$

with the orbital magnetic moment μ, the transverse energy $E_{\perp}$ of the charged particle with mass m in a magnetic field B with orientation s. In the adiabatic approximation μ is conserved. This implies that the transverse energy of the charged particle has to increase accordingly if it reaches higher magnetic fields . Because of the assumption of adiabaticity the energy is conserved and the increase of $E_{\perp}$ needs to be compensated by a decrease of $E_{\parallel}$. If the increase of the magnetic field is high enough the charged particle cannot pass the magnetic mirror ($E_{\parallel} \rightarrow 0$) and is ultimately reflected back due to the force $F_{\parallel}$. With two magnetic mirrors blocking the particle on both sides, the charged particle is unable to leave and is trapped within this magnetic bottle.

However, in reality the approximation of adiabaticity is impeded by a low magnetic fields, high starting angles and high kinetic energies of the charged particle [Wan13]. The electromagnetic field configuration of the KATRIN main spectrometer stores electrons with energies ranging from $1\,\mathrm{eV}$ up to $100\,\mathrm{keV}$ at the analysing plane. The storage conditions can be broken by loosing too much energy or a scattering process resulting in a change of the angle. More details can be found in [Wan13].

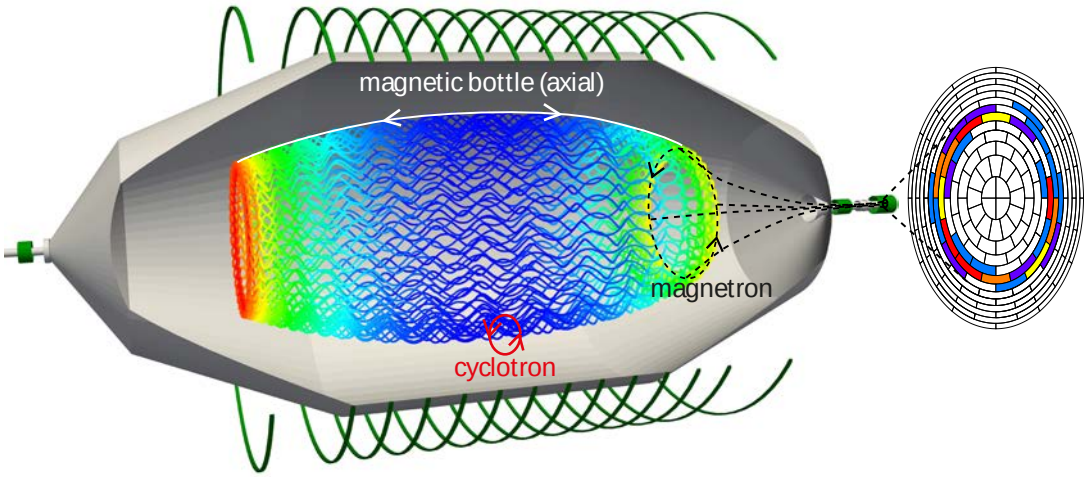

Figure 3.2: **Motion of a charged particle in a MAC-E filter** The motion of charged particles in an electromagnetic field can be explained by the superposition of gyration, magnetron drift and confinement in a magnetic bottle. The gyration is a rotation around the guiding centre which is parallel to the magnetic field lines. The magnetron drift is a rotation of the guiding centre around the symmetry axis of the MAC-E filter. The magnetic bottle consists of two mirrors, which a stored particle cannot pass. The picture is taken from [Bar14].

Resulting motion of a charged particle in a MAC-E filter

The motion of a charged particle in a MAC-E filter consists of a rapid gyration ($t_{\mathrm{gyration}} \approx 10^{-8}\,\mathrm{s}$), the back and forth motion in the magnetic bottle ($t_{\mathrm{bottle}} \approx 10^{-5}\,\mathrm{s}$) and a slow magnetron drift ($t_{\mathrm{magnetron}} \approx 10^{-4}\,\mathrm{s}$) [Mer12]. The combination of these three effects yields the trajectory for the charged particle in a MAC-E filter (see figure 3.2). During this motion the stored primary particle will scatter off of residual gas and ionize it. Due to the magnetron drift of stored particles the ionizations take place in a ring segment of the flux tube. The generated secondary electrons can fulfil the storage condition and be stored themselves. Otherwise the electrons will leave the MAC-E filter and can be detected. These secondary electrons will be distributed in a ring-like structure since these electrons are guided to the detector along the magnetic field lines after the ionization processes, which are ringlike distributed themselves.

3.2 Electron emission accompanying α-decays of radon

The α-decay was first described by Ernest Rutherford [Rut99]. Several years later he showed that the decay resulted in the emission of a helium ion. Therefore, an α-decay reduces the mass number A by 4 and the atomic number Z is reduced by 2.

$$ {}^{A}_{Z}X \rightarrow {}^{A-4}_{Z-2}Y + {}^{4}_{2}He \tag{3.5} $$

The α-decays of $^{219}\mathrm{Rn}$ and $^{220}\mathrm{Rn}$ into $^{215}\mathrm{Po}$ and $^{216}\mathrm{Po}$ are accompanied by the emission of electrons. The electrons are emitted due to different processes: shell-reorganization, shake-off, atomic relaxation and internal conversion (figure 3.3). These processes yield electrons at different energies ranging from $E \approx 1\,\mathrm{eV}$ to $E \approx 100\,\mathrm{keV}$. The probability to emit a number of electrons has a maximum at two emitted electrons and has a gradually decreasing tail for higher electron numbers [SD65].

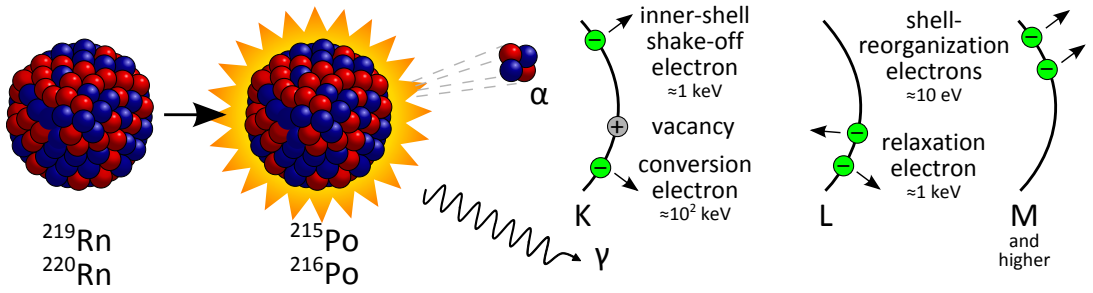

Figure 3.3: **Sketch of electron emission accompanying the α-decay of ^{219}Rn and ^{220}Rn.** ^{219}Rn decays into ^{215}Po and ^{220}Rn decay into ^{216}Po. During the α-decay of radon electrons are emitted. There are shell reorganization electrons, shake-off electrons, atomic relaxation electrons and internal conversion electrons. For each process the magnitude of the electron energy is given. Modified figure from [Mer12].

Shell reorganisation electrons

Because of an α-decay the nuclear charge is reduced by two. This reduction of the nuclear charge is counterbalanced by the emission of two electrons which are called shell reorganization electrons. The electrons in outer shells have a higher probability to be emitted than the electrons in inner shells due to the velocity distribution. Compared to the velocity of the α particle $v_\alpha \approx 10^7 \frac{\mathrm{m}}{\mathrm{s}}$ the inner shell electrons (K, L, M shell) have high velocities ($\frac{v_\alpha}{v_e} \approx 0.1$). Therefore the change of the nuclear charge is perceived as slow and the process is largely adiabatic [Fre75]. The outer shell electrons in contrast have lower velocities ($\frac{v_\alpha}{v_e} \approx 10$) and the change of the nuclear charge is perceived as abrupt resulting in the emission of outer shell electrons. This means that the shell reorganization electrons will originate primarily from the outer shells. The shell reorganization electrons are low energetic ($E \approx 10\,\mathrm{eV}$).

Shake-off electrons

Shake-off electrons are emitted if the α-particle interacts electromagnetically with an electron. Due to the high velocity of the inner shell electrons, the interaction probability of the α-particle is increased while it is decreased for outer shell electrons. Depending on the energy transfer the electron can either be elevated into a higher shell or become unbound. The unbound electron can have an energy ranging from a few eV up to tens of keV.

Internal conversion electrons

A radon atom decays into Polonium. The resulting Polonium atom has a non-vanishing probability to reside in an excited state. The Polonium atom then de-excites into the ground state by either emitting a photon or interacting electromagnetically with a shell electron. This is only possible if there is an electron with a non-vanishing wave-function in the nucleus. This so-called internal conversion electron has a energy of several hundred keV for ^{219}Rn and ^{220}Rn $\alpha-$decays. The $\alpha-$decay of ^{220}Rn into ^{216}Po can only produce one excited state which has a low probability [Wu07]. The $\alpha-$decay of ^{219}Rn into ^{215}Po, on the other hand, can produce multiple excited states and an excited state is more probable [Bro01].

Atomic relaxation

The emission of shake-off electrons and internal conversion electrons leaves vacancies in inner shells. These vacancies are filled by electrons from higher shells and the surplus energy is usually released via a photon. Alternatively the energy can be transferred to an electron which then is ejected [Mei22] [Aug23]. If the electron which fills the vacancy originates from a different shell the emitted electron is called an Auger electron. If the electron filling the vacancy originates from a

higher subshell the emitted electron is called a Coster-Kronig electron [CK35]. Atomic relaxation itself can create vacancies thus allowing for further atomic relaxations. In the case of Polonium the electrons ejected by atomic relaxations have a maximal energy of roughly $93\,\mathrm{keV}$ [Wan13].

Resulting energy distribution

These processes yield electrons with energies from a few eV to hundreds of keV [Wan13]. Higher energetic electrons have a higher influence on the background rate since they are able to create many secondary electrons. More details can be found in [Wan13].

3.3 Possible sources of radon in the KATRIN main spectrometer

There are three different decay chains including radon: the decay chains of Thorium $^{232}\mathrm{Th}$ (includes $^{220}\mathrm{Rn}$), Actinium $^{227}\mathrm{Ac}$ (includes $^{219}\mathrm{Rn}$) and Uranium $^{238}\mathrm{U}$ (includes $^{222}\mathrm{Rn}$) (see Appendix A).

$^{222}\mathrm{Rn}$ has a long half life ($T_{\frac{1}{2}} = 3.823\,\mathrm{d}$) which means that the vast majority of $^{222}\mathrm{Rn}$ is pumped out of the spectrometer ($t_{\mathrm{pump}} \approx 360\,\mathrm{s}$) by turbo molecular pumps (TMPs) before it decays [Wan13]. The half-lives of $^{220}\mathrm{Rn}$ ($T_{\frac{1}{2}} = 55.6\,\mathrm{s}$) and $^{219}\mathrm{Rn}$ ($T_{\frac{1}{2}} = 3.96\,\mathrm{s}$) however are short and most of the radon won't be pumped out of the spectrometer before it decays.

The three non-evaporable getter (NEG) pumps in the pump ports are the major source of $^{219}\mathrm{Rn}$ [Goe14] (figure 3.4 blue). The NEG pumps consist of roughly 3000 strips with a large specific surface area of $1500\,\frac{\mathrm{cm}}{\mathrm{g}^2}$ [Goe14]. The effective surface area of the getter material is so large due to the porosity of the NEG material (figure 3.5 b). The increased surface also enhances the probability that radon can desorb from the NEG strips into the vacuum to 0,1% [Goe12]. The NEG material used is SAES[1] type St707K getter material, which is compression bonded on constantan (55% Copper, 45% Ni) strips. The NEG material is made out of 70% Zirconium, 24,6% Vanadium and 5,4% Iron [BC95]. Additionally it contains trace amounts of Uranium ($^{235}\mathrm{U}$). The decay chain of Uranium includes the long-lived isotopes Protactinium ($^{231}\mathrm{Pa}$) and Actinium ($^{227}\mathrm{Ac}$) and the critical radon isotope $^{219}\mathrm{Rn}$. During the production process $^{227}\mathrm{Ac}$ is removed [Fra10]. This cuts off the decay chain and restricts the rate of radon production to the rate of decays of $^{231}\mathrm{Pa}$ ($T_{\frac{1}{2}} = 32\,760\,\mathrm{y}$) since the half-lives of the elements which are in the decay chain and are between $^{231}\mathrm{Pa}$ and $^{219}\mathrm{Rn}$ are rather short lived [Fra10]. The estimation of the $^{219}\mathrm{Rn}$ activity at the end of 2014 is $2.75\,\frac{\mathrm{Bq}}{\mathrm{kg}}$ [2]. These values allow for an estimation of the $^{219}\mathrm{Rn}$ emanation rate from the NEG pump $E_{^{219}\mathrm{Rn},estimate} \approx (0.165 \pm 0.030)\,\frac{\mathrm{Rn-decays}}{\mathrm{s}}$.

The other radon isotope of concern is $^{220}\mathrm{Rn}$ emanating from the main spectrometer vessel or its welds [Goe14]. The stainless steel main spectrometer vessel may contain trace amounts of $^{232}\mathrm{Th}$ despite the careful screening. A first estimation is possible by extrapolating from the measurements taken at the pre-spectrometer. This results in $(0.08 \pm 0.06)\,\frac{\mathrm{Rn-decays}}{\mathrm{s}}$ [Goe14].

The straightforward solution of removing the NEG pumps to remove the main radon source is not feasible since the NEG pumps ensure that the vacuum requirements are fulfilled. The main spectrometer vessel as a possible radon source can't be avoided, too. A solution to get rid of the radon-induced background has to be implemented.

3.4 Radon-induced background and suppression by the liquid-nitrogen cooled copper baffles

The passive suppression of radon-induced background by liquid-nitrogen cooled copper baffles is discussed in section3.4.1. Moreover, the corresponding liquid-nitrogen supply system is discussed in section 3.5 with focus on the high voltage separator.

[1] Saes Getters S.p.A., Viale Italia 77, 20020 Lainate (Milan), Italy, http://www.saesgetters.com

[2] $\mathrm{Surface} = 2.3\,\frac{\mathrm{Bq}}{\mathrm{kg}} + 0.3\,\frac{\mathrm{Bq\,y}}{\mathrm{kg}} = 2.75\,\frac{\mathrm{Bq}}{\mathrm{kg}}$ (values taken from [Goe14])

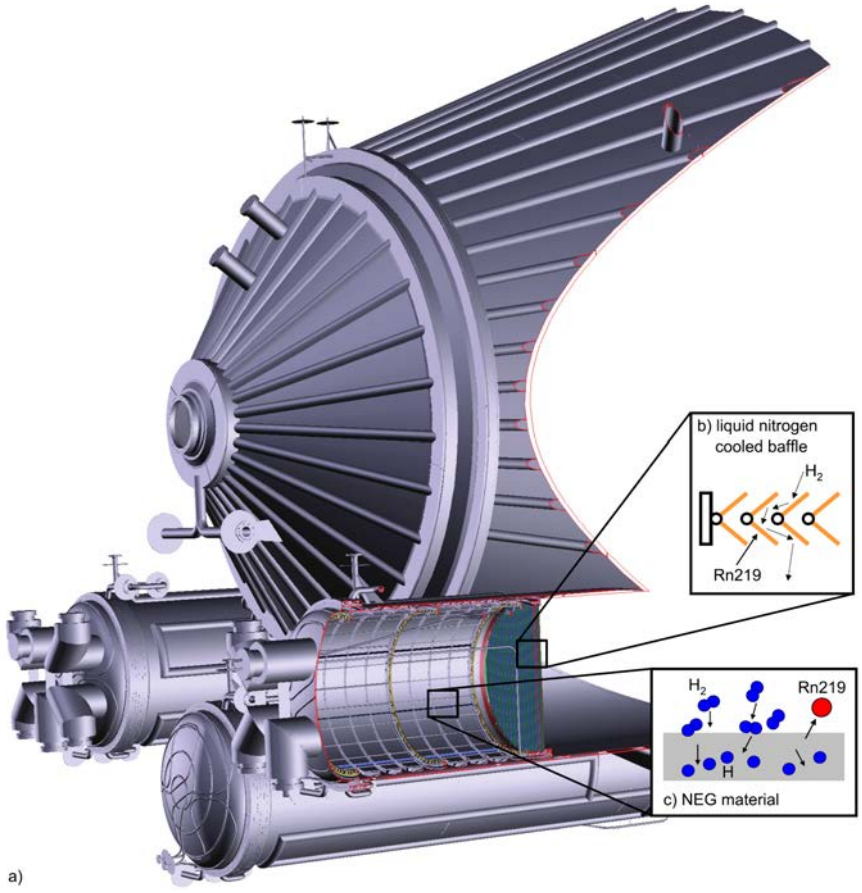

Figure 3.4: **Sketch of the KATRIN main spectrometer including the NEG pumps.** (a) The positions of the one of the NEG-pumps is shown (blue). In addition, the baffle is shown (green). (b) The liquid-nitrogen cooled copper baffle blocks the direct line of sight between the NEG strips and the main spectrometer. (c) The NEG material adsorbs hydrogen thus pumping the spectrometer. In addition, radon atoms desorb from it. Figure taken from [Goe14]

3.4.1 The liquid-nitrogen cooled copper baffles

The liquid-nitrogen cooled copper baffles consist of V-shaped copper plates. They reduce the radon-induced background by cryosorption of radon atoms. The KATRIN main spectrometer has three pump ports which are equipped with liquid-nitrogen cooled copper baffles. Each baffle consists of V-shaped copper plates which are connected to pipes welded to a ring pipe. Liquid nitrogen flows through this ring-pipe cooling the holding structure and the baffle to liquid-nitrogen temperatures.

The positioning of the baffles is chosen to block the direct line of sight between the NEG strips and the main spectrometer. This way the radon which emanates form the NEG strips has to hit the baffle at least once before reaching the sensitive volume in the main spectrometer. At the moment pump port 2 and 3 are equipped with NEG strips and pump port 1 is not. The final setups includes NEG strips in pump port 1 as well. This way the lowest pressure possible is reached.

The temperature of the baffles is monitored by four temperature sensors for each baffle (see figure 3.6). One sensor is attached to an outer baffle plate, while the other three sensors reside on the central V-shaped plate. The three sensors are located near the top, the middle and the bottom of the central plate.

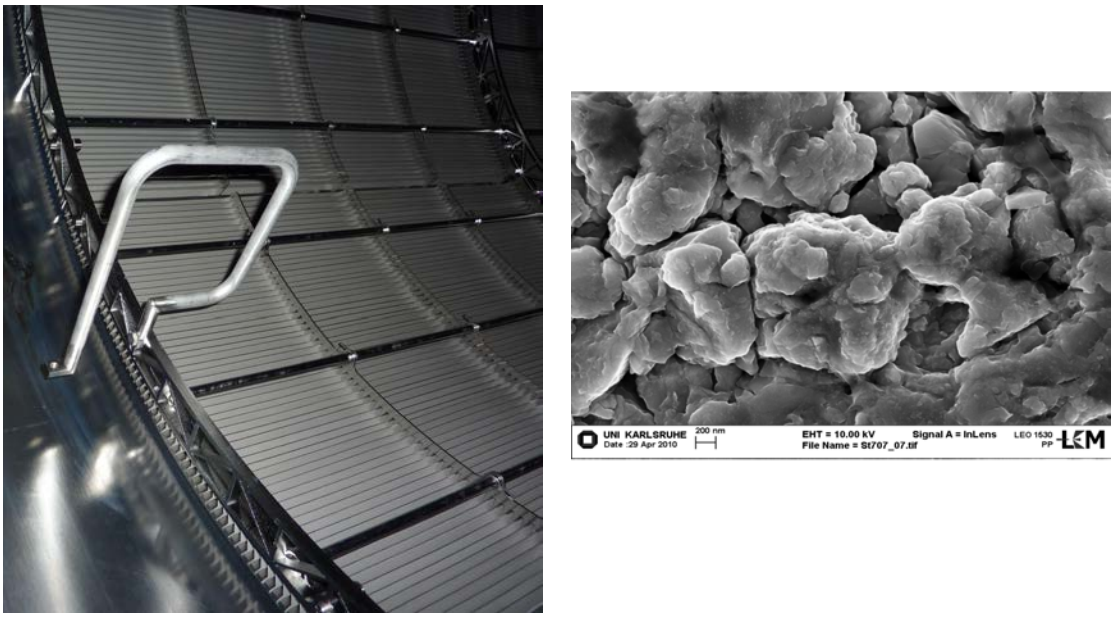

Figure 3.5: **NEG strips. Left hand side:** The NEG strips in one pump port are shown. Picture provided by H. Frenzel. **Right hand side:** The porous surface of the NEG material can be seen. The picture was taken with a scanning electrode microscope at the LEM of KIT.

3.4.2 Mean desorption time of radon from a copper surface

The mean time a cryosorbed atom stays on a cold surface is called mean residence time. It depends on the temperature of the surface and material properties. The mean desorption time τ_{des} is given by a simple exponential function:

$$\tau_{\mathrm{des}} = \tau_0 \cdot e^{-\frac{H_{\mathrm{des}}}{R \cdot T}} \tag{3.6}$$

where τ_0 is the oscillation period, which is related to the maximal phonon frequency ν_0 by $\tau_0 = {}^1/_{\nu_0}$, H_{des} is the desorption enthalpy, R is the gas constant and T is the temperature. The desorption enthalpy is assumed to be the same as the adsorption enthalpy as radon is not expected to form chemical bonds since it is a noble gas. The parameters H_{des} and τ_0 depend on the material of the adsorbent and the particle adsorbed. The particle of interest is radon. The surface property of the copper baffle is not determined definitely. There are three possible scenarios: a pure copper surface, an oxidised copper surface and a surface covered with a layer of water (ice). Oxidised copper has a surface of CuO after several months at air [Kei07]. With the relation

$$\nu_0 = \frac{k_b \cdot \theta}{h} \tag{3.7}$$

with $k_b = 8.62 \cdot 10^{-5}\,\frac{\mathrm{eV}}{\mathrm{K}}$ is the Boltzmann constant, $h = 4.14 \cdot 10^{-15}\,\mathrm{eV\,s}$ and θ being the Debye-temperature [EK00]. The Debye-temperature of CuO is $\theta = (390 \pm 10)\,\mathrm{K}$ [JET89]. It follows $\nu_0 = 8.12 \cdot 10^{12}\,\frac{1}{\mathrm{s}}$ and $\tau_0 = 1.2 \cdot 10^{-13}\,\mathrm{second}$. The parameters corresponding to these scenarios are summarised in table 3.1. The temperature dependence of the mean desorption times for these three scenarios is visualised in figure 3.7. It is evident that the surface condition of the adsorbent has a significant impact on the desorption time at a given temperature. When comparing the mean desorption time of an oxidised surface to a surface covered with ice at $T = 85\,\mathrm{K}$ the desorption time is reduced by four orders of magnitude. Therefore, it is desirable that the adsorption enthalpy of the copper baffles is not dominated by a surface covered with ice and that the temperature of the baffles is as low as possible.

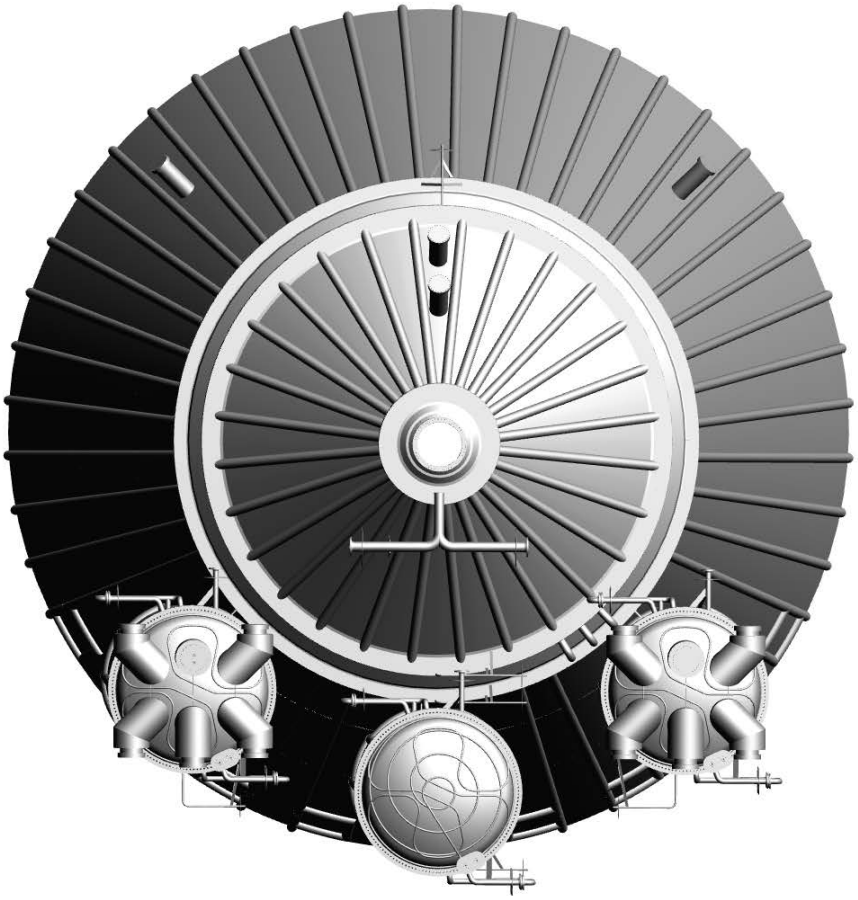

Pump Port	3	1	2
Baffle	yes	yes	yes
NEG	yes	no	yes

Figure 3.6: **The pump ports of the main spectrometer are depicted.** The three pump ports of the main spectrometer are depicted. All pump ports include a baffle while only pump ports 2 and 3 include NEG strips to obtain a better understanding of the source of the radon-induced background.

3.5 Liquid nitrogen supply system for the copper baffles

The liquid-nitrogen supply system is a crucial part of the KATRIN main spectrometer. Its function is to keep the copper baffles at stable liquid-nitrogen temperatures. This way, radon atoms are cryosorbed on the baffle and decay there instead of the sensitive volume of the magnetic flux tube. In the following the setup of the liquid-nitrogen supply system will be discussed (see section 3.5.1) with emphasis on the high voltage (HV) separator needed to insulate the main spectrometer from the liquid-nitrogen supply and exhaust lines, which are on ground (see section 3.5.2).

3.5.1 Setup of the liquid-nitrogen supply system

The liquid-nitrogen supply system is built to allow for the baffles 1 to 3 to be cooled to liquid-nitrogen temperatures 3.8. The system consists of three main parts: the liquid-nitrogen supply tank, the valve box and the high voltage separator. These components are connected via flexible vacuum insulated pipes (cryoflex transfer lines). The liquid-nitrogen supply tank is a product of Messer GmbH [3]. Its large capacity of 51 550 L ensures the continuous liquid-nitrogen supply. The

[3] Messer Group GmbH, Messer-Platz 1, 65812 Bad Soden, Germany

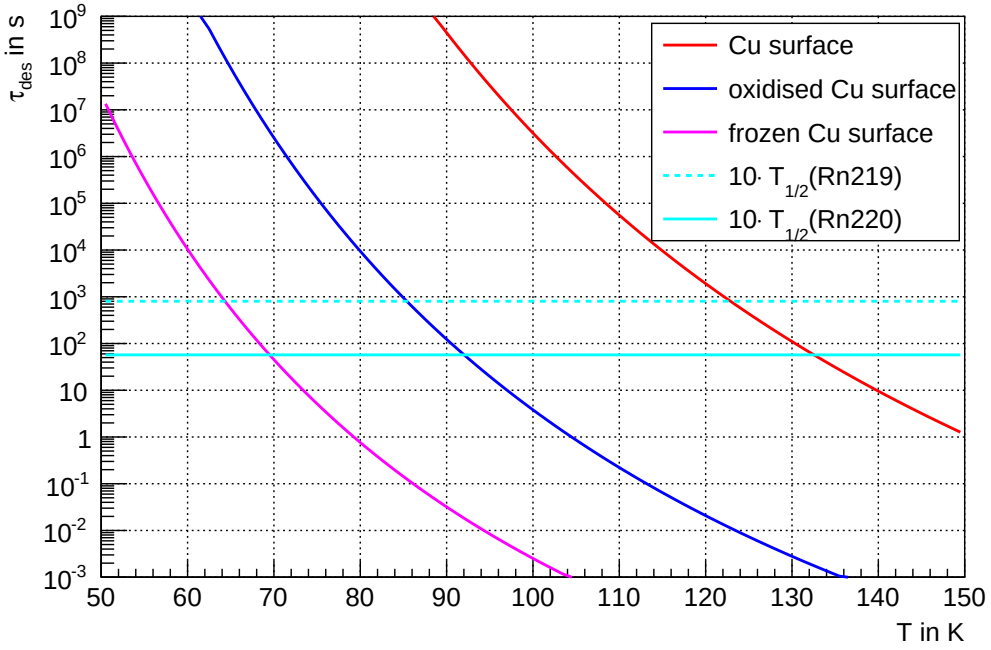

Figure 3.7: **Desorption time in dependency of the temperature.** The mean desorption time of radon is shown for surfaces of ice (magenta), oxidised copper (blue) and pure copper (red). In addition, ten times the half-life of both $^{219}\mathrm{Rn}$ and $^{220}\mathrm{Rn}$ are shown (cyan). Desorption times longer than ten times the half-life of the isotope are suppressed as well as the setup allows.

valve box allows to control the liquid-nitrogen flux to the copper baffles. It is built by Nexans [4]. More details about these components can be found in [Goe14].

Both inlet and outlet pipes pass the HV-separator which ensures that all components except the main spectrometer and a part of the HV-separator are on ground potential. The setup of the HV-separator will be discussed in more detail in section 3.5.2.

This is a crucial system as it allows for the baffles to be cooled during high voltage operation of the main spectrometer. This allows to suppress backgrounds induced by the α-decays of radon allowing to aim for the KATRIN background level of $10\,\mathrm{mcps}$. Each baffle can be cooled separately, which enables to study the influence of each baffle on the radon background (see section 5).

The liquid-nitrogen supply system is not able to cool the baffle to liquid-nitrogen temperatures ($77\,\mathrm{K}$) exactly but only to temperatures of about $86\,\mathrm{K}$. One reason is the elevated pressure in the liquid-nitrogen supply tank (approximately $1.5\,\mathrm{bar}$) resulting in a temperature of about $83\,\mathrm{K}$. This

[4] Nexans (Group's headquarters), 8, rue du Général Foy, 75008 Paris, France

Table 3.1: **The parameters describing several baffle surface conditions are summarised.** The desorption enthalpy H_{des} for radon and the maximal phonon frequency ν_0 are summarised for the baffle surface being ice, oxidised copper (CuO) or pure copper (Cu).

Surface	Period of oscillation τ_0 in $10^{-13}\,\mathrm{s}$	Desorption enthalpy H_{des} in $\frac{\mathrm{kJ}}{\mathrm{mol}}$
Ice	3 [EZG00]	-19.2 ± 1.6 [EZG00]
CuO	1.2 [JET89]	-26 [ES02]
Cu	1.5 [ES02]	-37 [ES02]

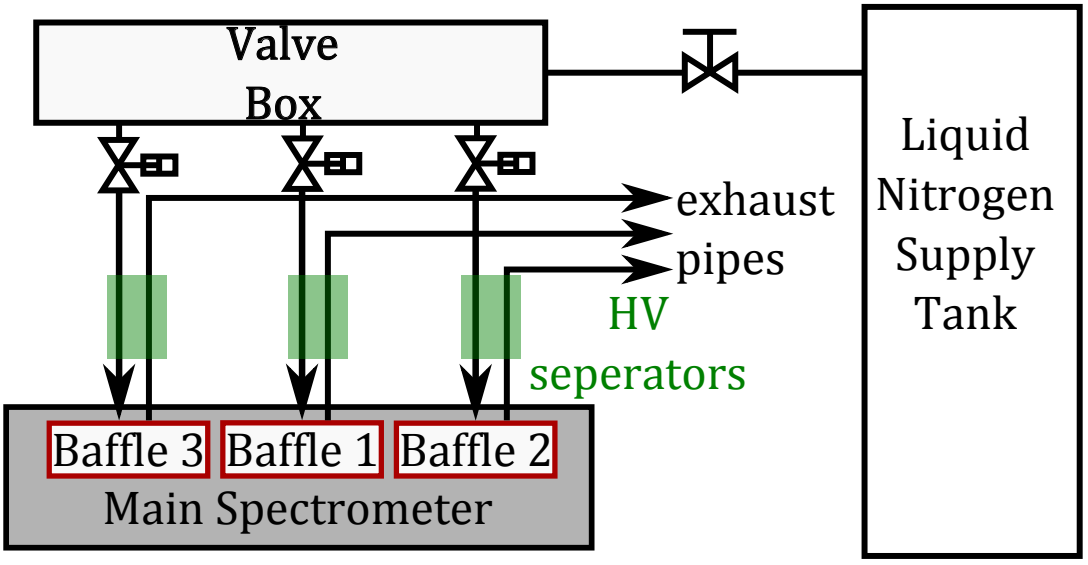

Figure 3.8: **Sketch of the liquid-nitrogen supply system.** The liquid-nitrogen supply system consists of three crucial parts: the supply tank, the valve box and the high voltage (HV) separators. Furthermore, it includes four valves to regulate the gas flow from the liquid-nitrogen supply tank to the valve box (V4), and from the valve box to the baffles (V1, V2, V3). The valve box distributes the liquid-nitrogen to the baffles and controls the flow to each one separately. The HV-separators are designed to insulate the valve box from the main spectrometer. This sketch is inspired by [Goe14, p124].

is close to the value measured by the temperature sensors (86 K). The remaining 3 K offset has several possible reasons. Firstly, the temperature sensors are not perfectly coupled to the baffle surface. Secondly, the baffles are not perfectly coupled to the liquid-nitrogen supply. Moreover, heat radiation from the main spectrometer vessel increases the temperature of the baffles, especially when the V-shaped baffle plates which face the vessel directly are concerned.

3.5.2 The high voltage separator

The HV-separator allows to constrain the high voltage to the main spectrometer residing in the KATRIN hall. This ensures safety, as only trained personnel has the keys to the KATRIN hall, therefore ensuring that no one - in particular external personnel - touches components carrying high voltage by accident.

Setup of the high voltage separator

The setup of the high voltage separator ensures the liquid-nitrogen supply while insulating all components beside the main spectrometer. The part of the HV-separator connected to the main spectrometer is on high voltage. In order to insulate all other components the liquid-nitrogen supply lines each include an insulator. This insulator is surrounded by vacuum ($p < 10^{-5}$ mbar) for thermal isolation. This was done to prevent icing and the possibility of leakage currents connected to icing [Goe14]. The setup chosen at KATRIN is depicted in figure 3.9. The high voltage separator can be divided into three parts: the bottom which is on high voltage, the middle which are insulators and the top which is on ground potential. The top simply contains the connections to both the TMP and the liquid-nitrogen pipes. In the middle of the HV-separator resides its core: the insulators. In the bottom part is the connection to the main spectrometer of the liquid-nitrogen supply. Furthermore, there is a tube which is covered with a rupture disk to prevent pressures which could endanger important components.

The high voltage insulation in vacuum under cryogenic conditions is of critical importance. This topic is still under investigation despite each of its subtopics (vacuum, cryogenics, high voltage)

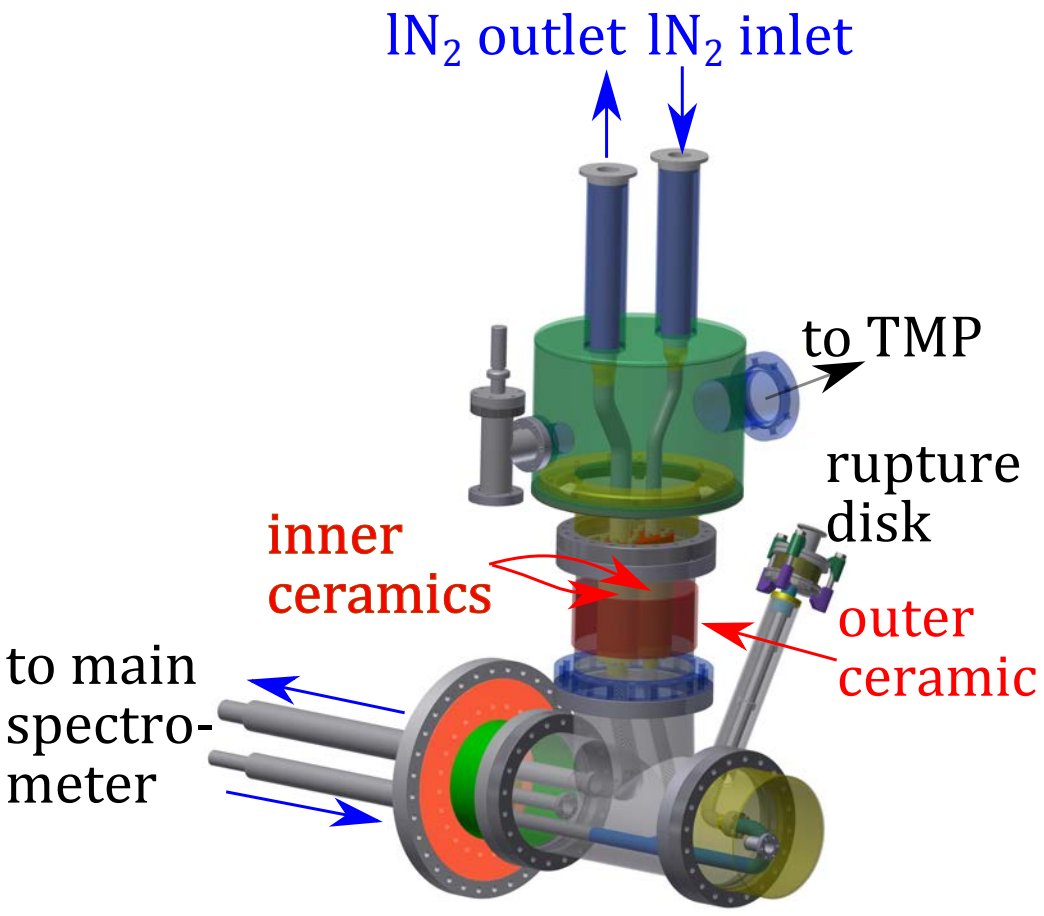

Figure 3.9: **Setup of the HV-separator.** The HV-separator has 6 openings. 4 openings are reserved for the liquid-nitrogen supply lines and 1 opening is reserved for the TMP creating a vacuum ($p < 10^{-5}\,\mathrm{mbar}$). Furthermore there is a pressure relieve covered with a rupture disk to prevent critical pressures. The two inner insulators integrated in the liquid-nitrogen supply line are enclosed by an outer ceramic.

being understood well separately. Especially the combination of high voltage and vacuum poses significant technical challenges [Lat95].

Design criteria for insulators in vacuum

The design criteria for insulators in vacuum have been studied extensively by many scientists. In summary 3 main guidelines have been created [WW95]:

- Minimise the electric field at the cathode triple junction to ensure that no free electrons are created in areas of high electric fields.
- Ensure that electrons are not focused on the surface of the insulators. On the one hand it is ensured that the surface is not damaged. On the other hand it is ensured that no further electrons are created and no ionised gas is created above the surface.
- Ensure that electrons which hit the surface are trapped. This guarantees that no cascade effects creep along the insulator to create delayed discharges.

All of the above guidelines are closely connected to the design of the insulator. Furthermore, it is emphasised that each insulator has to be designed for its specific operation and the way the insulators are conditioned.

In order to determine the usability of the insulators a test setup was used (see figure 3.10). The high voltage is applied to the lower part of the HV-separator reflecting the operating condition when it is connected to the main spectrometer. Furthermore, a Y-t-recorder is used to track the leakage current. Voltage breakthroughs can be heard acoustically by the voltage flash-over the $10\,\mathrm{M\Omega}$ resistor. Furthermore the Y-t-recorder tracks the occurrence of sparks. In total three different types of insulators were tested: glass fibre-reinforced plastic (GFP) insulators, ceramics and Babcock-Noell insulators.

Insulator 1: Glass fibre-reinforced plastic insulators

The glass fibre-reinforced plastic (GFP) insulators have a good high voltage design since the triple junctions are flat and their orientation is perpendicular to the insulation direction (see figure 3.11). The GFP insulator is gas-tight before and after slow thermal cycling to $77\,\mathrm{K}$. However, when the GFP insulator is at $77\,\mathrm{K}$ it is not airtight any more and leaks with a rate of approximately $0.02\,\frac{\mathrm{mbar\,l}}{\mathrm{s}}$. As the final KATRIN setup requires liquid-nitrogen cooled baffles and the GFP insulator is not airtight in this state it is impossible to use them. Therefore, an alternative is required.

Insulator 2: Ceramics

As a second approach ceramics from Allectra [5] were bought. These insulators do only barely pass with $20\,\mathrm{kV}$ applied after conditioning. It turns out that the problems arise due to effects at the junction between the insulator, the metal electrode and the vacuum, the so-called triple-junction. Furthermore, the triple junctions of the inner insulators of the HV-separator setup are of concern. This is verified by a test with teflon tape wrapped around the triple junctions of the inner ceramics multiple times to insulate this critical section specifically. The measurements show a significant increase of breakdown voltage to $25\,\mathrm{kV}$. In addition, COMSOL Multiphysics[6] simulations show that the electric fields are high at the dents of the metal welded on the insulators (see top of figure 3.13). It is conclusively proven that the problems of the Allectra ceramics originate from the triple junction.

On flat surfaces the critical electric field is $10^8\,\frac{\mathrm{V}}{\mathrm{m}}$ to $10^9\,\frac{\mathrm{V}}{\mathrm{m}}$. At dents, however, this value can be much lower. A simple idea is to shield these gaps by using a guard ring. This is also simulated with COMSOL Multiphysics (see bottom of figure 3.13). The idea of the guard rings is to focus the field lines on the bigger surface of a ring-shaped electrode instead of the sharp metal dents on the insulators. COMSOL Multiphysics simulations show that this idea improves the size of the electric field. Next, this idea was put to practice. In addition, the insulators were cleaned with acetone and baked out at $100\,^{\circ}\mathrm{C}$.

The result is not as positive as expected. The resulting setup showed no break-downs with a test voltage of $20.8\,\mathrm{keV}$ during the whole measurement time ($2\,\mathrm{h}$). However, only small increases to $22\,\mathrm{kV}$ lead to a breakdown. As literature suggests that the geometry of the insulator determines the breakdown voltage of the setup further tests with these insulators were stopped. Other insulators better suited for the specific conditions in the HV-separator are required.

3.5.3 Insulator 3: Lenz insulators

Based on the problems encountered the Babcock-Noell[7] insulators are a vast improvement 3.14. The triple junction has no sharp edges and is recessed. On short notice Dr. R. Lietzow from the Institute of Technical Physics of KIT provided us with six of these insulators. They were tested successfully at $35\,\mathrm{keV}$ which is sufficient for the usage during the second commissioning phase of the main spectrometer. For the final KATRIN setup $32\,\mathrm{keV}$ are needed for calibration

[5] Allectra GmbH, Traubeneichenstr. 62-66, D-16567 Schönfliess near Berlin, Germany
[6] COMSOL, Inc., 1 New England Executive Park, Burlington, MA 01803 USA
[7] Babcock Noell GmbH, Alfred Nobel Str. 20, 97080 Würzburg

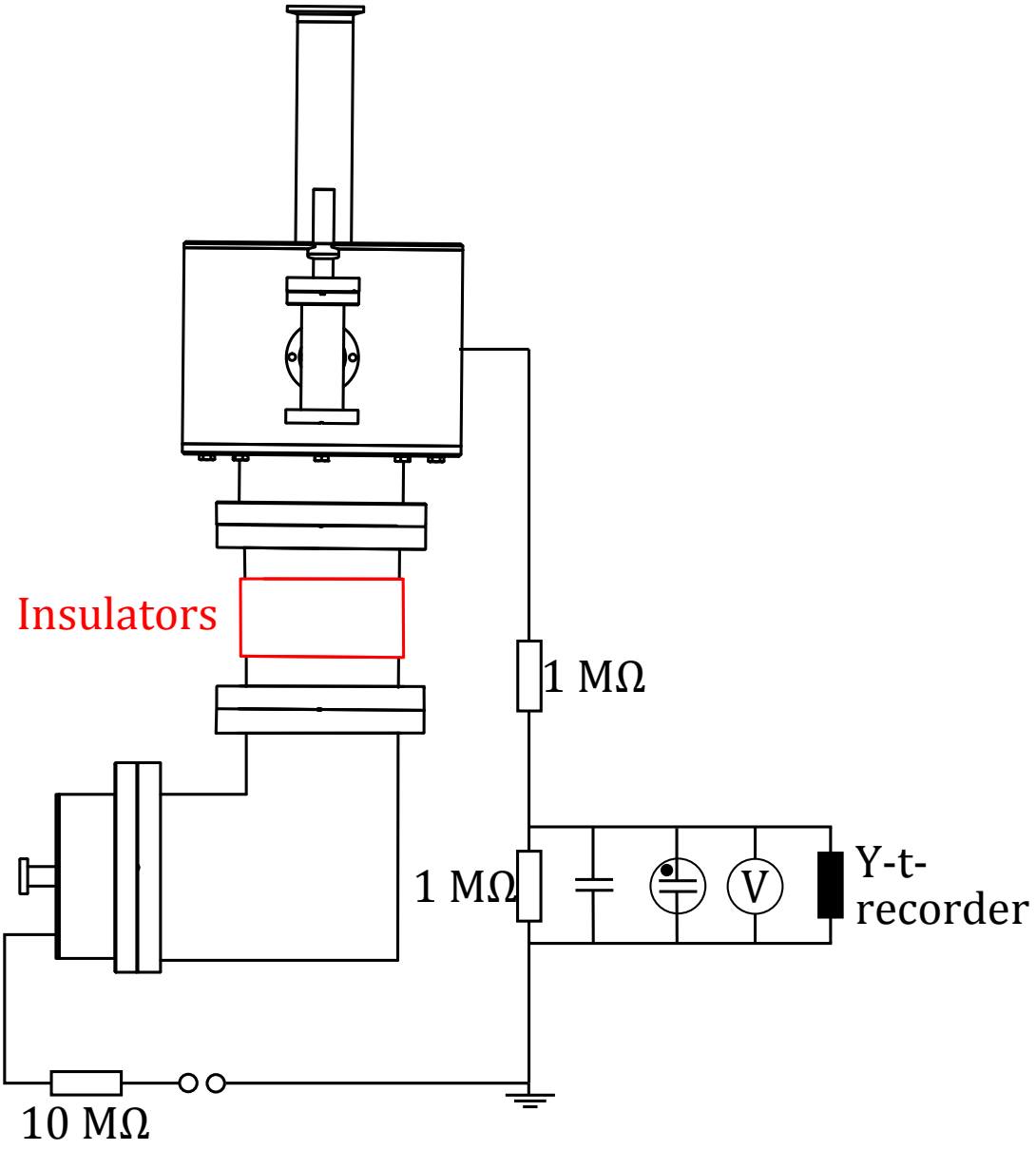

Figure 3.10: **Setup of the HV-separator for the determination of the breakdown voltage.** For the testing procedure the setup of the HV-separator is simplified by replacing the T-piece by a bent pipe. The high voltage is applied to the lower part of the HV-separator reflecting the future setup. When a breakdown occurs a current flow ensues. The leakage current is assessed by measuring the voltage drop at a resistor. In addition a glow lamp for over-voltage protection and a capacitor to suppress transients are connected in parallel. A voltmeter and a recorder which records the voltage on paper are used to monitor the leakage current.

Figure 3.11: **The GFP insulator.** One glass fibre-reinforced plastic insulator is shown. The flanges are made for indium seals.

measurements of the source with $^{83m}\mathrm{Kr}$. It is recommended to test the HV-separator at cryogenic temperatures, with a pressure smaller than $10^{-5}\,\mathrm{mbar}$ and high voltage of $32\,\mathrm{kV}$ for a day or to follow the recommendations of [Lat95] and test the insulators at the double voltage ($64\,\mathrm{kV}$) for 10 minutes.

3.5.4 Resulting HV-breaks at the main spectrometer

In the beginning two HV-separators equipped with the Allectra ceramics were connected to pump port 2 and 3. Both performed well. After two weeks of successful operation baffle 3 was warmed up to measure the background with only baffle 2 cold. Afterwards, baffle 3 was cooled down again. Approximately $1\,\mathrm{h}$ after the cool-down sparks were observed and traced back to the HV-break attached to pump port 3. The HV-separator was removed and reinstalled with Babcock-Noell insulators instead. The remaining HV-separator included Babcock-Noell insulators when it was first mounted to pump port 1.

In total the HV-separator connected to pump port 2 ran smoothly for four months until the measurement phase ended. The HV-separators with Babcock-Noell insulators were installed to pump ports 1 and 3 and worked fine for two and three months respectively.

The reliability of the HV-separators is crucial since it allows to measure with cooled baffles by liquid-nitrogen for arbitrary durations. On the one hand this allows to study the radon-induced background. On the other hand the remaining background with three cold baffles can be studied. This allows to gain important information on the nature of the background in the KATRIN main spectrometer.

3.5.5 Implications for other systems

The PAE shows discharges at $11\,\mathrm{kV}$ when the pressure is in the order of $10^{-11}\,\mathrm{mbar}$. By transferring the knowledge from this work Axel Müller found a possible explanation for this long-standing problem. It is proposed that field emissions at the tips of the aluminium foil on the perspex are the reason for these discharges.

Figure 3.12: **The insulator from Allectra.** The insulator from Allectra is made of ceramics (Al_2O_3). **top:** The ceramics are enclosed by two metal pipe sections. The triple-junction is at the intersection of the metal and the insulator. The brazing of the metal to the ceramics poses significant design disadvantages as the triple junction is right at the end of this dent. **bottom:** Triple junction covered with teflon tape. The teflon tape is held in place by cable ties.

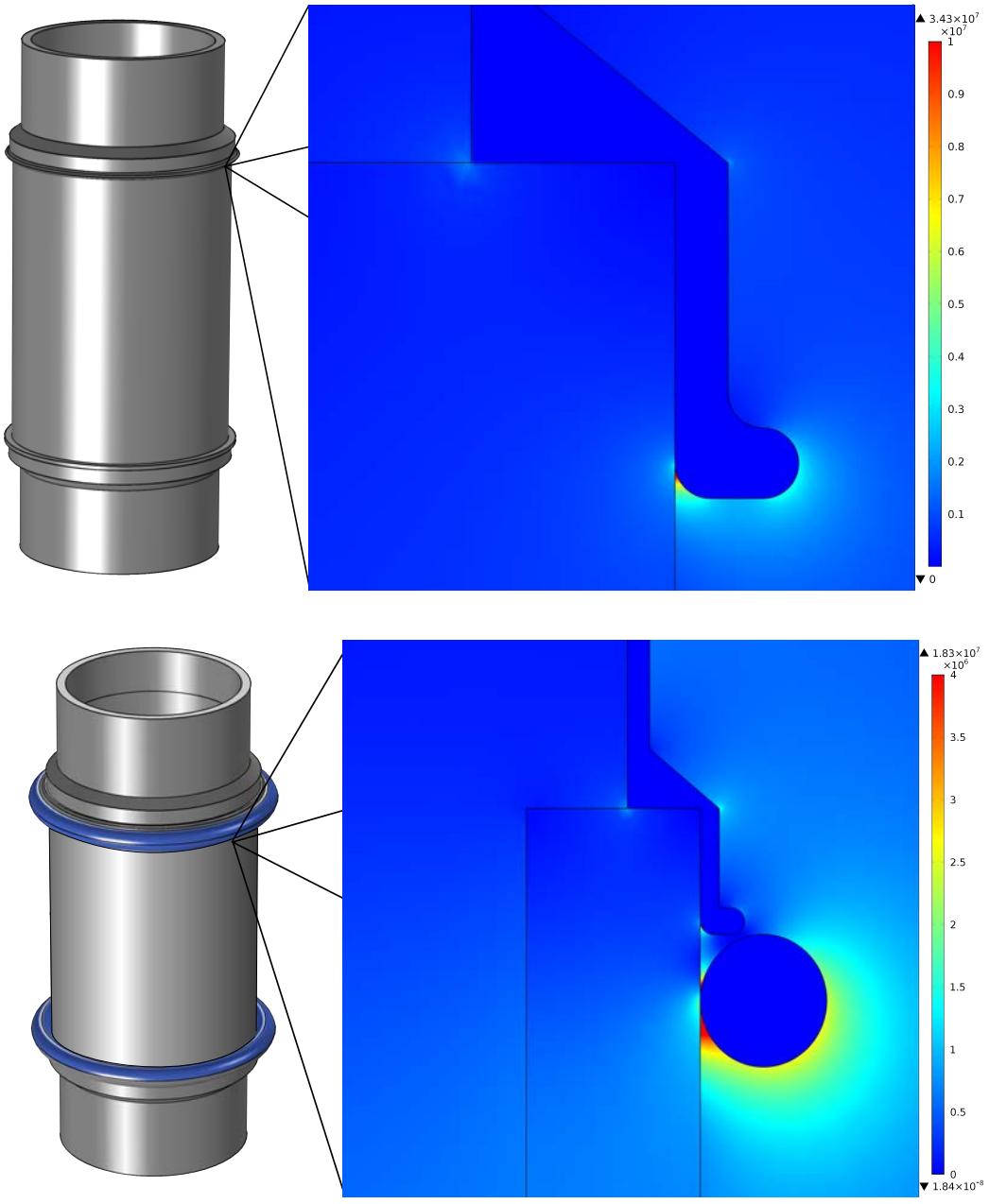

Figure 3.13: **COMSOL Multiphysics simulations of the electric field strength.** The electric field is critical for the breakdown voltage. Two scenarios are simulated. **Top:** The ceramic with the electrodes having a dent at the boundary between the electrode and the ceramic is shown. In addition, a zoom on the dent is shown with the electric field in $\frac{\mathrm{V}}{\mathrm{m}}$ as an overlay **Bottom:** The ceramic with additional copper rings shielding the dents is shown with a zoom on the boundary between the guard ring and the electrode. The maximal electric field is reduced roughly by a factor of 2. These simulations were performed in close cooperation with Alexander Jansen.

Figure 3.14: **The GFP insulator.** The insulators of the Babcock Noell GmbH. The triple junction is recessed to prevent voltage breakdowns.

4. Simulation of the suppression of radon-induced background by copper baffles

The background induced by radon α-decays depends on the temperatures of the liquid-nitrogen cooled copper baffles. In order to study the dependency, three increasingly complex simulations were performed. As a first approximation the model assumes the baffles to adsorb radon while never desorbing it (see section 4.1). This model was first developed in [Fra11] and [Goe14]. In the next model, a set of differential and integral equations are describing the desorption process numerically (see section 4.2). In the third model, a vacuum simulation, tailored for the specific needs of radioactive particles, was executed (see section 4.3). The modification of the vacuum simulation and the setup of the simulations was done by Marcel Krause. In section 4.4, the results of the different models are compared with each other.

4.1 A Simplified Model

Theory

The most basic model was first applied to the pre-spectrometer [Fra11] and can just as easily be applied to the main spectrometer as well [Goe14]. This approach describes three competing processes, leading to a reduction of the fraction of radon atoms in the main-spectrometer volume. Either the radon atom is pumped out by turbo-molecular pumps, adsorbed on by liquid-nitrogen cooled baffles or it decays. These processes are summarised in a flow chart (see figure 4.1). This approach neglects many aspects, among others the re-desorption of adsorbed radon. The theory is only valid if the mean desorption time is orders of magnitude higher than the lifetime of the radon isotope $\tau_{\mathrm{des}} \gg \tau_{\mathrm{Rn}}$. This statement is very strong. Since the baffle blocks the direct line of sight between the NEG material and the sensitive volume this statement implies that no radon atoms emanating from the NEG-material can contribute to the background. When the baffles are cooled to liquid-nitrogen temperatures the possible radon sources are restricted to the surface of the tank and components attached to it.

The transitions possible are depicted in figure 4.1 and can be expressed with a differential equation:

$$\frac{\mathrm{d}n_{\mathrm{MS}}(t)}{\mathrm{d}t} = -\left(\lambda_{\mathrm{ads}} + \lambda_{\mathrm{TMP}} + \lambda_{\mathrm{dec}}\right) \cdot n_{\mathrm{MS}}(t) \tag{4.1}$$

which leads to an exponential function $n_{\mathrm{MS}}(t)$. Here $n_{\mathrm{MS}}(t)$ is the fraction of particles in the main spectrometer volume at any given time t, $\lambda_{\mathrm{dec}} = {}^{1}/_{\tau_{\mathrm{dec}}}$ being the inverse of the lifetime of

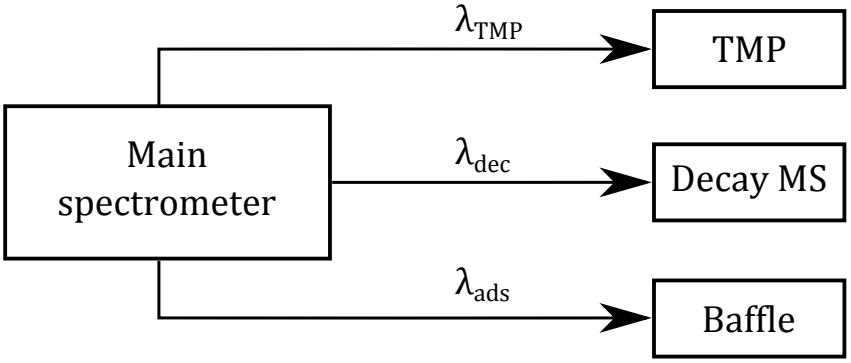

Figure 4.1: **The four possible states of radon in the Simplified Model:** The Rn-atoms either reside in the main spectrometer, they have been pumped out by the TMPs, they have been adsorbed on the baffle, or they have decayed in the main spectrometer. The transition between states included in the model are described by their respective transition rates (λ).

a radioactive isotope, $\lambda_{TMP} = {}^{S_{\mathrm{TMP}}}/_{V}$ being the fraction of the pumping speed S_{TMP} and the volume V which is pumped out and $\lambda_{ads} = {}^{k \cdot S_{\mathrm{Baffle}}}/_{V}$ is the fraction of the pumping speed of one baffle S_{Baffle} multiplied by the number of baffles $k \in \{1, 2, 3\}$.

(4.1) is solved by:

$$n_{\mathrm{MS}}(t) = e^{-(\lambda_{ads}+\lambda_{TMP}+\lambda_{dec})\cdot t} \tag{4.2}$$

Without TMPs and baffles ($S_{\mathrm{TMP}} = 0$, $S_{\mathrm{Baffle}} = 0$) the fraction of radon atoms decaying in the main spectrometer would be $100\,\%$. The probability P_{dec} for a radioactive atom to decay before it is pumped is:

$$P_{\mathrm{dec}} = n_{\mathrm{dec}} = \lambda_{\mathrm{dec}} \cdot \int_0^\infty n(t)\,\mathrm{d}t \tag{4.3}$$

$$= \frac{\lambda_{\mathrm{dec}}}{\lambda_{\mathrm{ads}} + \lambda_{\mathrm{TMP}} + \lambda_{\mathrm{dec}}} \tag{4.4}$$

$$= \left(1 + \frac{\tau_{\mathrm{dec}} \cdot (k_{\mathrm{Baffle}} \cdot S_{\mathrm{Baffle}} + S_{\mathrm{TMP}})}{V}\right)^{-1} \tag{4.5}$$

with the lifetimes of radon $\tau_{\mathrm{dec}} = {}^{1}/_{\lambda_{\mathrm{dec}}}$. The resulting efficiency of the suppression of radon α-decays in the main-spectrometer volume is:

$$\epsilon_{\mathrm{SM}} = 1 - P_{\mathrm{dec}} \tag{4.6}$$

Resulting efficiencies

The suppression efficiencies for radon-induced events obtained with (4.6) and (4.5) are summarised in table 4.1.

It is evident that $^{222}\mathrm{Rn}$ is no significant background source in the KATRIN experiment since its half-life is long compared to the pump-down time ${}^{1}/_{\lambda_{\mathrm{TMP}}}$. Therefore, it is not taken into account in

Table 4.1: **The efficiency of radon suppression for different configurations calculated with (4.5) is given.** The efficiency of radon suppression $\epsilon = 1 - P_{\mathrm{des}}$ depends on several parameters: the lifetime of the isotope τ_{des}, the pumping speed of 6 TMPs $S_{\mathrm{TMP}} = 3.51\,\frac{\mathrm{m}^3}{\mathrm{s}}$, the pumping speed of one baffle $S_{\mathrm{Baffle}} = 61.43\,\frac{\mathrm{m}^3}{\mathrm{s}}$ and $k_{\mathrm{Baffle}} \in \{1, 2, 3\}$ being the number of active baffles.

Rn isotope	lifetime τ_{des}	number of active baffles k	efficiency $\epsilon_{\mathrm{SM}} = 1 - P$
$^{219}\mathrm{Rn}$	5.71 s [MAB13]	0	1.6 %
		1	23.0 %
		2	36.8 %
		3	46.4 %
$^{220}\mathrm{Rn}$	80.2 s [Wu07]	0	18.5 %
		1	80.8 %
		2	89.1 %
		3	92.4 %
$^{222}\mathrm{Rn}$	5.5161 d [JS06]	0; 1; 2; 3	≈ 100 %

these calculations. Both $^{219}\mathrm{Rn}$ and $^{220}\mathrm{Rn}$ emanating from the main spectrometer or components directly attached to it, however, contribute significantly.

Due to its longer lifetime $^{220}\mathrm{Rn}$ is suppressed more efficiently than $^{219}\mathrm{Rn}$ for the same baffle configuration. For three cold baffles the suppression efficiency is 92.4 %. As a result even ^{220}Rn emanating from the spectrometer can be suppressed quite efficiently. For $^{219}\mathrm{Rn}$, however, at most a reduction by approximately 50 % is expected in this ideal model. A direct conclusion is that $^{219}\mathrm{Rn}$ can be suppressed the least and therefore would have the most impact.

In conclusion, the Simplified Model yields very quick results which rely only on few parameters. However, its validity is restricted to the specific scenario of an ideal baffle configuration. Important deductions are possible for ideal baffles: the $^{222}\mathrm{Rn}$ component is suppressed efficiently, radon isotopes emanating from the NEG material behind the baffles are suppressed completely, and $^{220}\mathrm{Rn}$ and $^{219}\mathrm{Rn}$ emanating from the main spectrometer are the most prominent threats.

4.2 Numerical Model of radon interactions with the liquid-nitrogen cooled baffle

The Numerical Model of radon interactions with the liquid-nitrogen cooled baffles is a further stage of the model presented in section 4.1. It is designed to study the contributions induced by radon emanating from the main spectrometer walls. In order to study the reduction efficiency of the baffle in dependence of the temperature, the model has to include the mean re-desorption time of radon adsorbed on a baffle (τ_{des}) as an additional parameter. It is connected to the temperature of the baffle via the relation presented in (3.6). The states and transitions of the model are summarised in figure 4.2. Since the radon atom can now either decay on the baffle or return back into the main spectrometer the set of equations describing this model becomes more complex.

Equations describing the model

This model relies on the description of decays and pumping processes by exponential functions as well. Furthermore, a differential equation is needed to describe the fraction of particles residing on the baffle.

As a starting point is is assumed again, that all radon atoms are emitted from the spectrometer walls at t=0 s. The fraction of radon α-decays $n_{\mathrm{dec}}(t)$, occuring inside the main-spectrometer volume

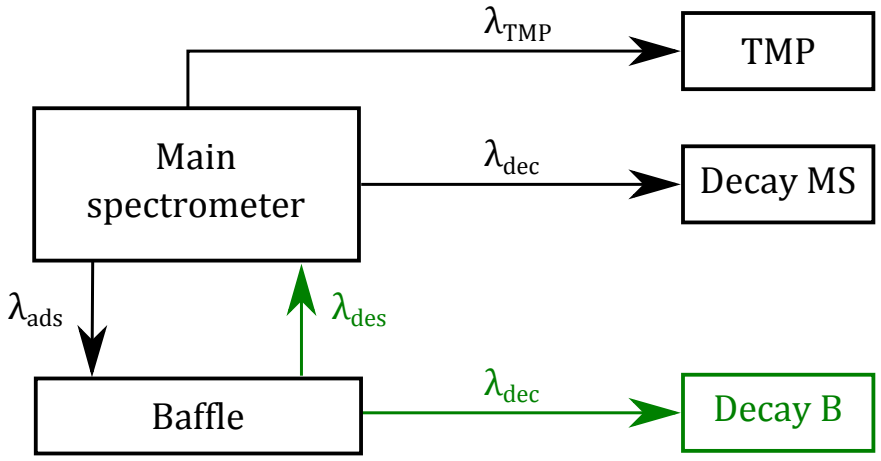

Figure 4.2: **The five possible states and transitions for radon emanating from the vessel in the Numerical Model.** There are two intermediate states: radon residing in the main spectrometer and radon being adsorbed on the baffle. Furthermore, there are three final states: The first one is for radon being pumped out, the second one for radon decaying in the main spectrometer, and the third one for radon decaying while sticking to the baffle. The possible paths and their respective transition rates (λ) are indicated by arrows. The additions to the Simplified Model (section 4.1) are coloured green.

during the time t after their emission from the main-spectrometer wall is given by:

$$n_{\mathrm{dec}}(t) = \lambda_{\mathrm{dec}} \cdot \int_0^t n_{\mathrm{MS}}(t')dt' \tag{4.7}$$

where $n_{\mathrm{MS}}(t')$ is the fraction of radon atoms, which are in the main spectrometer volume at the time t'. For the limit of infinitely large times (4.7) becomes the efficiency of radon suppression.

$$\epsilon = 1 - \lim_{t\to\infty} n_{\mathrm{dec}}(t) \tag{4.8}$$

$$= 1 - \lambda_{\mathrm{dec}} \cdot \int_0^\infty n_{\mathrm{MS}}(t')dt' \tag{4.9}$$

This is analogous to the Simplified Model, where $n_{\mathrm{MS}}(t')$ is an exponential function in the (see (4.2)). However, here an additional addend is needed, increasing by the fraction of radon atoms re-desorbed from the baffle surface n_{des} until time t.

$$n_{\mathrm{des}}(t) = \lambda_{\mathrm{des}} \cdot \int_0^t n_{\mathrm{Baffle}}(t')\,\mathrm{d}t' \tag{4.10}$$

where $n_{\mathrm{Baffle}}(t')$ is the fraction of radon atoms which reside on the baffle at the desorption time t'. After the desorption at time t' the radon atoms again behave as in (4.2). Hence, they are subject to the pumping and decay processes for the remaining time-interval $\Delta t = t - t'$. In order to determine the fraction of radon atoms which still reside in the main spectrometer after a time t $n_{\mathrm{des,\,MS}}(t)$ the multiplicand $\exp\left(-\left(\lambda_{\mathrm{ads}} + \lambda_{\mathrm{dec}} + \lambda_{\mathrm{TMP}}\right) \cdot \Delta t\right)$ needs to be applied :

$$n_{\mathrm{des,\,MS}}(t) = \lambda_{\mathrm{des}} \cdot \int_0^t n_{\mathrm{Baffle}}(t') \cdot e^{-(\lambda_{\mathrm{ads}}+\lambda_{\mathrm{dec}}+\lambda_{\mathrm{TMP}})\cdot(t-t')}\mathrm{d}t' \tag{4.11}$$

All things considered, the total fraction of radon atoms in the main spectrometer is the sum of (4.2) and (4.11):

$$n_{\mathrm{MS}}(t) = n(t) + n_{\text{des, MS}}(t) \tag{4.12}$$

$$= e^{-(\lambda_{\mathrm{ads}}+\lambda_{\mathrm{dec}}+\lambda_{\mathrm{TMP}})\cdot t} + \lambda_{\mathrm{des}} \cdot \int_0^t n_{\mathrm{Baffle}}\left(t'\right) \cdot e^{-(\lambda_{\mathrm{ads}}+\lambda_{\mathrm{dec}}+\lambda_{\mathrm{TMP}})\cdot(t-t')} dt' \tag{4.13}$$

Again, (4.13) contains an unknown: The fraction of radon atoms residing on the baffle. It can be described by a differential equation:

$$\frac{\mathrm{d}n_{\mathrm{Baffle}}(t)}{\mathrm{d}t} = \lambda_{\mathrm{ads}} \cdot n_{\mathrm{MS}}(t) - (\lambda_{\mathrm{des}} + \lambda_{\mathrm{dec}}) \cdot n_{\mathrm{Baffle}}(t)\,. \tag{4.14}$$

where $n_{\mathrm{Baffle}}(t')$ is the fraction of radon atoms residing on the baffle at a given time t'. The first term is the fraction of particles which have been adsorbed on the surface of the baffle which increases the fraction of radon atoms on the baffle. The second term is the fraction of radon atoms leaving the surface of the baffle either by decaying (λ_{dec}) or by desorption (λ_{des}) back into the main spectrometer. By inserting (4.13) into (4.14) a solvable equation is obtained.

$$\frac{\mathrm{d}n_{\mathrm{Baffle}}(t)}{\mathrm{d}t} = \lambda_{\mathrm{ads}} \cdot \left(e^{-(\lambda_{\mathrm{ads}}+\lambda_{\mathrm{dec}}+\lambda_{\mathrm{TMP}})\cdot t} + \lambda_{\mathrm{des}} \cdot \int_0^t n_{\mathrm{Baffle}}\left(t'\right) \cdot e^{-(\lambda_{\mathrm{ads}}+\lambda_{\mathrm{dec}}+\lambda_{\mathrm{TMP}})\cdot(t-t')} dt' \right) - (\lambda_{\mathrm{des}} + \lambda_{\mathrm{dec}}) \cdot n_{\mathrm{Baffle}}(t) \tag{4.15}$$

The differential equation was solved numerically with a classical fourth order Runge-Kutta method [SM03, p 328]:

$$n_{\mathrm{Baffle},m+1} = n_{\mathrm{Baffle},m} + \frac{t_s}{6} \cdot (k_1 + 2 \cdot k_2 + 2 \cdot k_3 + k_4) \tag{4.16}$$

$$k_1 = f(t_m, n_{\mathrm{Baffle},m}) \tag{4.17}$$

$$k_2 = f(t_m + 0.5 \cdot t_s, n_{\mathrm{Baffle},m} + 0.5 \cdot t_s \cdot k_1) \tag{4.18}$$

$$k_3 = f(t_m + 0.5 \cdot t_s, n_{\mathrm{Baffle},m} + 0.5 \cdot t_s \cdot k_2) \tag{4.19}$$

$$k_4 = f(t_m + t_s, n_{\mathrm{Baffle},m} + t_s \cdot k_3) \tag{4.20}$$

where $n_{\mathrm{Baffle},m}$ is the numerical solution for the step m and t_s is the step-size. The integrals are solved by the rectangle method:

$$\int_0^t f\left(t'\right) \mathrm{d}t' = \sum_{i=0}^{m} f(t_s) \cdot \frac{t_s}{2} \tag{4.21}$$

where $f(t)$ is the integrand and $m = {}^{t}/_{0.5 \cdot t_s}$ is the number of rectangles used for the integration. Furthermore the efficiency determination (4.9) is valid for infinitely large times. The upper limit of the simulation time was chosen as $t_{\mathrm{u}} = 1000\,\mathrm{s}$ resulting in:

$$\epsilon_{\mathrm{NM}} = \epsilon(1000\,\mathrm{s}) = 1 - n_{\mathrm{dec,MS}} \tag{4.22}$$

The resulting error can be estimated for $^{219}\mathrm{Rn}$ and $^{220}\mathrm{Rn}$ by calculating the fraction of radon atoms which have not decayed in $1000\,\mathrm{s}$:

$$\sigma = \exp\left(-\frac{1000\,\mathrm{s}}{\tau_{\mathrm{dec}}}\right) \approx \begin{cases} 4 \cdot 10^{-6}, & \text{for } ^{220}\mathrm{Rn} \\ 1 \cdot 10^{-76}, & \text{for } ^{219}\mathrm{Rn} \end{cases} \tag{4.23}$$

These errors are negligible.

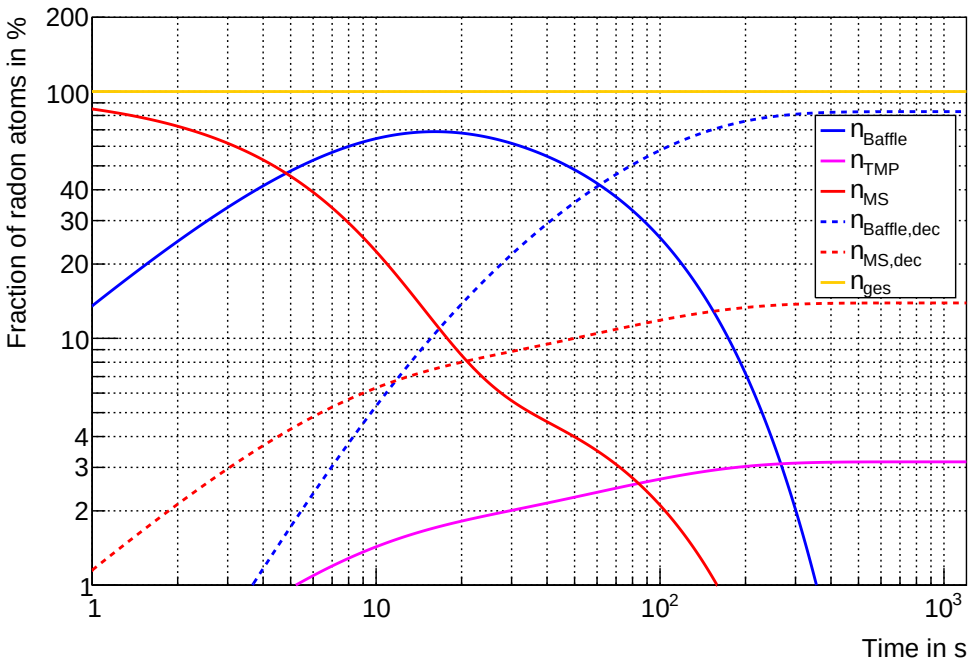

Figure 4.3: **The temporal development of $^{220}\mathrm{Rn}$ for a desorption time of $\tau_{\mathrm{des}} = \tau_{\mathrm{dec}} \approx 80.2\,\mathrm{s}$ and three cold baffles.** The total fraction of radon atoms is $100\,\%$ during the simulation (yellow). The fraction of radon atoms residing in the main spectrometer n_{MS} (red line) and the corresponding decays $n_{\mathrm{MS,\,dec}}$ (red dashed line) are shown. In addition the fraction of radon atoms residing on the baffle n_{B} (blue line) and the fraction of radon atoms decaying on it $n_{\mathrm{B,\,dec}}$ (blue dashed line) are shown. Lastly, the fraction of radon atoms, which are pumped by the TMPs are shown (magenta).

More importantly, the accuracy of this model is restricted by its simplicity. It does neither include the specific geometry of the baffles nor the remaining pump port volume behind them. This is of critical importance for radon emanating from the getter since it has to pass the baffle geometry. Thus, this model is restricted to radon emanating from the main spectrometer vessel. Furthermore, the influence of the geometry introduces a systematic error in this simulation as radon is more likely to hit the baffle again, when it re-desorbs from it. This influence is not taken into account in this model. In the following, the errors of the simulated suppression efficiency and the corresponding desorption time are assumed to be $4\,\%$ since the model fails to describe the specific KATRIN geometry and the baffle geometry in particular.

Resulting radon distribution and efficiencies

With this approach the influence of the desorption time on the radon distribution can be simulated. The set of parameters already used in the Simplified Model (see table 4.1) is needed as input in this model, too. As a further starting condition the radon atoms were assumed as equally distributed in the main spectrometer.

The direct output of one simulation consists of the fraction of radon atoms residing in the five states of the model (see figure 4.2) at each time step. The temporal development of the fraction of radon atoms in each state is shown exemplary for $^{220}\mathrm{Rn}$ and a desorption time of $\tau_{\mathrm{des}} = \tau_{\mathrm{dec,220}} = 80.2\,\mathrm{s}$ in figure 4.3. All radon atoms start in the main spectrometer. Due to the high pumping speed of the baffle, close to $70\,\%$ of the radon atoms get adsorbed on it while only smaller fractions decay or are pumped by the TMPs. After roughly $30\,\mathrm{s}$ The maximal fraction of radon atoms is on the baffle. Afterwards the desorption of radon atoms from the baffle replenishes the fraction of radon atoms in the main spectrometer which is indicated by the kink in its temporal development. This

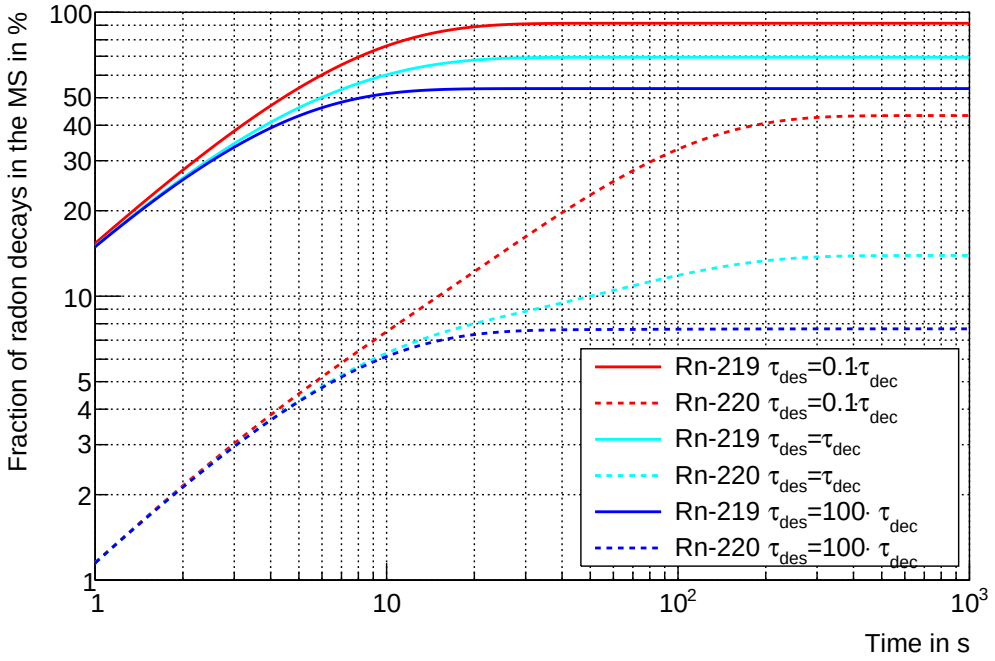

Figure 4.4: **The temporal evolution of the fraction of radon atoms decaying in the main spectrometer.** It is depicted for both $^{219}\mathrm{Rn}$ (solid lines) and $^{220}\mathrm{Rn}$ (dashed lines). The desorption time τ_{des} is changed for each of the three scenarios shown: $\tau_{\mathrm{des}} = 0.1 \cdot \tau_{\mathrm{dec}}$ (red), $\tau_{\mathrm{des}} = 1 \cdot \tau_{\mathrm{dec}}$ (cyan) and $\tau_{\mathrm{des}} = 10 \cdot \tau_{\mathrm{dec}}$ (blue). The influence of the desorption becomes apparent by comparing the three scenarios depicted.

kink also translates to the fraction of radon atoms pumped by the TMPs and the fraction which decays in the main spectrometer. Both show the same kink as they depend on the fraction of radon atoms in the main spectrometer. The distribution in the three final states of the model (the TMP or decay either in the main spectrometer or on the baffle) can be obtained by utilising the values at $1 \cdot 10^3\,\mathrm{s}$. Of all radon atoms $83\,\%$ decay on the baffle while $14\,\%$ decay in the main spectrometer and $3\,\%$ are pumped by the TMPs.

By varying the desorption time it is possible to obtain a better understanding of its influence. The most important region is defined by desorption times on the order of the lifetime of the radon isotopes as the competition between desorption and decay is the most pronounced. Exemplarily the desorption time is set to $\tau_{\mathrm{des}} = 0.1 \cdot \tau_{\mathrm{dec}}$, $\tau_{\mathrm{des}} = 1 \cdot \tau_{\mathrm{dec}}$ and $\tau_{\mathrm{des}} = 100 \cdot \tau_{\mathrm{dec}}$ (figure 4.4). The results show that a long desorption time cuts off growth of the fraction of radon atoms which decayed in the main spectrometer at the time where the maximum fraction residing on the baffle is observed ($15\,\mathrm{s}$). For a desorption time on the order of the lifetime of the radon isotope a kink is observed both for $^{220}\mathrm{Rn}$ and $^{219}\mathrm{Rn}$. For short desorption times the fraction of radon atoms decaying in the main spectrometer increases to the point where the kink is not resolved any more.

A high suppression efficiency as defined in (4.22) is most important for the sensitivity of the KATRIN experiment. The desorption time has been varied over the whole range where it is expected to have a significant effect on the background rate of the KATRIN experiment. Furthermore the number of baffles has been varied from 0 to 3. Simulations of $^{219}\mathrm{Rn}$ (figure 4.5) show the major impact of the desorption time on the efficiency of the suppression of radon α-decays in the main spectrometer. As expected, the increasing desorption times enhance the suppression efficiency as the fraction of radon atoms bound on the baffle increases. All simulations converge to the value of the scenario with warm baffles for low desorption times. The reason is that the fraction of radon atoms decaying on the baffle is small due to the negligible time the radon atoms spend on the baffle. The efficiency of suppression reaches its upper limit at desorption times of about $70\,\mathrm{s}$ implying

that any lower desorption time lowers the efficiency of suppression correspondingly.

It is advantageous to parametrize the results with an analytic function describing the simulations to be able to calculate the suppression efficiency reliably without the need of a complex computer algorithm. One possible ansatz is a logistic function. The reasoning is that logistic functions describe the growth of a population which starts out exponentially and saturates at a given level. The exponential growth in the beginning seems possible since all processes (desorption, decay and pumping) are described by exponentials.

$$\epsilon_l\left(\tau_{\mathrm{des}}\right) = \frac{L}{1+\exp\left(-k\cdot\left(\tau_{\mathrm{des}}-\tau_{\mathrm{des},0}\right)\right)} + c \tag{4.24}$$

$$= \frac{p0}{1+\exp\left(-p1\cdot\left(\tau_{\mathrm{des}}+p2\right)\right)} \tag{4.25}$$

An promising alternative is an arctangent since geometric dependencies often contain such functions.

$$\epsilon_a\left(\tau_{\mathrm{des}}\right) = p0\cdot\arctan\left(p1\cdot\tau_{\mathrm{des}}+p2\right)+p3 \tag{4.26}$$

The results of the fits to the simulation are included in figure 4.5. The arctangent fits are in good agreement with the data. As for this simulation the two radon isotopes differ only by their lifetimes. The increased lifetime of $^{220}\mathrm{Rn}$ translates to a shift of the shoulder of $\epsilon\left(\tau_{\mathrm{des}}\right)$ to higher desorption times while the shape of the function remains similar.

A logistic fit to the simulations of $^{219}\mathrm{Rn}$ shows worse agreement with the simulated points by several percent (see figure 4.6). It does not describe the data observed so well which is reflected by the big χ^2-values. The areas in which the logistic fit deviates are close to the extrema of the concavity. In fact, the fit quality of the logistic fits remains consistently worse than the arctangent fit. Therefore, it will not be discussed further.

In summary, the shape of the dependency of the suppression efficiency on the desorption time is described well by an arctangent function as shown in (4.26). The efficiency of suppression reaches its limit at desorption times of about $500\,\mathrm{s}$ implying that any lower desorption time increases the fraction of radon atoms emanating from the vessel which decay in the main spectrometer.

4.3 Test-particle Monte-Carlo simulation to track particles in vacuum

In order to determine the radon suppression efficiency a Monte Carlo simulation was performed. The freely available MOLFLOW+ code [CER15] was chosen and modified by Marcel Krause [Kra15] to enable the simulation of radioactive decays and re-desorption. Based on this modified MOLFLOW version simulations with a simplified geometry of the KATRIN main spectrometer were executed. This is the basis for the evaluation done here. In contrast to the two previous models, this approach allows to simulate radon emanating from the NEG material of the getter and takes into account the geometry of the baffles.

MOLFLOW+

MOLFLOW+ is a test-particle Monte-Carlo code designed for vacuum simulations in the ultra high vacuum regime [KP09]. This assumes that the mean free path of simulated particles in vacuum is larger than the geometry boundaries of the vessel. This is called free **mol**ecular **flow**. Therefore, particles move on straight trajectories until they hit a wall, where they are either adsorbed or diffusely reflected according to Lambert's cosine law:

$$P(\mathrm{d}\Omega) = \cos\theta\frac{\mathrm{d}\Omega}{\pi} \tag{4.27}$$

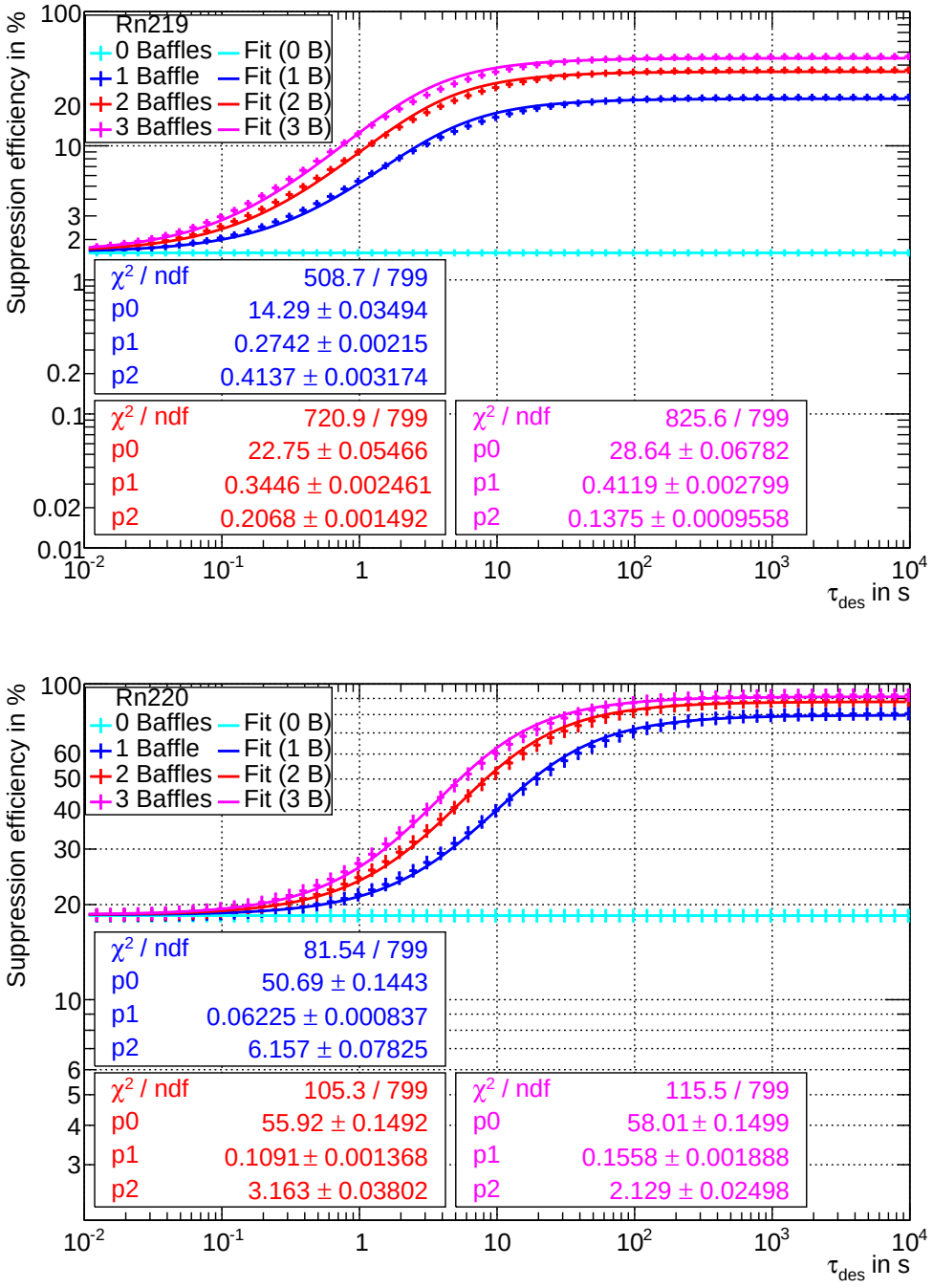

Figure 4.5: **The dependence of the suppression efficiency of $^{219}\mathrm{Rn}$ and $^{220}\mathrm{Rn}$ on the desorption time.** The fraction of radon atoms which emanated from the main-spectrometer vessel and decay in it are shown for desorption times between $0.02\,\mathrm{s}$ and $10^4\,\mathrm{s}$. Only every tenth simulated point is shown in the plots to increase the visibility of the fitted arctangent functions. The number of baffles is set to 0 (cyan), 1 (blue), 2 (red) and 3 (magenta). The corresponding fit parameters can be found in the statistic box with the same colour as the fit. **top:** The results for $^{219}\mathrm{Rn}$ are shown. **bottom:** The results for $^{220}\mathrm{Rn}$ are shown. The fitted arctangent functions describe the simulations well.

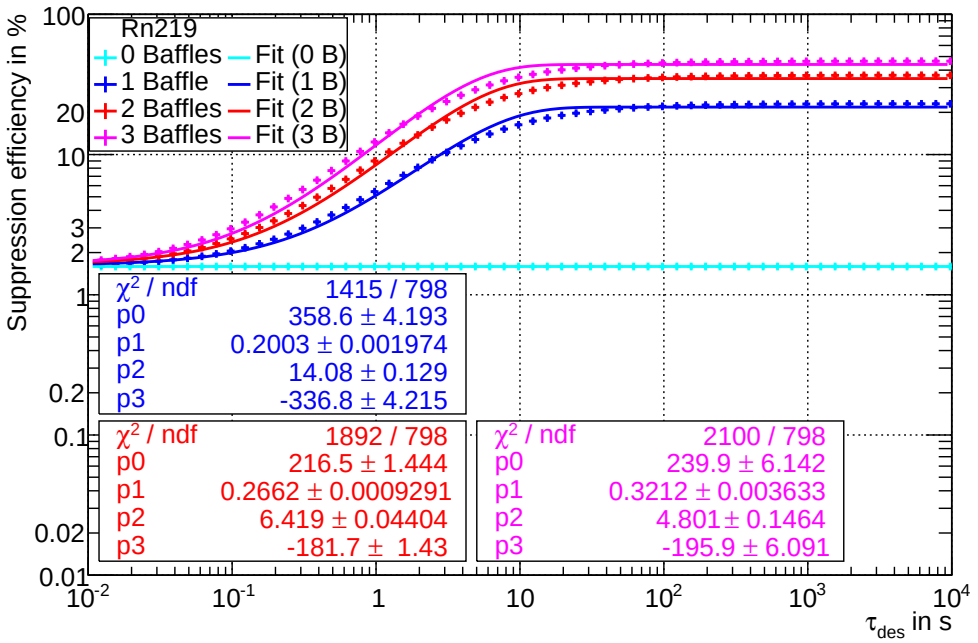

Figure 4.6: **The dependence of suppression efficiency of $^{219}\mathrm{Rn}$ on the desorption time is shown with a logistic fit.** The approach is the same as in figure 4.5. However, logistic functions (see (4.24)) are fitted to the simulations.

with $\Omega = (\theta, \phi)$ the solid angle, and $\mathrm{d}\Omega = \sin\theta \mathrm{d}\theta \mathrm{d}\phi$, where θ and ϕ are the usual angles of the spherical coordinate system. By transforming uniformly distributed random numbers x and y in the unit interval, θ and ϕ are generated according to

$$\theta = \arccos\left(\sqrt{1-x}\right) \tag{4.28}$$

$$\phi = 2 \cdot \pi \cdot y \tag{4.29}$$

The angle with which the particles desorb from the surface on which they were created is calculated in the same way.

MOLFLOW+ modifications

Marcel Krause modified MOLFLOW+ in order to allow simulations of short-lived radioactive particles. An additional parameter was added: each particle gets a finite lifetime when it is created. The lifetime T is created by generating a uniformly distribute random number f in the interval $[0, 1)$. The lifetime T of a specific particle is defined by the cumulative distribution function

$$f(T) = 1 - e^{-\frac{T}{\tau_{\mathrm{dec}}}} \tag{4.30}$$

where τ_{dec} is the mean lifetime of the isotope simulated.

In addition, a new property, the mean residence time, was added to the list of properties of each surface element of the geometric model. After an adsorption the particle can now desorb again. This process is the core of the radon interaction with the baffle. In order to describe this process a desorption time t_{des} is generated from a randomly distributed number g in the interval $[0, 1)$

$$g(t_{\mathrm{des}}) = 1 - e^{-\frac{t_{\mathrm{des}}}{\tau_{\mathrm{des}}}} \tag{4.31}$$

where τ_{des} is the mean residence time.

All in all, the simulation tracks one radioactive atom by first creating it with a lifetime T. During its motion the time since its creation t is tracked. When it hits an adsorbing wall the time until the re-desorption t_{des} is subtracted from the remaining lifetime $T - t$ of the particle. When the lifetime reaches 0 it decays. Depending on its decay position it either decays in the volume or on a surface. For volume decays the 3D coordinates of the decay positions are stored in an extra file. All other events along a trajectory of a particle are attributed to the surface element where the event occurred. Possible events are hits (reflection), adsorption (permanent adsorption or decay on a surface), desorption (start of a new particle) and re-desorption (after a preceding adsorption). Each surface element has four counters to count these events. The decay positions in the volume are evaluated to obtain the number of radon atoms which decayed in the pump ports N_{P} and in the vessel N_{V}. As a border between these volumes the side of the baffle facing the vessel was chosen.

In order to determine the fraction of radon atoms decaying in the main spectrometer, two effects have to be multiplied. The first factor is the fraction of radon atoms decaying in the vacuum:

$$f_1 = \frac{N_{\mathrm{DV}}}{N_{\mathrm{C}}} \tag{4.32}$$

where N_{DV} is the number of particles which decayed in the vacuum, while N_{C} is the number of particles created. The second factor is the fraction of radon atoms which decay in the main spectrometer volume and not in the pump ports

$$f_2 = \frac{N_{\mathrm{DT}}}{N_{\mathrm{ADV}}} \tag{4.33}$$

where N_{DT} is the number of radon decays in the tank volume (excluding the pump ports) and N_{ADV} is the number of radon decays in the vacuum. All in all, this leads to a suppression efficiency ϵ_{MF}

$$\epsilon_{\mathrm{MF}} = f_1 \cdot f_2 = 1 - \frac{N_{\mathrm{DV}}}{N_{\mathrm{C}}} \cdot \frac{N_{\mathrm{DT}}}{N_{\mathrm{ADV}}}. \tag{4.34}$$

N_{DV} and N_{DT} both are assumed to be binomially distributed leading to a statistical error of

$$\sigma_{N_{\mathrm{DV}}} = \sqrt{N_{\mathrm{DV}} \cdot f_1 \cdot (1 - f_1)} \tag{4.35}$$

$$\sigma_{N_{\mathrm{DT}}} = \sqrt{N_{\mathrm{DT}} \cdot f_2 \cdot (1 - f_2)} \tag{4.36}$$

As the baffle temperature has both an influence on the fraction of radon atoms decaying in the pump ports or in the vessel and on the fraction of radon atoms adsorbed on the baffle when they decay the correlation between the numbers N_{DV} and N_{C} does not vanish. The statistical error is:

$$\sigma_{\epsilon_{\mathrm{MF,stat}}} = \epsilon_{\mathrm{MF}} \cdot \sqrt{\left(\frac{\sigma_{N_{\mathrm{DV}}}}{N_{\mathrm{DV}}}\right)^2 + \left(\frac{\sigma_{N_{\mathrm{DT}}}}{N_{\mathrm{DT}}}\right)^2 + \left(2 \cdot \mathrm{COV}\left(N_{\mathrm{DV}}, N_{\mathrm{DT}}\right)\right)^2} \tag{4.37}$$

where $\mathrm{COV}\left(N_{\mathrm{DV}}, N_{\mathrm{DT}}\right)$ is the covariance. It can be simplified with the Cauchy-Schwarz inequality:

$$\sigma_{\epsilon_{\mathrm{MF,stat}}} \leq \epsilon_{\mathrm{MF}} \cdot \sqrt{\left(\frac{\sigma_{N_{\mathrm{DV}}}}{N_{\mathrm{DV}}}\right)^2 + \left(\frac{\sigma_{N_{\mathrm{DT}}}}{N_{\mathrm{DT}}}\right)^2 + \left(\frac{2 \cdot \sigma_{N_{\mathrm{DV}}} \cdot \sigma_{N_{\mathrm{DT}}}}{N_{\mathrm{DV}} \cdot N_{\mathrm{DT}}}\right)} \tag{4.38}$$

The upper limit of this inequality will be used from here on.

Setup of the main spectrometer

In order to describe the KATRIN main spectrometer geometry, a Simplified Model was created with Blender [SV15]. The main spectrometer with its pump ports and other ports, the baffle, NEG strips and the TMPs were incorporated. The inner wire electrodes are not included in the model

[Kra15]. Unfortunately, a mistake was made during the setup of the simulations. The radius of the transition between steep cones and flat cones of the source side of the main spectrometer was set to $r_{\mathrm{wrong}} = 3\,\mathrm{m}$ instead of $r_{\mathrm{right}} = 2.75\,\mathrm{m}$. Therefore the volume of the steep cone V_{sc} and the flat cone V_{fc} are slightly off.

$$V_{\mathrm{sc}} = \frac{h_{\mathrm{sc}} \cdot \pi}{3} \cdot \left(R_{\mathrm{sc}}^2 + R_{\mathrm{sc}} \cdot r + r^2\right) \tag{4.39}$$

$$V_{\mathrm{fc}} = \frac{h_{\mathrm{fc}} \cdot \pi}{3} \cdot \left(R_{\mathrm{fc}}^2 + R_{\mathrm{fc}} \cdot r + r^2\right) \tag{4.40}$$

where $h_{\mathrm{sc}} = 1.89\,\mathrm{m}$ is the length of the steep cone and $h_{\mathrm{fc}} = 5.25\,\mathrm{m}$ the length of the flat cone, $R_{\mathrm{sc}} = 0.25\,\mathrm{m}$ being the other radius of the steep cone and $R_{\mathrm{fc}} = 4.9\,\mathrm{m}$ is the other radius of the flat cone. Therefore, the combined volume is:

$$V_{\mathrm{cone}} = V_{\mathrm{sc}} + V_{\mathrm{fc}} = \begin{cases} 264.1\,\mathrm{m}^3, & \text{for } r_{\mathrm{right}} = 2.75\,\mathrm{m} \\ 281.7\,\mathrm{m}^3, & \text{for } r_{\mathrm{wrong}} = 3\,\mathrm{m} \end{cases} \tag{4.41}$$

The difference of these two values with respect to the whole volume of $V_{\mathrm{ges}} = 1240\,\mathrm{m}^3$ is $1\,\%$. This is expected to reduce the simulated effective pumping speed from the main spectrometer due to the increased volume. As a systematic error $\epsilon_{\mathrm{MF,syst}} = 2\,\%$ is assumed both on the suppression efficiency and the desorption time due to the inaccuracy of the model. It is combined with the statistical error as follows:

$$\sigma_{\epsilon_{\mathrm{MF,ges}}} = \sqrt{\epsilon_{\mathrm{MF,stat}}^2 + \epsilon_{\mathrm{MF,syst}}^2} \tag{4.42}$$

Resulting efficiency trends

The MOLFLOW+ model needs the actual geometry of the main spectrometer and its components as input as well as a mean desorption time of radon residing on the baffle. Furthermore, the lifetimes of the two radon isotopes are required, too. The pumping speed of a TMP or a baffle is described by a sticking coefficient α, which is the probability to that a particle, hitting this surface once, sticks to the surface. For TMPs α resembles the pumping probability for a particle flying through an orifice with the same diameter as the pump. For baffle surfaces α has been set to $\alpha_{\mathrm{B}} = 1$

At first, the whole main spectrometer is used as a source for radon emanation. Again, the number of baffles is varied from 0 to 3 and the desorption time of all three baffles is varied. The range is smaller since the simulations are much more time consuming. Again, an arctangent function as introduced in (4.26) is fitted to the data (see figure 4.7).

Extrapolating with this function is not recommended since the χ^2-values are not good. The suppression efficiency of $^{219}\mathrm{Rn}$ emanating from the wall is not good. At most a reduction of about $51\,\%$ is expected with three cold baffles.

In the case of $^{220}\mathrm{Rn}$ at most suppression efficiencies of about $93\,\%$ are expected in the case of three cold baffles. This implies that 7 times more $^{220}\mathrm{Rn}$ background emanating from the wall can be suppressed by the liquid-nitrogen cooled baffles.

Next, the NEG strips are considered as a source of $^{219}\mathrm{Rn}$. Currently there are only NEG strips installed into the pump ports 2 and 3. The simulations are depicted in figure 4.8. Here not only the number of cold baffles is important but also which baffles are cold, since only pump port 2 and 3 are equipped with NEG strips. Up to now the following configurations have been simulated: all baffles warm, baffle 3 cold, baffle 1 and 2 cold, baffle 2 and 3 cold and all cold baffles. The setting with warm baffles yields a reduction of $18\,\%$ due to the TMPs. The setting with baffle 3 cold results in a maximal reduction of about $68\,\%$ for large desorption times. In this case, baffle

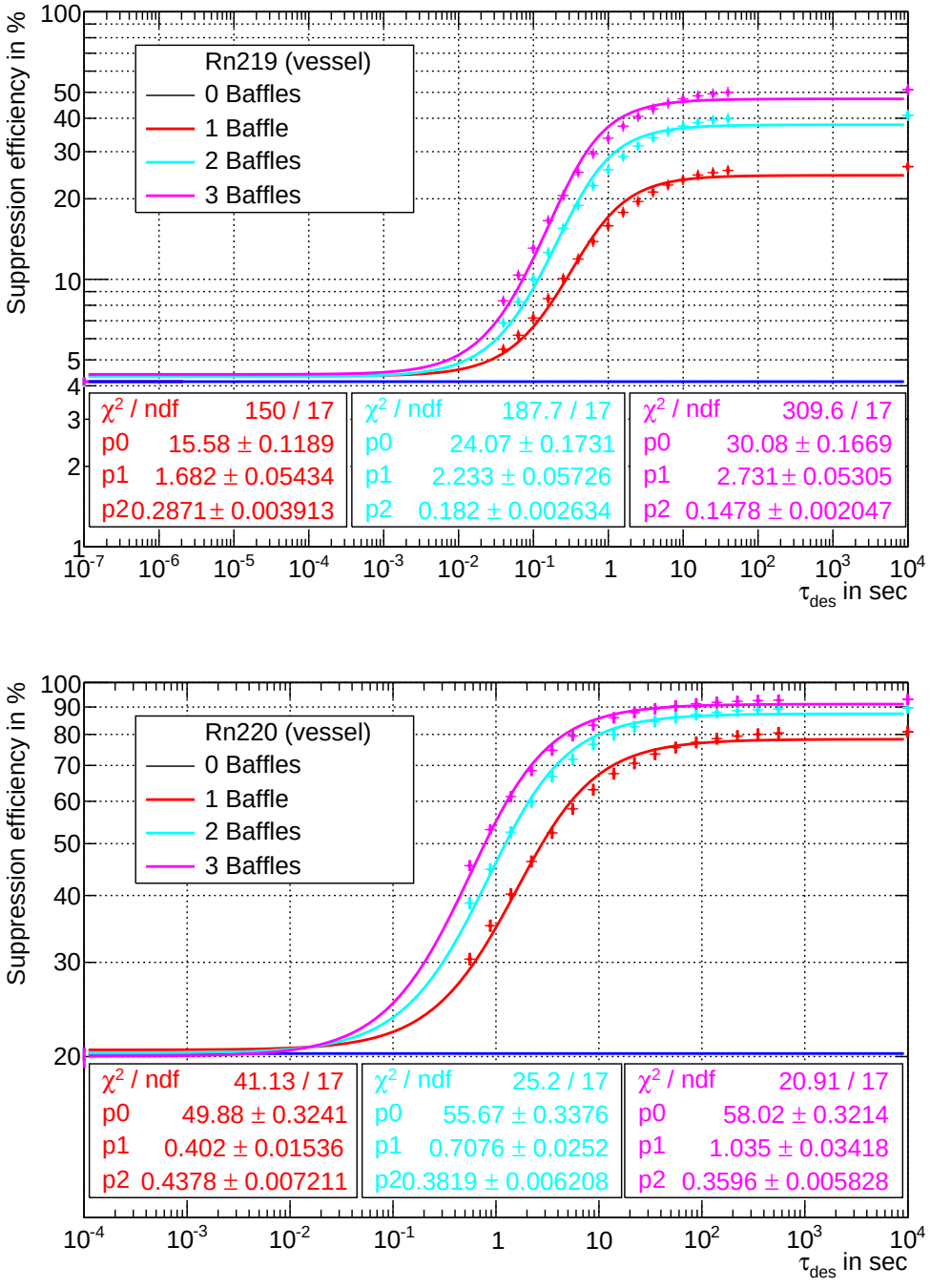

Figure 4.7: **The scenarios of either ^{219}Rn or ^{220}Rn emanating from the vessel are investigated.** The dependency of the suppression efficiency on the desorption time τ_{des} is shown. The data points simulated with MOLFLOW+ are shown. The number of baffles influences the suppression efficiency. Therefore, the scenario with 0 (blue), 1 (red), 2(cyan) and 3 (magenta) cold baffles is investigated. **top:** The simulations for ^{219}Rn are shown. In addition each data set is fitted with an arctangent function. **bottom:** The same is done for ^{220}Rn.

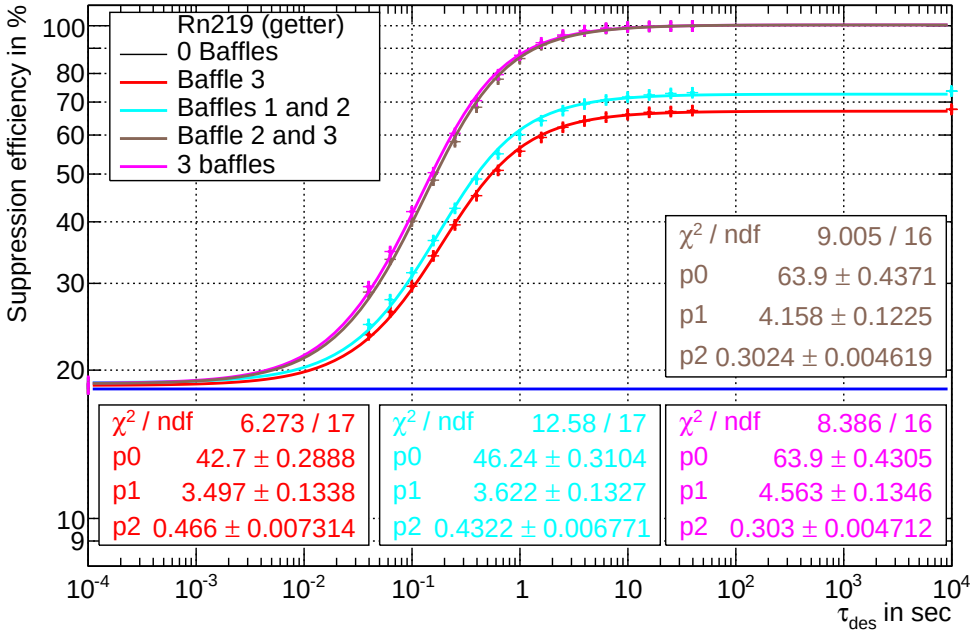

Figure 4.8: $^{219}\mathrm{Rn}$ **emanating from the getter is investigated.** The suppression efficiency of radon-induced backgrounds by the liquid-nitrogen cooled baffles is simulated for $^{219}\mathrm{Rn}$ emanating from the getter residing in the pump ports 2 and 3. Therefore, we expect different behaviours for cooling down either a baffle in these pump ports or the one in pump port 1. The combinations of cold baffles investigated are: 0 baffles cold (blue), baffle 3 cold (red), baffle 1 and 2 cold (cyan), baffle 2 and 3 cold (brown) and baffle 1,2, and 3 cold (magenta). Furthermore, an arctangent function was fitted to each simulation which describes the simulations well. The statistic boxes corresponding to the fits are coloured the same way as the fits.

3 blocks all the radon emanating from the NEG-strips in its pump port resulting in a reduction of $50\,\%$. It also pumps roughly $26\,\%$ (see figure 4.8) of the radon emanating from the NEG-strips in pump port 2. This leads to an additional reduction of $26\,\% \cdot 50\,\% = 13\,\%$. Since both baffle 2 and 3 have NEG-strips in their respective pump ports the same behaviour is expected if the baffle 2 is cooled instead of baffle 3. Baffle 1, however, is expected to show a different dependency. It is expected that it behaves more like the 1 baffle scenario for $^{219}\mathrm{Rn}$ emanating from the wall resulting in a value of about $28\,\%$. Therefore, the cool-down of baffle 1 is expected to be much less significant than the cool-down of baffle 2 or 3.

The cool-down of baffles 1 and 2 yields a reduction of $74\,\%$ for large desorption times. This represents an improvement of only $7\,\%$ when compared to the scenario where baffle 3 is cooled.

Cooling down baffle 2 and 3 yields a reduction of $100\,\%$ for large desorption times. The reason for the perfect suppression in the simulation scenario is the special geometry of the baffles. They block the direct line of sight between the main spectrometer volume and the NEG strips. Therefore each radon atom has to touch a baffle surface at least once and stays adsorbed for long times before reaching the main spectrometer. A more realistic scenario includes a chance that not all hits of radon on a baffle surface lead to adsorption. This factor can be included in an effective desorption time. Therefore, no additional simulations are required. However, it is important to keep in mind that reaching exactly $100\,\%$ is not realistic because of the deviation of the adsorption probability from $100\,\%$. As is expected due to the positioning of the NEG strips the scenario where baffle 2 and 3 are cooled differs significantly from the scenario where baffles 1 and 2 are cooled.

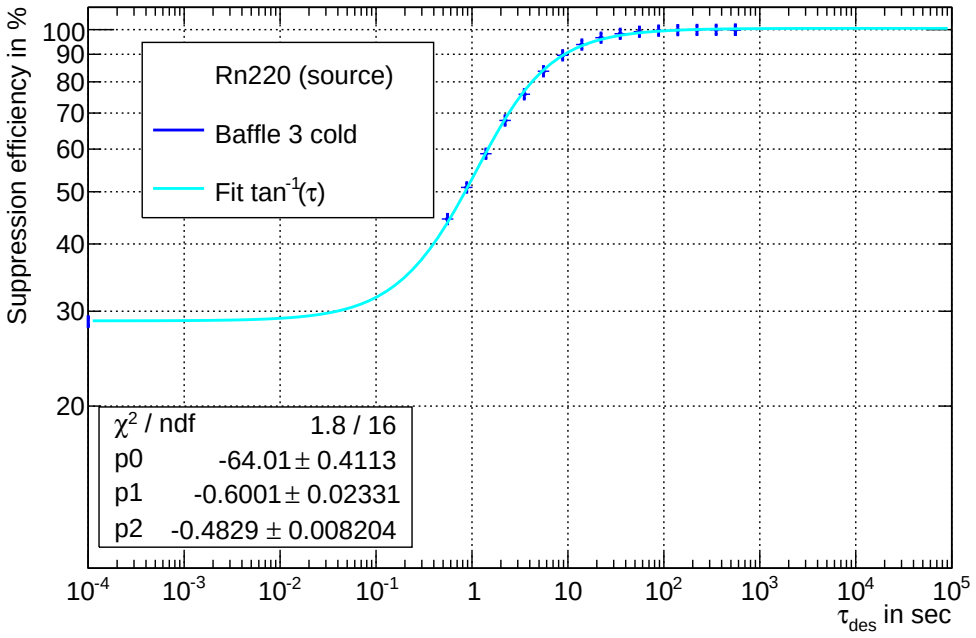

Figure 4.9: **The additional $^{220}\mathrm{Rn}$ source is investigated separately.** The source is attached to pump port 3 and the dependency of the suppression efficiency of radon decays in the main spectrometer volume is investigated. Only the temperature of baffle 3 is varied while the other baffles are warm. An arctangent is fitted to the data points.

The scenario of 3 cold baffles closely resembles the scenario with baffle 2 and 3 being cooled since the influence of baffle 1 is minor. Again an arctangent is fitted to the data. The arctangent describes the data well and can be used to extrapolate to lower values.

The final simulation describes an additional $^{220}\mathrm{Rn}$ source connected to pump port 3 (figure 4.9). The effect of the cool-down of baffle 3 is investigated. Again, for high desorption times the suppression efficiency is $100\,\%$. As before this result is not entirely realistic since the adsorption probability is not $100\,\%$ therefore reducing the suppression efficiency.

Again an arctangent function was fitted to the data points available. The limit for low desorption times is $28\,\%$ and is slightly higher than for $^{220}\mathrm{Rn}$ emanating from the vessel. The reason is the short distance to the TMPs and the baffle restricting the movement of the $^{220}\mathrm{Rn}$ atoms out into the main volume of the spectrometer.

4.4 Comparison of the different models

The parameters which have been obtained with the Simplified Model are the limits $\tau\mathrm{des} \to 0$ and $\tau\mathrm{des} \to \infty$ of both the Numerical Model and the MOLFLOW+ simulations. As the Simplified Model is a special case of the Numerical Model with the additional constraint of $\tau_{\mathrm{des}} = 0\,\mathrm{s}$, it is expected that both models provide the same results for the same set of parameters. These values are compiled in table 4.2 for emanation of radon from the wall of the main spectrometer. Furthermore, the measurements for $^{219}\mathrm{Rn}$ emanating from the getter and the measurements with an additional source are compiled in table 4.3.

As expected the Simplified Model and the Numerical Model do not differ. In addition the comparison of the limits of these two models with the MOLFLOW Simulations are in good agreement.

The numerical and the MOLFLOW Simulations both allow to investigate the dependency of the suppression efficiency on the desorption time for both radon isotopes (see figure 4.10). In addi-

Table 4.2: **Comparison of the different models for radon emanating from the walls.** The Simplified Model, the Numerical Model and MOLFLOW+ simulations all yield suppression efficiencies for the limits of the mean desorption time. The isotope, the limit of τ_{des} which is currently investigated, the suppression efficiency of the Simplified Model ϵ_{SM}, of the Numerical Model ϵ_{NM} and of the MOLFLOW Simulations ϵ_{MF} are given.

Rn isotope	Limit	Number of cold baffles	ϵ_{SM} in %	ϵ_{NM} in %	ϵ_{MF} in %
^{219}Rn (Wall)	$\tau_{\mathrm{des}} \to 0$	0	1.59 ± 0.06	1.60 ± 0.06	4 ± 2
^{219}Rn (Wall)	$\tau_{\mathrm{des}} \to \infty$	1	1.59 ± 0.06	1.60 ± 0.06	4 ± 2
		1	23.0 ± 0.9	23.0 ± 0.9	26 ± 1
		2	37 ± 1	37 ± 1	41 ± 1
		3	46 ± 2	46 ± 2	51 ± 1
^{220}Rn (Wall)	$\tau_{\mathrm{des}} \to 0$	0	18.5 ± 0.7	18.5 ± 0.7	20 ± 2
^{220}Rn (Wall)	$\tau_{\mathrm{des}} \to \infty$	0	18.5 ± 0.7	18.5 ± 0.7	20 ± 2
		1	81 ± 3	81 ± 3	80.9 ± 0.4
		2	89 ± 4	89 ± 4	89.7 ± 0.2
		3	92 ± 4	92 ± 4	93.0 ± 0.1

tion to the offset of the limits the numerical curve is shifted by one order of magnitude to lower desorption times when compared to the curve obtained with the MOLFLOW data. This effect is most likely caused by the baffle geometry. Only a fraction of radon atoms hitting the baffle is re-desorbed into the direction of the main spectrometer volume. For the most part the radon atoms, which desorb from the baffle, hit the baffle again at a different position. It is expected that the inclusion of this effect would results in a shift of the Numerical Model to values closer to the MOLFLOW Simulations.

Lastly, the models differ in computation time. The Simplified Model is a simple function and can be calculated within seconds. The Numerical Model requires a program to solve the differential equations and about $20\,\mathrm{s}$ to calculate the efficiency for one specific desorption time. As this model is implemented in C++ the number of data points calculated within one run can be increased arbitrarily thus minimising the manpower needed. The MOLFLOW model requires at least $10\,\mathrm{min}$ for short desorption times and up to several hours for long desorption times on the order of τ_{dec} in order to calculate the efficiency for one set of parameters. In addition each MOLFLOW Simulation has to be started manually making simulations rather slow. As a final possibility the arctangent fit to the MOLFLOW+ data can be used to calculate data points at an arbitrary desorption time within seconds. Despite the long simulation time, the MOLFLOW models are the most accurate description of the radon suppression in the main spectrometer. Therefore, they are used for the analysis of the measured data in section 6.

Table 4.3: **Comparison of the different models for radon emanating from the NEG or the additional $^{220}\mathrm{Rn}$ source .** The MOLFLOW+ simulations yield suppression efficiencies for the limits of the mean desorption time. The Simplified model assumes adsorbed particles to stay on the surface forever for $\tau_{\mathrm{des}} \to \infty$ which leads to a prediction of $\epsilon_{\mathrm{SM}} = 100\,\%$. The Numerical Model is not available for sources in a pump port. The "-" sign states that the corresponding model cannot be applied for the scenario.

Rn isotope	Limit	Cold baffles	ϵ_{SM} in %	ϵ_{NM} in %	ϵ_{MF} in %
$^{219}\mathrm{Rn}$ (NEG)	$\tau_{\mathrm{des}} \to 0$	all warm	-	-	18 ± 2
$^{219}\mathrm{Rn}$ (NEG)	$\tau_{\mathrm{des}} \to \infty$	3	-	-	67.7 ± 0.7
		1; 2	-	-	73.6 ± 0.5
		2; 3	100	-	99.91 ± 0.002
		1; 2; 3	100	-	99.92 ± 0.002
$^{220}\mathrm{Rn}$ (Source)	$\tau_{\mathrm{des}} \to 0$	all warm	0	-	29 ± 1
$^{220}\mathrm{Rn}$ (Source)	$\tau_{\mathrm{des}} \to \infty$	3	100	-	99.9975 ± 0.0008

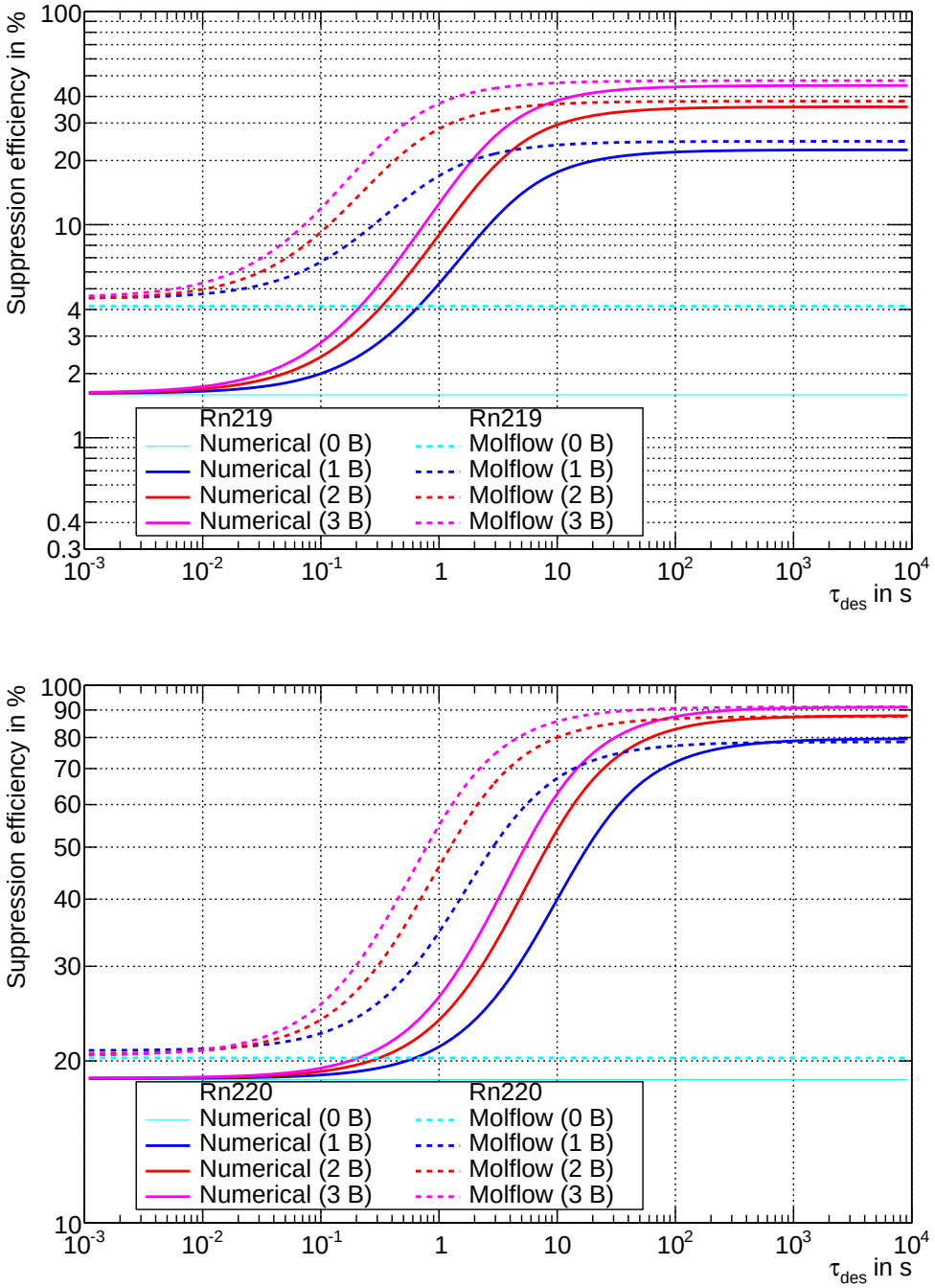

Figure 4.10: **Comparison of the numerical and the MOLFLOW Simulations.** The numerical simulations and the MOLFLOW Simulations are compared for the scenarios with radon emanating from the main spectrometer vessel. The number of baffles is varied from 0 to 3. For each of these scenarios the suppression efficiency is determined for varying τ_{des}. The results presented here are the arctangent fit to the data points. Please note that the MOLFLOW Simulations are missing data points to cover the whole range. The curves presented for the MOLFLOW Simulations are only extrapolations for values lower than $0.5\,\mathrm{s}$. In this area of low desorption times only the endpoints for $\tau_{\mathrm{des}} = 0$ have been verified. **top:** The simulations have been performed for $^{219}\mathrm{Rn}$. **bottom:** In addition, the simulations for $^{220}\mathrm{Rn}$ are depicted.

4.5 Conclusion

The important limits of the performance of the baffle system have been investigated by three different models, the Simplified Model, the Numerical Model and the MOLFLOW Simulations. Cryosorption of radon atoms on the cold baffle surfaces is not permanent. Radon can be desorbed after a mean residence time of τ_{des}, which depends strongly on the temperatures of the baffles. Therefore, the residence time is an important parameter for the understanding of the behaviour of the baffle performance. In the Numerical Model and the MOLFLOW Simulations τ_{des} is an integral part of the model, while for the Simplified Model τ_{des} is only taken into account indirectly through the pumping speed S_{Baffle}. The value of S_{Baffle} has been determined with a MOLFLOW simulation for different sticking coefficients $\alpha = 100\,\%$ which corresponds to $\tau_{\mathrm{des}} \to \infty$.

By considering residence times much larger than the lifetime of the respective radon isotope, it is found that $^{220}\mathrm{Rn}$ emanating from the vessel can be suppressed with an efficiency of up to $(93.0 \pm 0.1)\,\%$, while $^{219}\mathrm{Rn}$ emanating from the main spectrometer vessel can only be suppressed by $(51 \pm 1)\,\%$.

Furthermore, the MOLFLOW Simulations allow to study the suppression efficiency of $^{219}\mathrm{Rn}$ emanating from the two sets of NEG strips located in pump port 2 and 3. With only baffle 3 cold the simulation produces a maximal suppression efficiency of $(67.7 \pm 0.7)\,\%$, while the cooldown of the baffles 1 and 2 allows for a maximal suppression efficiency of $(73.6 \pm 0.6)\,\%$. When baffle 2 and 3 are cold a suppression efficiency of $100\,\%$ can be achieved. The same is valid when all three baffles are considered. As the dependency of the suppression efficiency of radon decays on τ_{des} is described by the models, it is possible to compare the simulated baffle efficiency for different τ_{des} with measured data in order to learn more about the desorption process. This will allow to predict the efficiency of radon suppression for different setups such as the final setup with three NEG pumps instead of two and three cold baffles.

All three simulations return similar results for radon emanating from the main spectrometer vessel. The values obtained are in good agreement.

An arctangent fit can parametrise the simulations well. This fit can be used to interpolate between measurement points, allowing to reduce the number of time consuming simulation points, thus saving computation time and the time spent to set up a MOLFLOW model.

Finally, it is strongly recommended to perform additional MOLFLOW Simulations increasing the range covered by the simulations down to $10^{-2}\,\mathrm{s}$ as the suppression efficiency changes significantly between the last simulated points and this value. Furthermore, two more simulations at $10^{-3}\,\mathrm{s}$ and $10^{3}\,\mathrm{s}$,respectively, would allow for more stable fits.

5. Measurements of the radon-induced background

In this chapter the radon-induced background originating from the main spectrometer and its suppression by liquid-nitrogen cooled copper baffles are investigated. Radon is a background source of critical importance since its contribution to the total background rate exceeds the design limit of $10^{-2}\,\mathrm{cps}$ [KAT05] [Mer13]. The importance of this background was shown by measurements at the pre-spectrometer [Fra10] [Goe12], simulations [Mer13] [Wan13] and further measurements at the main spectrometer during the initial commissioning phase of the spectrometer and detector section (SDS-I) [Goe14] [Sch14]. A major achievement of this phase was the experimental proof that the detected radon-induced background is significantly suppressed by liquid-nitrogen cooled copper baffles. Since the high-voltage separators of the liquid-nitrogen supply system were not available during the SDS-I commissioning phase it was only possible to operate the baffle system at low temperatures for a short time ($7\,\mathrm{h}$) while the retarding potential was applied to the main-spectrometer vessel.

For the second commissioning phase (SDS-II) these high-voltage separators were implemented (see section 3.5) in order to operate the baffles as required, even at high voltage. With this setup, it is possible to perform measurements at artificially elevated pressures in the main spectrometer which allows to efficiently search for radon-induced events in the data (section 5.1). The reduction of radon-induced background by different combinations of liquid-nitrogen cooled copper baffles is discussed in detail as well (section 5.2). The temporary installation of an additional radon source allows to study the influence of its contribution to the background (section 5.3) and the temperature dependence of the background reduction (section 5.4). The latter is compared with simulations of the radon background (section 5.5).

5.1 Identification of background originated by stored particles

The radon α-decay is accompanied by the emission of electrons by various processes (see section 3.2). These electrons can be stored in a MAC-E filter like the KATRIN main spectrometer (see section 3.1). A magnetically trapped electron can ionize residual-gas particles and create secondary electrons which may leave the spectrometer, hit the detector and produce background. In order to investigate the radon-induced background it is essential to separate it from other background sources. This can be achieved by searching for event clusters featuring characteristic ring-like patterns at the detector.

Measurements at artificially elevated pressures

The identification of stored particles is based on electrons resulting from ionisations of residual-gas atoms and molecules. For elevated pressures the electron scattering probability P scales proportionally to the number of targets [Wan13].

$$P = n \cdot \sigma \cdot s \tag{5.1}$$

where n is the number of targets per volume, σ is the scattering cross section and s is the electron path length. Based on these properties it is possible to calculate the mean free path λ.

$$\lambda = \frac{1}{n \cdot \sigma} \tag{5.2}$$

By utilizing the ideal-gas law the density of target atoms n can be calculated as a function of the pressure p.

$$p \cdot V = N \cdot R \cdot T \tag{5.3}$$

$$\Leftrightarrow n = \frac{N}{V} = \frac{p}{R \cdot T} \tag{5.4}$$

where V is the gas volume, N is the target number, R is the gas constant and T is the temperature. By assuming a non-relativistic scenario it is now possible to determine the mean time between two scattering events t_{scatter}.

$$E_{\mathrm{kin}} = \frac{1}{2} \cdot m_{\mathrm{e}} \cdot V^2 = \frac{1}{2} \cdot m_{\mathrm{e}} \cdot \left(\frac{\lambda}{t_{\mathrm{scatter}}} \right)^2 \tag{5.5}$$

$$t_{\mathrm{scatter}} = \sqrt{\frac{m_{\mathrm{e}} \cdot \lambda^2}{2 \cdot E_{\mathrm{kin}}}} \tag{5.6}$$

Using (5.2) and (5.4) this equation can be written as:

$$t_{\mathrm{scatter}} = \sqrt{\frac{m_{\mathrm{e}}}{2 \cdot E_{\mathrm{kin}}}} \cdot \frac{1}{\sigma_{\mathrm{tot}} \cdot n} = \sqrt{\frac{m_{\mathrm{e}}}{2 \cdot E_{\mathrm{kin}}}} \cdot \frac{R \cdot T}{\sigma_{\mathrm{tot}} \cdot p} \tag{5.7}$$

From (5.7) it is evident that the scattering time is anti-proportional to the pressure. This dependence is shown exemplarily in table 5.1. From the numbers obtained it can be seen that for increasing pressure the events created by one stored electron occur during shorter timescales. At $10^{-8}\,\mathrm{mbar}$ the mean time interval between two scattering events is $0.1\,\mathrm{s}$. This means that a deviation from the KATRIN standard operating pressure ($10^{-11}\,\mathrm{mbar}$) to elevated pressures ($10^{-8}\,\mathrm{mbar}$) enables the accumulation of events induced by stored particles on short time periods. This allows to separate the background produced by stored electrons from other backgrounds by searching for the occurrence of temporally localised spikes in the event rate. These event clusters can be clearly seen in the trend of the event rate from a typical background measurement at elevated pressure (see figure 5.1). In addition, it can be observed that the three operated copper baffles installed in the three pump ports of the main spectrometer significantly reduce the number of these clusters. This reduction is expected for radon as a source of stored electrons.

Ring search

One way to search for background originated by stored particles is to make use of their magnetron drift in a MAC-E filter (see section 3.1), resulting in detector hits with a ring-like structure (see figure 5.2). However, in order to ensure the validity of this detection method the cluster multiplicity needs to be at least as high as 10 [Sch14]. In order to avoid the loss of statistics a more sophisticated way to detect such clusters is required.

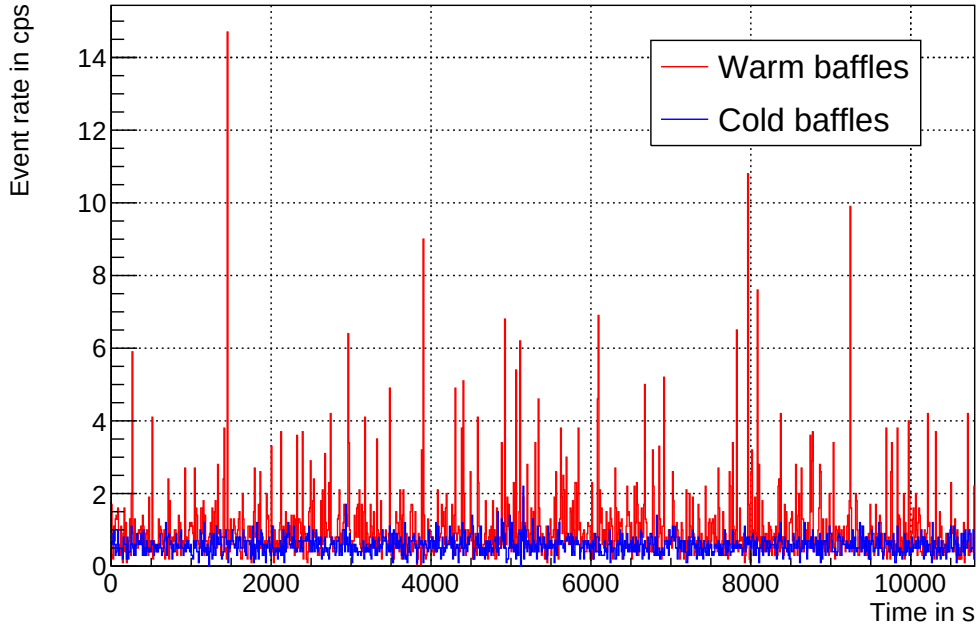

Figure 5.1: **Rate trend of measurements with a warm baffle and a cold baffle configuration.** The rate trend of a configuration with three warm baffles (red) is compared to a measurement with three cold baffles (blue). The clusters are visible as spikes in the event rate. The comparison of these measurements yields a strong decrease of clusters for cold baffles. This reduction is equivalent to a diminution of the processes creating the corresponding background events.

Time-interval threshold and multiplicity threshold

At elevated pressures the events originated from stored particles have lower inter-arrival times than from other background sources. This temporal correlation can be utilised to enrich the sample with background produced by stored particles. The distribution of inter-arrival times for a typical measurement is depicted in figure 5.3. It follows an exponential dependency for inter-arrival times with $\Delta t \geq 0.2\,\mathrm{s}$ as it is expected for uncorrelated events. At smaller time scales the exponential dependency becomes invalid due to the highly correlated background induced by stored electrons at elevated pressure.

Two successive events originated from other backgrounds have a considerable chance to pass the chosen time threshold. This is hinted by the extrapolation of the exponential function to lower inter-arrival times in figure 5.3. In order to suppress these false positives the number of consecutive events that have to occur within $\Delta t = 0.2\,\mathrm{s}$ of a next event have to be considered. This number is

Table 5.1: **Pressure dependence of the mean time interval between two scattering events.** The mean time interval between two scattering events is given for $m_\mathrm{e} \cdot c^2 = 511\,\mathrm{keV}$, $T = 19\,^\circ\mathrm{C}$ and $E_\mathrm{kin} = 10\,\mathrm{keV}$ with a corresponding total scattering cross section of $\sigma = 6.4 \cdot 10^{-18}\,\mathrm{cm}^2$ [Wan13].

Pressure in mbar	Scattering time in s
10^{-8}	0.11
10^{-9}	1.1
10^{-10}	11
10^{-11}	110

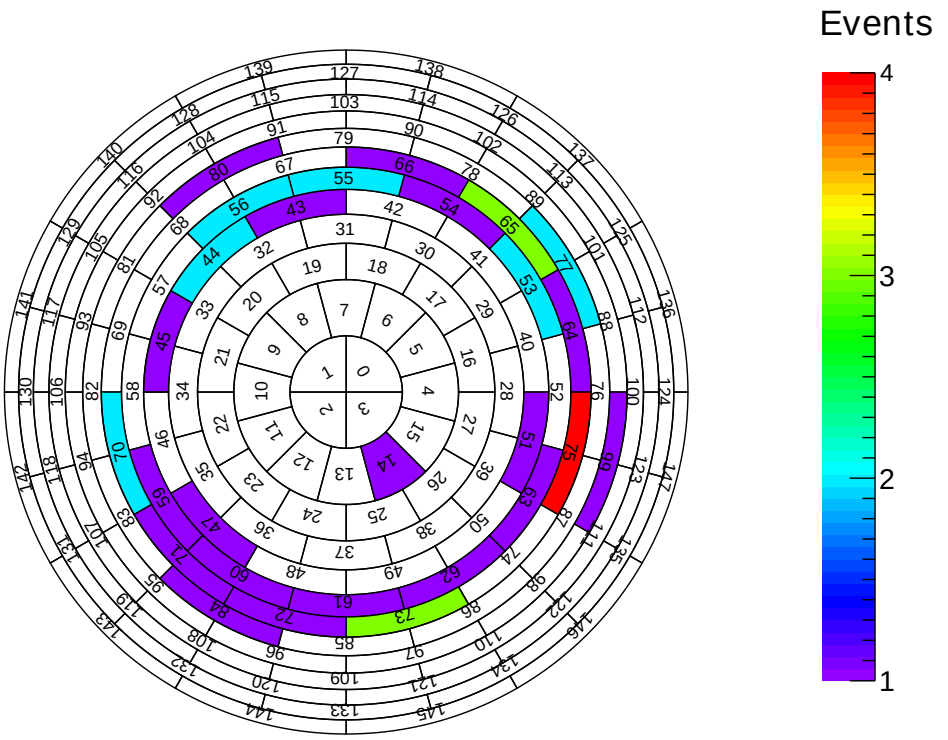

Figure 5.2: **Event cluster mapped on the corresponding pixels of the detector.** The number of detected events for each pixel within a typical rate spike is shown in the pixel map. The resulting ring structure is expected due to the storage conditions of MAC-E filters, in particular due to the magnetron drift of electrons.

called multiplicity N. In the scope of this work $N \geq 5$ is chosen as a boundary.

The last remaining problem is temporal overlapping of clusters. It becomes more probable both for an increasing number of clusters per time and for decreasing pressure. Due to the dependency on the cluster rate C_{Rn} the measurements with an additional radon source are prone to this effect. In order to investigate this behaviour the occurrence of the clusters is assumed to be Poisson-distributed in time. For such processes the probability O that two clusters arrive within a certain time-interval Δt_{d} of each other can be calculated [Sch14].

$$O = \frac{\int_0^{\Delta t_{\mathrm{d}}} e^{-C_{\mathrm{Rn}} \cdot t}\, dt}{\int_0^{\infty} e^{-C_{\mathrm{Rn}} \cdot t}\, dt} \tag{5.8}$$

$$= 1 - e^{-C_{\mathrm{Rn}} \cdot \Delta t_{\mathrm{d}}} \tag{5.9}$$

With a multiplicity of $N = 5$ and a time-interval threshold of $\Delta t = 0.2\,\mathrm{s}$ the mean cluster rate is $C_{\mathrm{Rn}} = 0.38\,\mathrm{s}^{-1}$ with warm baffles, but with the radon source and a mean cluster duration of $\Delta t_{\mathrm{d}} = 0.35\,\mathrm{s}$ (see figure 5.4), so that the probability of overlaps is $O = 12.5\,\%$. Additionally, an integration over all cluster durations yields that $34\,\%$ of the measurement time is covered by clusters. This will lead to an overestimation of events included in clusters.

In conclusion, an event cluster is characterised by a cut on the event inter-arrival time ($\Delta t \leq 0.2\,\mathrm{s}$) and a cut on the event multiplicity ($N \geq 5$). This characterisation allows to efficiently search for clusters in the background rate.

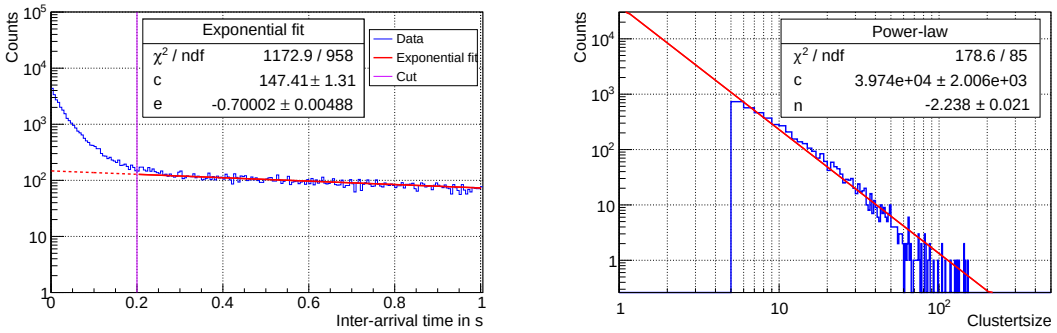

Figure 5.3: **Inter-arrival time and multiplicity.** On the **left-hand side** the inter-arrival times of successive events are presented (blue). An exponential fit $f(\Delta t) = c \cdot \exp(e \cdot \Delta t)$ is applied to the data from $0.2\,\mathrm{s}$ to $1\,\mathrm{s}$ (red exponential function) and extrapolated to lower time-intervals (red dashed exponential function). A suggested cut at $\Delta t = 0.2\,\mathrm{s}$ is added (magenta line). On the **right-hand side** the occurrence of the event multiplicity in the observed clusters can be seen. Bins with a multiplicity of $N \leq 5$ are not shown due to the not negligible possibility of contamination of the data with accidental contributions by other backgrounds. Furthermore, a power-law $f(N) = c \cdot N^n$ has been fitted to the event multiplicity.

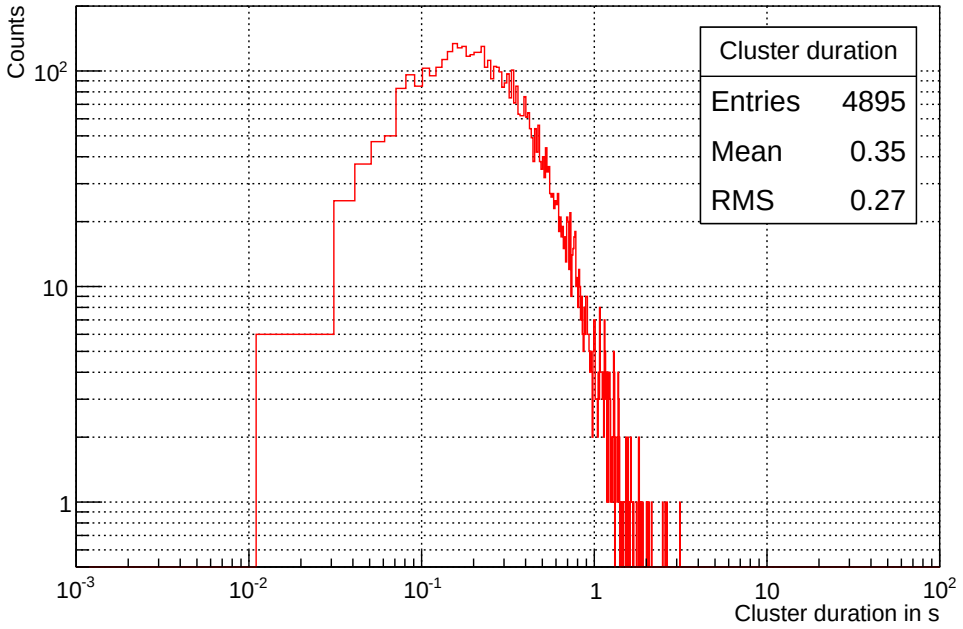

Figure 5.4: **Cluster duration for a measurement with a radon source behind the warmed-up baffle in pump port 3.** The corresponding measurements were taken with the pressure elevated to $1 \cdot 10^{-8}\,\mathrm{mbar}$ and a radon source with fully opened valve installed in the pump port 3 behind the warmed-up baffle. The mean duration of a cluster is $(0.35 \pm 0.27)\,\mathrm{s}$. As an error estimate the root mean square value is taken since this is a non-Gaussian-distributed value.

Measurement parameters

In order to gain insight into the behaviour of the background originated by radon different combinations of operating cold baffles were used with and without an artificial radon source installed. There were several measurement parameters remaining constant during all measurements: The voltage of the main-spectrometer vessel $U_{\text{Vessel}} = -18.5\,\text{kV}$, the voltage of the inner electrode (IE) $U_{\text{IE}} = -18.6\,\text{kV}$, the voltage of the post-acceleration electrode (PAE) $U_{\text{PAE}} = 10\,\text{kV}$, and the magnetic-field configuration represented by its value at the analysing plane $B = 5\,\text{G}$ are the most important settings. Only 142 of the 148 detector pixels are used for the following analyses. The excluded ones are pixels 10, 34, 58, 82, 106 and 130 due to a defect of the corresponding pre-amplifier card. The position of these pixels can be seen in figure 5.2. Only low-energetic negatively charged particles with energies E_{MS} on the order of $1\,\text{eV}$ in the analysing plane can escape the main spectrometer. On their way to the detector these particles gain energy due to the potential of the analysing plane U_{IE}, the post acceleration voltage U_{PAE} and the bias voltage $U_{\text{Bias}} = 0.12\,\text{kV}$ of the FPD detector. In total the energy of the electrons reaching the detector is

$$E_0 = E_{\text{MS}} + e \cdot (-U_{\text{IE}} + U_{\text{PAE}} + U_{\text{Bias}}) = 28.72\,\text{keV} \tag{5.10}$$

The FWHM[1] energy resolution of the FPD detector is $\Delta E \approx 2\,\text{keV}$ at E_0, thus, the energy region of interest is defined by $E_0 - 3\,\text{keV}$ to $E_0 + 2\,\text{keV}$. With E_0 from (5.10) the region of interest for electrons being low-energetic in the main spectrometer is $25.72\,\text{keV}$ to $30.72\,\text{keV}$. This parameter is valid for all runs used in this thesis.

The parameters used for the background measurements with different baffle configurations are summarised in table 5.2. The measurements with the artificial radon source are split into two sections: measurements with constant temperature settings can be found in table 5.3 while the measurements with temperature variations are summarised in table 5.4.

The baffle temperature was varied by controlling the liquid-nitrogen flow. In this context, there are several parameters which were utilised: the minimal and the maximal valve-opening positions v_{min} and v_{max} of the liquid-nitrogen supply line connected to baffle 3, the minimum temperature T_{min} and the maximal warm-up ΔT above T_{min}. In this range the valve was opened corresponding to:

$$v_{\text{current}} = \begin{cases} v_{\text{max}} & \text{if } T_{\text{current}} \geq T_{\text{min}} + \Delta T \\ v_{\text{min}} + \frac{T_{\text{current}} - T_{\text{min}}}{\Delta T} \cdot (v_{\text{min}} - v_{\text{max}}) & \text{if } T_{\text{min}} < T_{\text{current}} < T_{\text{min}} + \Delta T \\ v_{\text{min}} & \text{if } T_{\text{current}} \leq T_{\text{min}} \end{cases} \tag{5.11}$$

The values used during measurements 1 to 4 are summarised in table 5.5.

[1] **F**ull **W**idth at **H**alf **M**aximum

Table 5.2: **Measurement parameters during background measurements.** All measurements were performed with a pressure of $p \approx 10^{-8}\,\text{mbar}$ in the main spectrometer. The run numbers, the voltage of the steep cones (SC) U_{SC}, and the mean rate of events within the region of interest including statistical uncertainties are given for each combination of baffles cooled to liquid-nitrogen temperatures.

Runs	Cooled baffles	U_{SC} in V	Mean event rate in mcps
20972 to 20990	none	0	1064 ± 4
21113 to 21135	2	0	761 ± 3
24039 to 24082	1; 2	1	768 ± 2
20922 to 20965	2; 3	0	589 ± 2
22064 to 22125	1; 2; 3	1	587 ± 2

Table 5.3: **Parameters for measurements with an additional radon source.** The measurement parameters and run numbers used for the determination of the baffle efficiencies are listed. There are several parameters: the positioning of the radon source, the opening position of the valve separating the radon source from the main spectrometer and the voltage of the steep cones (SC) U_{SC}. In addition, the mean rate of events observed is given.

Runs	Cooled baffles	Positioning of radon source	Valve opening of radon source in %	U_{SC} in V	Mean event rate in mcps
22126 to 22129	1; 2; 3	Pump port 2	100	1	1185 ± 10
22142	1; 2; 3	Port 110	80	1	761 ± 34
22144 to 22146	1; 2; 3	Port 110	82	1	1279 ± 17
22143	1; 2; 3	Port 110	85	1	2732 ± 61
22141	1; 2; 3	Port 110	90	1	3234 ± 61
22172 to 22173	1; 2; 3	Port 110	100	1	3595 ± 26
22401 to 22410	1; 2; 3	Pump port 3	100	1	661 ± 4
23992 to 23995	1; 2	Pump port 3	100	1	6500 ± 100

Table 5.4: **Parameters for measurements with an additional radon source at different temperatures.** The valve of the $^{220}\mathrm{Rn}$ source is opened to 100% and connected to pump port 3 for all measurements. In the table the run numbers, the temperature range of baffle 3 and the mean cluster rate are listed. These cluster rates have to be taken only as a first impression since the values are unstable due to the variation of the temperature. The temperature of baffle 3 is approximated by the sensor positioned in the middle of the baffle (KATRIN number 435-RTP-5-3082). Please note that the runs 23964 to 23966 were taken during the warm-up of the baffle which is why no useful mean rate can be given.

Measurement	Runs	Pressure in mbar	Baffles varying in temperature	Temperature range of baffle 3 in K	Mean cluster rate in mcps
1	22395 to 22410	10^{-8}	1; 2; 3	86.9 to 88.6	10.8 ± 0.5
2	23807 to 23809	$< 10^{-8}$	3	88 to 96.3	81 ± 2
3	22429 to 22443	$< 10^{-8}$	3	97 to 101	126 ± 2
4	22459 to 22472	$< 10^{-8}$	3	100.2 to 113	173 ± 2
5	23964 to 23966	10^{-8}	3	87.4 to 128.6	-
6	23992 to 23995	10^{-8}	3	290.4 to 292.3	378 ± 5

Table 5.5: **Settings for the liquid-nitrogen flow through baffle 3.** The liquid-nitrogen flow through baffle 3 is defined by four set parameters: the minimum temperature $T_{\min}$, the temperature increase ΔT, the minimal and maximal valve-opening positions $v_{\min}$ and $v_{\max}$. These values are summarised for the measurements 1 to 4.

Measurement	Runs	Temperature range of baffle 3 in K	$T_{\min}$ in K	ΔT in K	$v_{\min}$ in %	$v_{\max}$ in %
1	22395 to 22410	86.9 to 88.6	82.4	3.8	1.9	4.0
2	23807 to 23809	88 to 96.3	84	14	1.8	3.1
3	22429 to 22443	97 to 101	96.6	9	1.8	4.0
4	22459 to 22472	100.2 to 113	104.8	14	1.8	3.8

5.2 Background reduction by liquid-nitrogen cooled copper baffles

A major goal of the SDS-II commissioning phase was to quantitatively determine the reduction of the radon-induced background by liquid-nitrogen cooled copper baffles. In order to investigate this reduction different combinations of baffles were cooled down to liquid-nitrogen temperatures while the detector rate was measured in the region of interest. A summary of the measurements taken can be found in table 5.2.

5.2.1 Determination of radon-induced backgrounds and the remaining background rate

The reduction of radon-induced background with different baffles operating at liquid-nitrogen temperatures enables the determination of the remaining background, which is not induced by stored particles, and the efficiency of the suppression of observable radon-induced decays. In order to gain knowledge on these parameters a greatly simplified background model needs to be established first.

The background observed by the detector can be separated into three components with respect to radon-induced events:

- The first component of the background is the radon-induced background which consists of clusters obtained by the inter-arrival time cut ($\Delta t \leq 0.2\,\mathrm{s}$) and the multiplicity cut ($N \geq 5$). As an abbreviation C_{Rn} will be used in the following.
- The second component of the background is the radon-induced background which is not contained within clusters. One reason for the loss of clusters is the multiplicity cut. An additional reason is the possibility of a radon decay yielding only one electron arriving at the detector. Such single electrons cannot be separated from other backgrounds. Lastly, there is also an enhanced probability that they leave the main spectrometer in the direction of the pre-spectrometer. This does also reduce the observed multiplicity and might put the number of events reaching the detector below the multiplicity threshold. As an abbreviation S_{Rn} will be used in the following.
- The last component is background which is not induced by radon in general. As an abbreviation R will be used in the following.

With these three fractions the total background rate R_{tot} can be expressed as

$$R_{\mathrm{tot}} = C_{\mathrm{Rn}} + S_{\mathrm{Rn}} + R. \tag{5.12}$$

C_{Rn} and S_{Rn} are both produced as a consequence of radon decays. Since the energy of the stored primary electron determines the number of produced secondary electrons the ratio between C_{Rn}

and S_{Rn} depends on the energy distribution of the primary electrons (see section 3.2), but, in particular, is independent of the number of radon α-decays and thus independent of the baffle temperature. This allows to use the simplification

$$\frac{S_{\mathrm{Rn}}}{C_{\mathrm{Rn}}} = \alpha = \mathrm{const.} \tag{5.13}$$

which leads to

$$R_{\mathrm{tot}} = C_{\mathrm{Rn}} \cdot (1 + \alpha) + R \tag{5.14}$$

Formula (5.14) states that the total rate scales linearly to the rate C_{Rn} found in clusters. In addition, the R_{tot}-intercept gives the remaining background which is induced by non-radon-like events R. Moreover, the remaining background rate originated by radon for three cold baffles can be determined. In this case, the remaining radon-induced background rate R_{Rn} can be calculated:

$$R_{\mathrm{Rn}} = r_{\mathrm{cb}} - R \tag{5.15}$$

where r_{cb} is the mean background rate for 3 cold baffles. In principle, it is possible to correct the absolute background rates with respect to the removal of the non-working 6 detector pixels, assuming that the background scales linearly with the number of pixels taken into account. This is only correct in a first approximation, since each detector ring maps a different flux-tube volume. However, the difference of the observed value is smaller than $10\,\%$. Therefore, the corrected remaining background rate by non-radon events is R_{cor} and the remaining radon-induced background is $R_{\mathrm{Rn,cor}}$ for 148 pixels.

$$R_{\mathrm{cor}} = \frac{148}{142} \cdot R \tag{5.16}$$

$$R_{\mathrm{Rn,cor}} = \frac{148}{142} \cdot R_{\mathrm{Rn}} \tag{5.17}$$

In order to confirm (5.15) and to gain insight into the remaining background rate measurements with varying amounts of radon α-decays inside the main-spectrometer volume were performed. Since the NEG pumps are a known radon source it was possible to vary the amount of radon decaying in the flux tube by utilizing different combinations of baffles cooled to liquid-nitrogen temperatures. In total, measurements were taken with warm baffles, baffle 1 cold, baffles 1 and 2 cold, and baffles 1, 2 and 3 cold. A summary of the performed background runs and important measurement parameters can be found in table 5.2. The results of these measurements for clusters with multiplicities $N \geq 5$ and inter-arrival times $\Delta t \leq 0.2\,\mathrm{s}$ are shown in figure 5.5. A linear function representing (5.15) is fitted to the taken data points. This fit yields a remaining background rate of $R = (0.562 \pm 0.002)\,\mathrm{cps}$ for 142 pixels which is not induced by stored particles. Furthermore, the liquid-nitrogen cooled copper baffles reduce the observed background significantly from $(1.064 \pm 0.004)\,\mathrm{cps}$ to $(0.587 \pm 0.002)\,\mathrm{cps}$. Therefore (5.15) yields $R_{\mathrm{Rn}} = (0.025 \pm 0.003)\,\mathrm{cps}$ which is still a factor of 2.5 larger than the designed rate of $0.01\,\mathrm{cps}$ required to achieve the specified sensitivity of the KATRIN experiment. In order to be able to suppress the radon-induced background more efficiently additional active background-removal methods are needed. Promising methods are electron cyclotron resonance [Mer13], or the utilization of static and pulsed electric dipoles or magnetic pulses [Wan13].

In order to gain better statistics additional measurements were performed with an artificial radon source. The valve separating the radon source and the main spectrometer was opened to certain positions given in percentages and the position of the radon source was varied as well. The performed measurements can be found in table 5.3. The taken data points are diagrammed in figure 5.6. In addition a linear fit is shown. Within the uncertainties of the fits the remaining background rate $R = (0.564 \pm 0.002)\,\mathrm{cps}$ is the same as without the $^{220}\mathrm{Rn}$ source. The remaining radon-induced background rate is also similar with $R_{\mathrm{Rn}} = (27 \pm 3)\,\mathrm{mcps}$. The slope of the fit remains

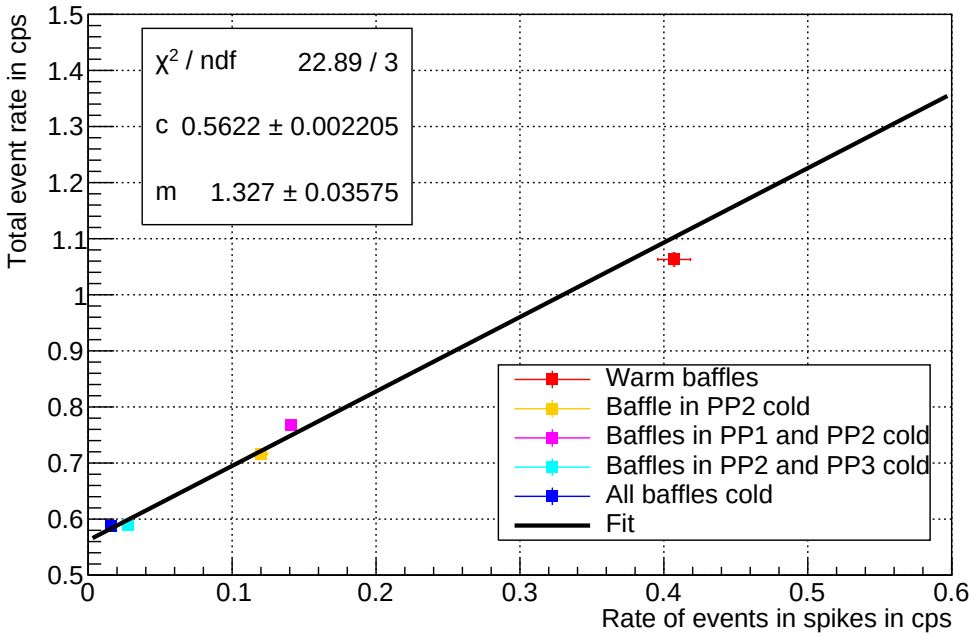

Figure 5.5: **Total event rate over event rate within clusters for the background measurements.** The total event rate in dependence of the rate of events contained in clusters is given. The data points are obtained with different sets of cold baffles: all baffles warm (red), the baffle in pump port 2 cold (orange), the baffles in pump ports 1 and 2 cold (magenta), the baffles in pump ports 2 and 3 cold (cyan), and all three baffles cold (blue). A linear function $R_{\mathrm{tot}} = m \cdot C_{\mathrm{Rn}} + c$ is fitted to these data points (black line).

unchanged within the observed uncertainties. The consistency of the background measurements with and without additional radon source is a strong evidence that the background is induced by radon. An effect of the cooling of the operating baffles to liquid-nitrogen temperatures indicates radon as a background source as well.

When the source is connected to the main spectrometer directly (port 110) and the corresponding valve fully opened the measurement point drops off from the linear fit. One reason is the overlap of clusters discussed in section 5.1. Another oddity is that the rates for one cold baffle in pump port 2 are lower than for cold baffles in pump ports 1 and 2. This is the inverse of the expected order. This will be discussed in section 5.3.

In addition to the remaining background rate the efficiency of the radon suppression can be calculated for different setups of the three operating copper baffles.

5.3 Suppression of radon-induced background by the copper baffles

The efficiency ϵ of the suppression of the background induced by radon α-decays is calculated by comparing the number of clusters found into two data samples with different baffle configurations. As reference value the measurements with warm baffles were taken.

$$\epsilon = 1 - \frac{C_{\mathrm{s1}}}{C_{\mathrm{s2}}} \tag{5.18}$$

where C_{s1} and C_{s2} are cluster rates for measurements with two different combinations of cold baffles. The configurations used are summarised in table 5.3. The corresponding efficiency is calculated for multiplicity cuts ranging from 2 to 20 to study the dependency.

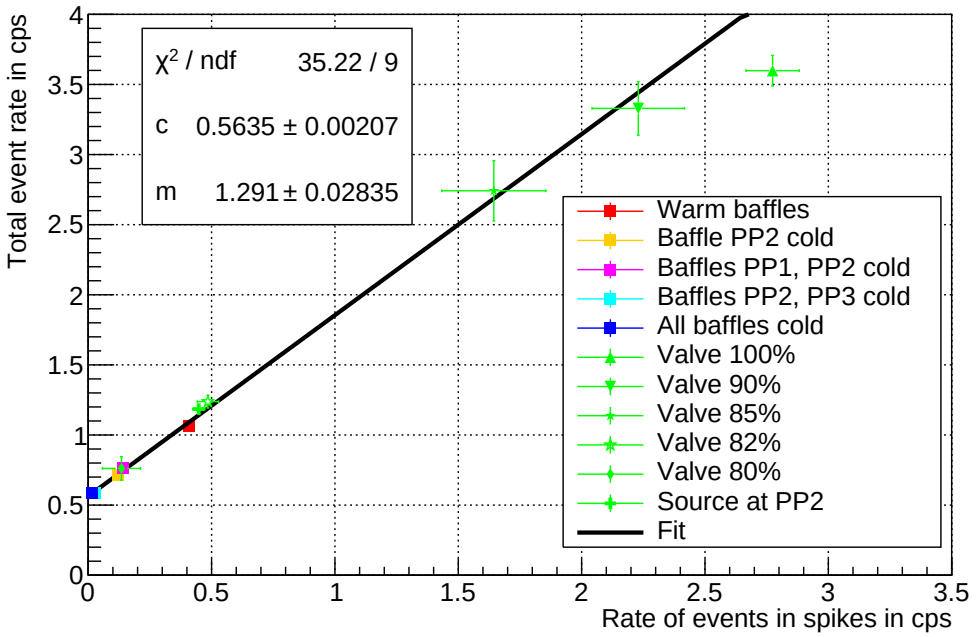

Figure 5.6: **Total event rate over event rate within clusters for measurements with and without artificial radon source.** The background runs are colour coded as in figure 5.5. The measurements with the artificial radon source are taken with three cold baffles (green). The measurements with the radon source include measurements with the source mounted on top of the main spectrometer with valve-opening positions varying between 80 % and 100 % and one measurement with the source mounted in pump port 2 behind the baffle system (green cross). A linear function $R_{\mathrm{tot}} = m \cdot C_{\mathrm{Rn}} + c$ is fitted to these data points (black line).

5.3.1 Efficiency of the suppression of radon-induced background

The suppression efficiency of the number of observed clusters is determined for different baffle configurations. The highest efficiency is expected when comparing the measurements with all 3 baffles cooled to liquid-nitrogen temperatures ($T = 86\,\mathrm{K}$) with measurements at room temperature ($T = 292\,\mathrm{K}$). The resulting multiplicity dependence of the efficiency is plotted in figure 5.7. It is evident that for low multiplicities of $N < 5$ the determined efficiency deviates strongly from the mean value. As discussed already in section 5.2.1 the reason is the contribution of accidental accumulations of events forming false clusters. Consequently, only multiplicity thresholds of $N \geq 5$ are taken into account to calculate the mean efficiency. Events caused by radon α-decays are suppressed efficiently which confirms the results obtained during SDS-I [Goe14] [Sch14]. Furthermore, the actual efficiency found by this conservative approach is $\epsilon = 97^{+2}_{-3}\,\%$. The efficiency increases for all sets and is not distributed randomly around the mean. The reason is that the measurement points are correlated due to the integral character of this analysis method: The same cluster number used for a certain threshold N_1 is contained within all data sets with multiplicities of $N_2 < N_1$. The surplus of high-multiplicity clusters for warm baffles is present when comparing it to all other background measurements. Its cause might be a certain fluctuation of the cluster count of the measurements with warm baffles.

Efficiency 1 from table 5.6 gives the reduction for one single cold baffle. In the simplified case of $^{219}\mathrm{Rn}$ emanated from the NEG material in the pump ports 2 and 3 dominating the radon-induced background, the optimal possible efficiency is 75 %. A reduction of 50 % is expected since baffle 2 blocks the direct line of sight of the getter material in pump port 2 to the main-spectrometer volume and fully suppresses $^{219}\mathrm{Rn}$ coming from the NEG strips in the ideal case. Additionally,

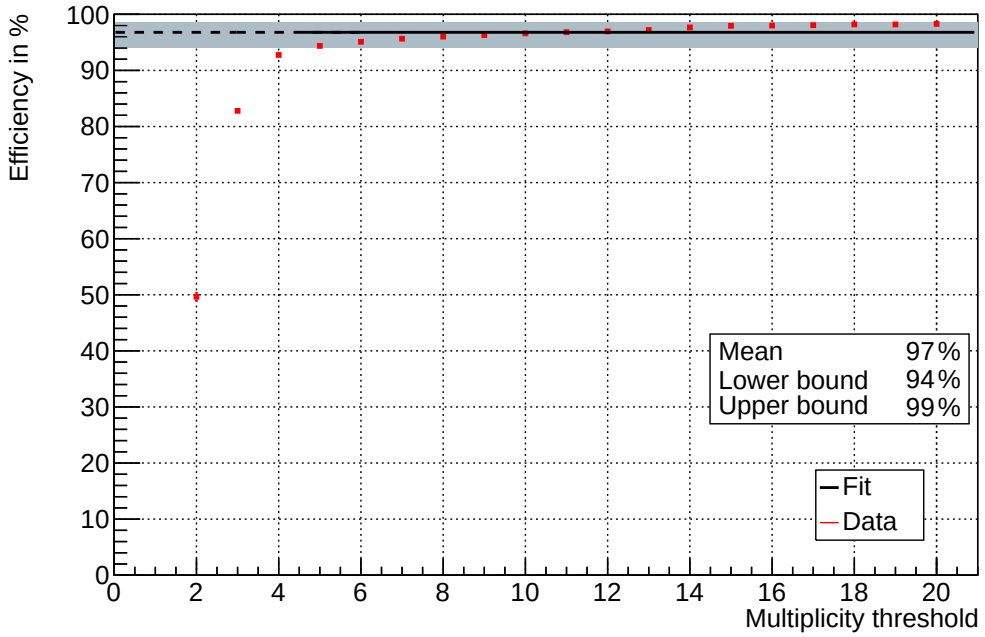

Figure 5.7: **Cluster-suppression efficiency of three cold baffles in dependence of the cluster multiplicity.** The efficiency is calculated according to (5.18) with setting 1 being the combination of three cold baffles and setting 2 utilising three warm baffles. The resulting efficiency is plotted in dependence of the multiplicity threshold applied for the cluster determination (red). In addition, the mean multiplicity calculated for $N \geq 5$ is shown (black line). Furthermore, a conservative uncertainty approximation is done by taking the lowest and the highest efficiency contained within the one-sigma intervals of efficiencies $N \geq 5$ (grey band). The resulting suppression efficiency provided by the liquid-nitrogen cooled copper baffles is $\epsilon = 97^{+2}_{-3}\,\%$.

for optimal conditions a reduction of $50\,\%$ for the radon emanated by the getter material in pump port 1 is expected. The value obtained by the measurements is $71^{+7}_{-10}\,\%$ and is consistent with the basic expectations.

When comparing efficiencies 1 and 2 from table 5.6 the additional effects on the cool-down of the baffle in pump port 1 which does not contain any NEG material is studied. The additional efficiency is expected to be around $50\,\%$ of the remaining rate. However, no change is observed within the error estimation of $66^{+10}_{-9}\,\%$. When comparing the amount of clusters directly the efficiency obtained by the cool-down of baffle 1 is $-16^{+18}_{-17}\,\%$. Within the estimated uncertainties the reduction is barely compatible with 0. This behaviour is not consistent with the expectations and is difficult to explain. As several months have passed between the two measurements there is a possibility that hardware changes have influenced the observed rates. One major change was the additional installation of the radon source. However, the corresponding valve was fully closed during the measurements and no significant contribution of the isolated source is expected.

The cool-down of the baffles in pump ports 2 and 3 yields an efficiency of cluster suppression by $93^{+3}_{-2}\,\%$. This translates to an additional suppression of $\epsilon_6 = 77^{+7}_{-3}\,\%$ when comparing to the baffle in pump port 2 cold only. The additional cool-down of baffle 3 has about the same impact as the cool-down of baffle 2. Due to the shielding of the NEG material in pump port 2 by the corresponding baffle, a lower value is expected for equally operating baffles. It is possible to explain this with different suppression efficiencies of baffles 2 and 3. Further proof of this solution can be obtained by comparing the cluster rate with an additional radon source temporarily installed

Table 5.6: **Summary of the background measurements with different cooled baffles.** The measurements summarised in table 5.2 are used to calculate the influence of the baffle cooldown to the cluster rate. As reference, the efficiency calculations are shown, as well as the two settings C_{s1} and C_{s2} which are compared and the mean efficiency which is determined for $N \geq 5$.

Efficiency	Setting C_{s1} Baffles cold	Setting C_{s2} Baffles cold	Mean efficiency in %
1	2	none	71^{+7}_{-10}
2	1; 2	none	66^{+10}_{-9}
3	2; 3	none	93^{+3}_{-2}
4	1; 2; 3	none	97^{+2}_{-3}
5	1; 2	2	-16^{+18}_{-17}
6	2; 3	2	77^{+7}_{-3}
7	2; 3	1; 2	80^{+6}_{-3}
8	1; 2; 3	2; 3	49^{+25}_{-19}

in the corresponding pump ports (see section 5.3.2). Lastly, a comparison with the measurements with baffles 1 and 2 cold is done. For the scenrio of radon being primarily emanated from the main spectrometer vessel it is expected that the two scenarios do not differ. However, the resulting efficiency $\epsilon_7 = 80^{+6}_{-3}\,\%$ is not compatible with 0. This is a strong indication that the NEG material residing in pump ports 2 and 3 is the dominant radon source in the main spectrometer.

The most important measurement of three copper baffles cooled to liquid-nitrogen temperatures was discussed above in detail. The resulting efficiency is $\epsilon_4 = 97^{+2}_{-3}\,\%$. When comparing this value to the measurements with baffles 2 and 3 cold a second approach to determine the efficiency of baffle 1 becomes available. This results in an additional efficiency of $\epsilon_8 = 49^{+25}_{-19}\,\%$ which is in agreement with the values of the other two baffles. However, it also contradicts the comparison of baffle 1 cold with baffles 1 and 2 cold which results in $\epsilon_5 = -16^{+18}_{-17}\,\%$.

A more dedicated analysis of the suppression efficiency, of the remaining background rate and of the total radon emanation rate is established in [Har15].

5.3.2 Measurements with an additional radon source

In addition to the determination of the background reduction for different baffle combinations, measurements with an additional $^{220}\mathrm{Rn}$ source were performed. This enables another way to determine the efficiencies of the baffles. However, it has to be taken into account that the source behaves differently since it is a $^{220}\mathrm{Rn}$ source while the main source of the radon background is expected to be $^{219}\mathrm{Rn}$ from the getters. Due to its longer half-life it is expected that for radon atoms being emanated behind the baffles in one of the pump ports the suppression efficiency is decreased when compared to $^{219}\mathrm{Rn}$ since they have more time to pass the baffle.

In the case of radon residing in the main spectrometer vessel the efficiency of reduction is increased for $^{220}\mathrm{Rn}$ due to its longer half-life. In this case the longer half-life increases its chances to be adsorbed by a baffle before it decays.

The efficiency calculations are summarised in table 5.7 while an overview of the measurements can be found in table 5.3.

Effect of the baffle blocking the direct line of sight of the source to the main spectrometer

Firstly, the measurement with the radon source at pump port 3 will be discussed. During the first measurement baffles 1 and 2 were held at liquid-nitrogen temperatures, during the second one the

Table 5.7: **Summary of the measurements with an additional radon source and different cooled baffles.** The efficiencies are calculated based on the measurements summarised in table 5.3. The efficiencies are listed for reference purposes together with the settings of the operating baffles and the position of the radon source.

Efficiency	Setting C_{s1} Baffles cold	Setting C_{s1} Source position	Setting C_{s2} Baffles cold	Setting C_{s2} Source position	Efficiency in %
1S	1; 2; 3	at pump port 3	1; 2	at pump port 3	99^{+1}_{-1}
2S	1; 2; 3	at pump port 3	1; 2; 3	at pump port 2	87^{+5}_{-5}
3S	1; 2; 3	at pump port 3	1; 2; 3	at port 110	98^{+1}_{-2}
4S	1; 2; 3	at port 110	1; 2	at pump port 3	56^{+11}_{-9}
5S	1; 2; 3	at pump port 2	1; 2; 3	at port 110	81^{+9}_{-5}

baffle in pump port 3 was cooled, too, thus thermally blocking the direct line of sight of the source to the flux tube. The resulting efficiency is $\epsilon_{1\mathrm{S}} = 99^{+1}_{-1}\,\%$. This means that even for $^{220}\mathrm{Rn}$ baffle 3 suppresses radon stemming from the region in the pump port separated from the main spectrometer by the baffle. This result implies an even better suppression factor for $^{219}\mathrm{Rn}$ emanating from the same region. Furthermore, the measurement with cold baffles and the radon source connected to pump port 3 has an enhanced remaining cluster rate ($C_{\mathrm{Rn}} = (661 \pm 4)\,\mathrm{mcps}$) when compared to the measurements without radon source ($C_{\mathrm{Rn}} = (587 \pm 2)\,\mathrm{mcps}$). This signifies that even at the lowest temperatures a significant amount of $^{220}\mathrm{Rn}$ is able to pass the baffle before decaying.

Effect of one warm baffle to the background rate

When comparing the cluster rate of a measurement with the source mounted directly to the main spectrometer with a measurement where the source is attached to pump port 3 and the corresponding baffle is warm, the rate decreases by $\epsilon_{4\mathrm{S}} = 56^{+11}_{-9}\,\%$. The effect of the source position contributes only an increase of about $2\,\%$ when connecting the source directly to the main spectrometer. However, here an opposing effect is observed. It originates from the reduction of the number of baffles pumping $^{220}\mathrm{Rn}$ by cryosorption out of the sensitive main-spectrometer volume.

Effect of positioning the radon source behind the cold baffle to the background rate

It is possible to study the influence of the positioning of the $^{220}\mathrm{Rn}$ source with three cold baffles. Firstly, the effect of repositioning it from pump port 3 to pump port 2 is investigated. This yields a suppression by $\epsilon_{2\mathrm{S}} = 87^{+5}_{-5}\,\%$. This is not fully understood since under equal measurement conditions it is not supposed to matter whether the radon source is put to pump port 2 or 3. One explanation is that the baffle in pump port 2 does not have the same operating temperature as baffle 3 and therefore does not contribute the same efficiency. One possible explanation for these differences is that the instrumentation with the temperature sensors of the two baffles is realised differently. While the setup remained unchanged in baffle 2 since SDS-I the thermal coupling of the temperature sensors in pump port 3 was improved. It is suggested to implement the changes also for the temperature sensors residing in pump port 2.

In addition the change of efficiency can be observed for a $^{220}\mathrm{Rn}$ source being connected to the main spectrometer and to pump port 2. The resulting efficiency is $\epsilon_{\mathrm{S5}} = 81^{+9}_{-5}\,\%$. The difference originates from the necessity of a radon atom to traverse through the baffle when the radon source is located at the pump port.

The same comparison can be done with pump port 3 instead of pump port 2. The resulting efficiency is $\epsilon_{3\mathrm{S}} = 98^{+1}_{-2}\,\%$.

To summarise, these comparisons yield that the baffles are not equally effective at suppressing contributions to the background rate induced by radon decays. Additionally, there is a significant

effect on the cluster rate of thermally blocking the direct line of sight between the radon source and the main spectrometer.

5.4 Temperature dependence of the suppression of the radon-induced background

The $^{220}\mathrm{Rn}$ source was connected to pump port 3 to study the influence of the temperature of the corresponding baffle on the suppression of radon-induced background. In total, six sets of measurements with different mean temperatures and temperature variations were taken, which are summarised in table 5.4.

5.4.1 Temperature variation by refilling the liquid-nitrogen supply tank

For the first measurement the liquid-nitrogen flow was adjusted to ensure the lowest possible temperatures (measurement 1 in table 5.4). During the measurement the liquid-nitrogen supply tank was refilled. This process lead to a temperature variation for all three baffles, shown in figure 5.8. The sensors residing in the middle of baffles 1 and 3 show temperatures below $90\,\mathrm{K}$ and follow the same progression. The sensors at the side of the baffles 1 and 3 and the sensors of baffle 2 return higher temperatures. Moreover, they do not follow the trend of the sensors in the middle of the baffles. The temperature of each sensor depicted in a temperature regime varying from $130\,\mathrm{K}$ to $160\,\mathrm{K}$ follows a different time dependency. The temperature measured by the sensor residing at the side of baffle 1 rises firstly and then drops to lower values. The temperatures of baffle 2 are unaffected. The sensor positioned at the side of baffle 3 shows a small rise in temperature at first, followed by a decrease.

The temperatures of all baffles vary due to the refill of the liquid-nitrogen supply tank resulting in a certain correlation of the temperatures of the baffles. Therefore, it is difficult to disentangle the contributions of the temperature of the three baffles to the suppression of the cluster rate. The sensors of baffle 3 are expected to be the most important ones since the direct line of sight from the additional radon source to the main spectrometer is blocked by this baffle. The temperature and the rate of observed clusters induced by radon α-decays are shown in figure 5.9 in the bottom left for the middle sensor and in the bottom right for the side sensor. The temperature of both sensors and the cluster rate follow a similar behaviour. Both the temperature of the sensor in the middle of baffle 3 and the cluster rate show an increase after $3\,\mathrm{h}$. The temperature of the sensor on the side lags behind with a maximum at about $4\,\mathrm{h}$. The data suggests a correlation between the temperature of the baffles and the cluster rate. This behaviour is expected for the adsorption of radon by the liquid-nitrogen cooled copper baffles under the assumption that the half-life of radon and its desorption time have similar magnitudes.

The setting was chosen for the lowest possible temperatures. An increase of $0.5\,\mathrm{K}$ results in a doubling of the rate. Therefore, it is crucial to ensure that all three baffles are operated at the lowest temperature achieved with baffle 3 to reach the maximal reduction of radon-induced background with this system.

Lastly, the rate shows a significant peak after a run time of $1\,\mathrm{h}$. The width and height of this peak are not reproduced by the temperature trend of baffle 3. One possible explanation is the additional occurrence of peaks in the temperature trend of baffles 1 and 2. Consequently, the temperature at the middle of baffle 1 (figure 5.9 upper left) and at the side of this baffle (figure 5.9 upper right) are both compared with the rate trend. This peak after $1\,\mathrm{h}$ implies that not only the temperature of the sensor in the middle of baffle 3 influences the cluster rate but the temperature of baffle 1 contributes to the rate change as well. However, the slope in the first hour of the measurement is not reproduced by this temperature trend. In addition, the bottom sensor of baffle 1 shows an additional increase after $4.5\,\mathrm{h}$ (see figure 5.8 bottom). This is not reflected in the cluster rate trend.

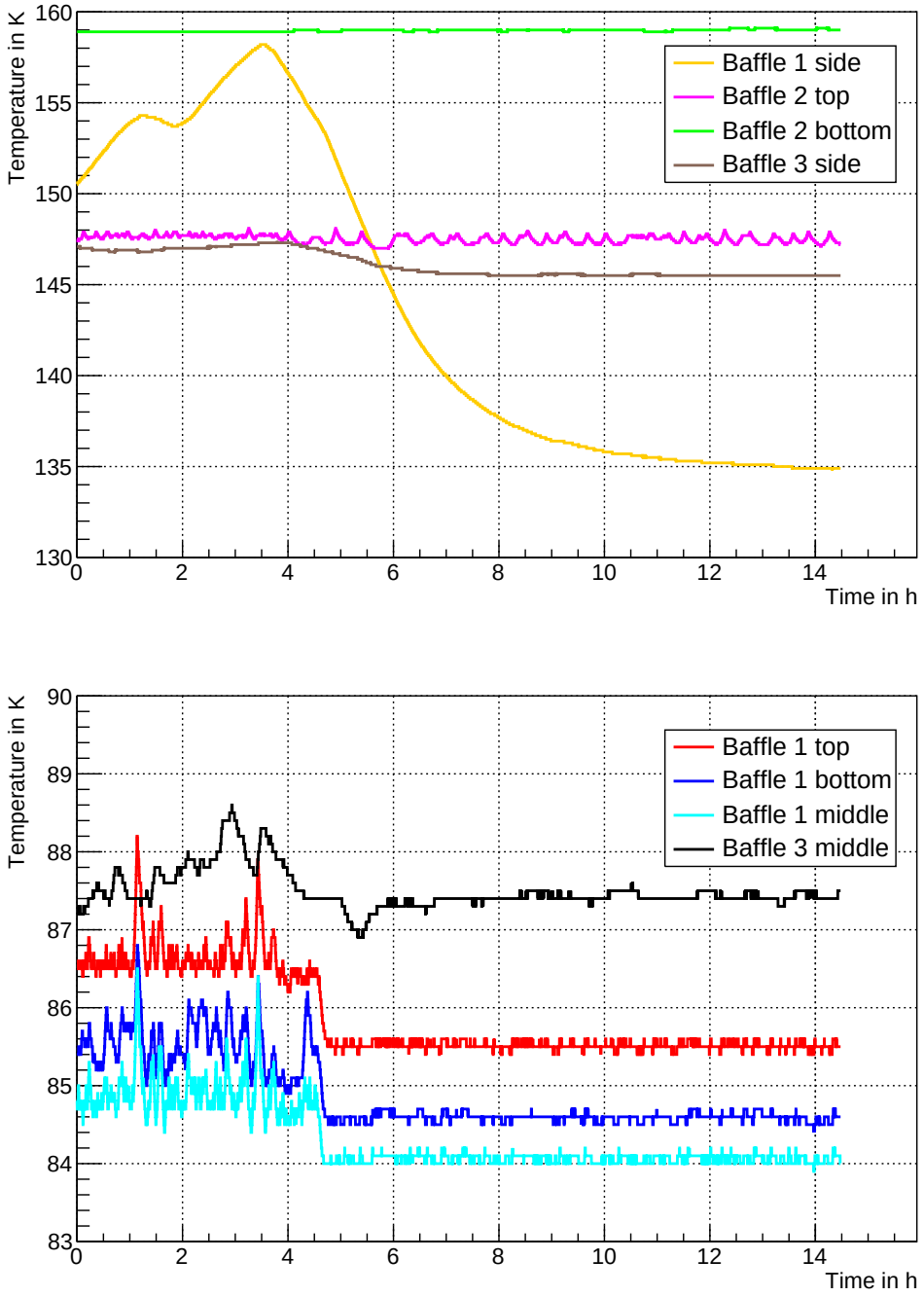

Figure 5.8: **Variation of temperatures of the three copper baffles after the refill of the liquid-nitrogen supply tank.** The temperature of the three baffles residing in the respective pump ports is monitored by several sensors for each baffle. The temperatures measured by the operational sensors are plotted. In the **top** graph the response of the sensors at elevated temperatures are shown: the sensor at the side of baffle 1 (orange), the sensor at the top (magenta) and at the bottom (green) of baffle 2 and the sensor at the side of baffle 3 (brown). In the **bottoms** graph the sensors returning temperatures in the range of the liquid-nitrogen regime are plotted. The sensor at the top (red line), bottom (blue line), and middle (cyan line) of baffle 1 and the sensor in the middle of baffle 3 (black line) are shown.

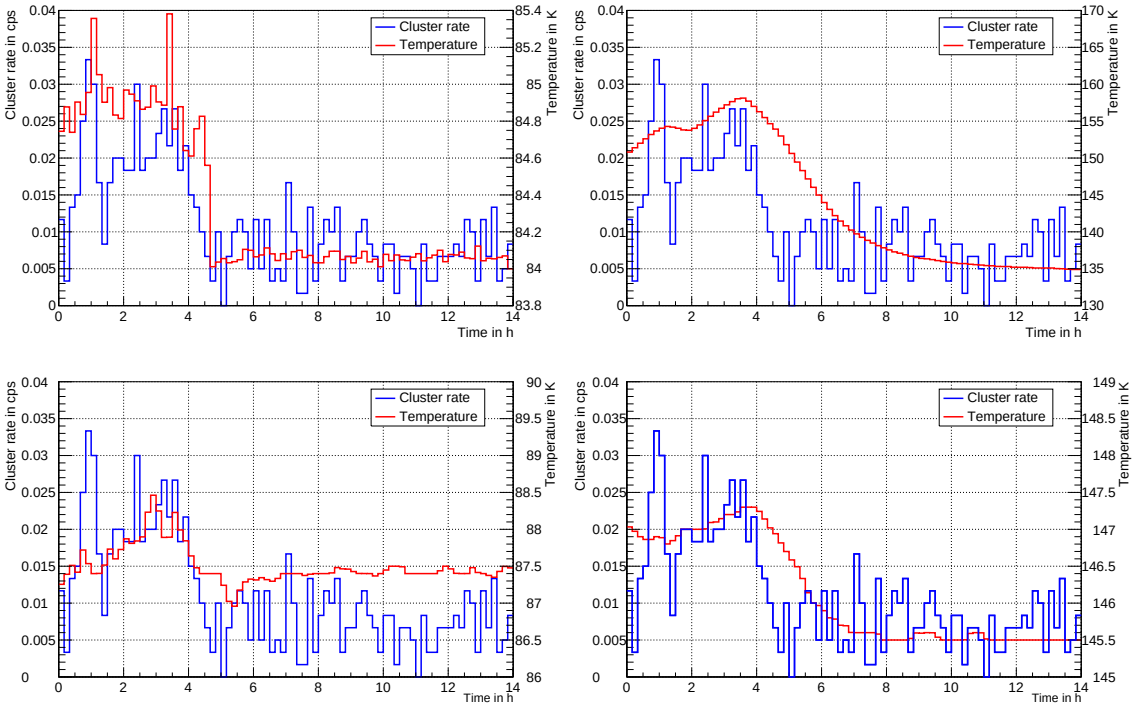

Figure 5.9: **The temperature and rate variations of measurement 1 (table 5.4) for the temperature sensors attached to baffles 1 and 3.** The temperature (red) and the cluster rate (blue) are plotted. The time bin width is set to 600 s in order to get a useful average of the low cluster rate while only few rate bins are empty. **Top left:** Sensor in the middle of baffle 1. **Top right:** Sensor at the side of the baffle 1. **Bottom left:** Sensor in the centre of the baffle 3. **Bottom right:** Sensor at the side of the baffle 3.

To summarise, the rate trend depends on the temperature change of the middle sensors of baffles 1 and 3. Furthermore, the refilling of the liquid-nitrogen tank increases the background rate induced by radon α-decays. This might make it necessary to exclude the first 4 h of data from the neutrino-mass measurements following the completion of the refill.

5.4.2 Targeted temperature variation of the baffle in pump port 3

The temperature of baffle 3 was varied by controlling the liquid-nitrogen flow in order to collect information on its influence on the cluster rate induced by the radon source. In comparison to measurement 1 no influences of baffles 1 and 2 need to be considered since their temperature were stable during the measurements. Five sets of data were taken, each with unique setups. Measurements 2 to 6 which are summarised in tables 5.4 and 5.5 are used. Each setting is evaluated both for the temperature sensor in the centre and at the side of baffle 3.

Cyclic measurements

The targeted cyclic measurements 2 to 4 have the advantage that a correlation between temperature and cluster rate can be verified unambiguously by observing the same cyclic changes of both parameters. In figure 5.10 the detector rate and the temperature of baffle 3 are plotted for measurements 2 (top) and 3 (bottom). The same procedure is followed for measurement 4 in figure 5.11.

All graphs on the left show the central sensor while the ones on the right show the sensor located at the side of baffle 3. From all three data sets it is obvious that the cyclic variations of the cluster rate are not reflected in the temperature trend of the sensor at the side. There is no visible

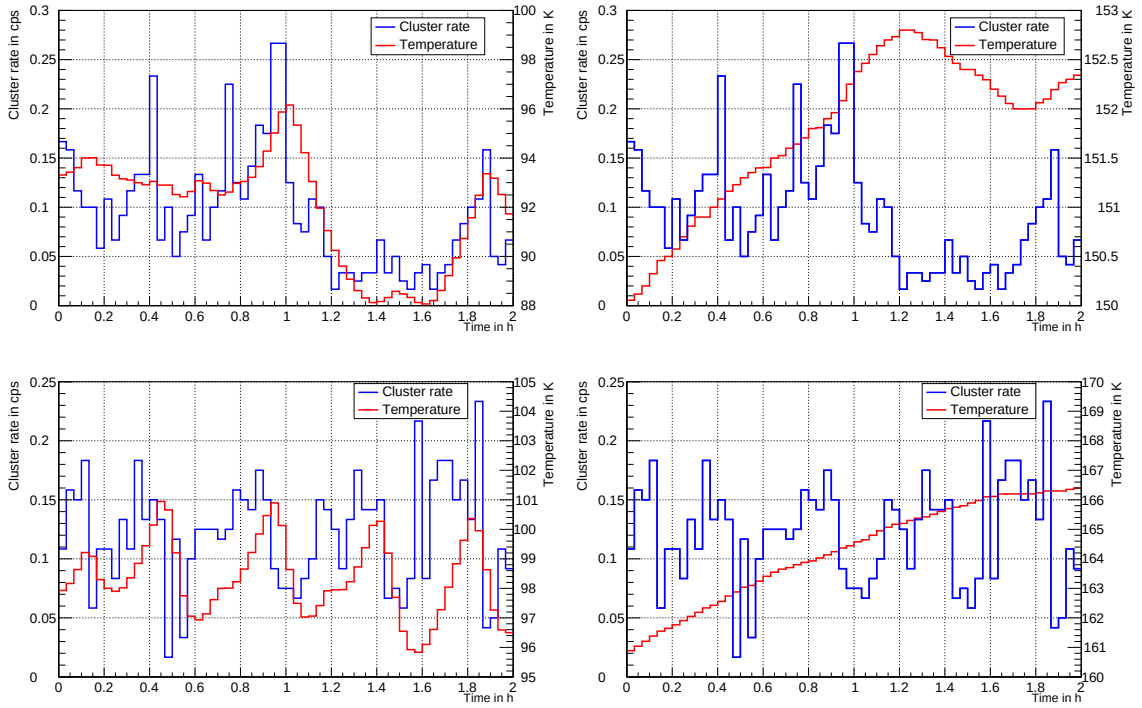

Figure 5.10: **The temperature and rate variations of the cyclic measurements 2 and 3 (table 5.4) for the temperature sensors attached to baffle 3.** The temperature (red) and the cluster rate (blue) are plotted. The time bin width is set to 120 s. The utilisation of the settings of measurement 2 and the sensor in the middle yields the graph in the **top left** while the sensor residing at the side of the baffle results in the **top right** diagram. The same is done for measurement 3 with the data of the sensor in the middle shown in the **bottom left** while the temperature of the sensor at the side is in the graph at the **bottom right**.

correlation between this sensor and the cluster rate within one run. The sensor in the centre, however, behaves differently. It is obvious that its temperature trend mirrors the shape of the cluster rate. Accordingly, it is plausible that the baffle as a whole follows a similar temperature trend as the central sensor and not a trend like the sensor on the side. The latter faces the pump-port walls which emit heat radiation. This is one possible reason for the sensor at the side showing atypical elevated temperatures. This way, the resulting temperature is not dominated by the oscillating liquid-nitrogen feed-through. Besides the obvious likeness of the shape of the central temperature sensor and the cluster rate a certain shift is visible. One possible reason for this shift is that only one local measurement of a sensor is taken into account here while the temperature distribution of the entire baffle is unlikely to be homogeneous at elevated temperatures and not known. Consequently, the effective temperature of the whole baffle is possibly shifted with respect to the readout of the central sensor. This hypothesis is investigated more detailed in section 5.4.4.

Measurement during warm-up of baffle 3

Measurement 5 was taken during the first 1.5 h of the warm-up of baffle 3. The corresponding temperatures and the cluster rate are depicted in the top graphs of figure 5.12. For the sensor in the middle of the baffle the temperature and the rate follow the same trend for about 0.6 h corresponding to a temperature of about 105 K. With the passing time the cluster rate increases slower and saturates after approximately 1 h at a rate of $C_{\mathrm{Rn}} = 378\,\mathrm{mcps}$ and a temperature of $T = 115\,\mathrm{K}$. In summary, the cluster rate is only dependent on the temperature of the baffle for temperatures below 115 K at its centre.

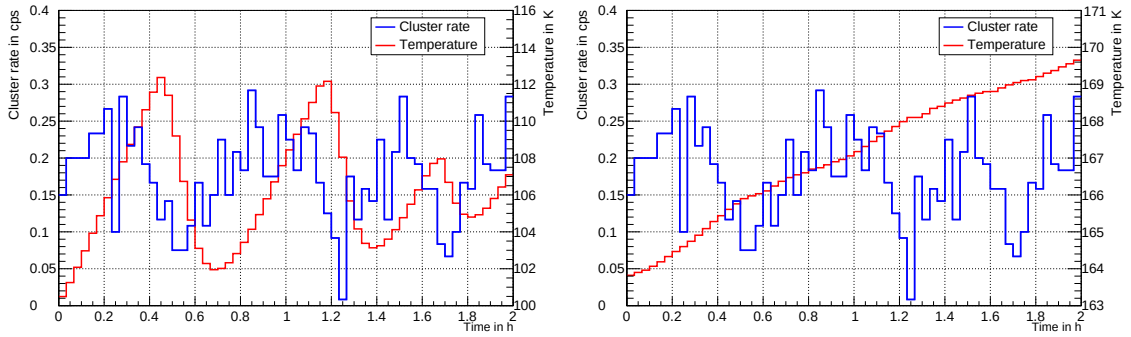

Figure 5.11: **The temperature and rate variations of the cyclic measurement 4 (table 5.4) for the temperature sensors attached to baffle 3.** The temperature (red) and the cluster rate (blue) are plotted. The time bin width is set to 120 s. The utilisation of the settings of measurement 4 and the sensor in the middle yields the graph in the **left** while the sensor residing at the side of the baffle results in the **right** diagram.

The sensor at the side of the baffle shows a similar behaviour. However, the slope of the corresponding temperature differs from the one of the cluster rate. Once again, the sensor at the side of the baffle shows worse agreement with the cluster rate than the sensor located in the centre of baffle 3.

Measurements with warmed-up baffle 3

Measurement 6 was performed when the baffle was nearly at room temperature. The temperature and the rate trends can be found in the bottom graphs of figure 5.12. In this case the cluster rate does not depend on the temperatures. However, this measurement yields the maximum of the observed radon-induced background due to the radon source located at pump port 3. This is important in order to determine the efficiency of the suppression of radon-induced events as a function of the temperature which is the focus of the next section.

5.4.3 Dependency of the cluster rate on the temperature of baffle 3

From the previous section 5.4.2 it has become evident that the cluster rate is dependent on the temperature of baffle 3 which is best represented by the central temperature sensor. Additionally, the cluster rate saturates at a certain temperature which corresponds to roughly 115 K. Moreover, at low temperatures the cluster rate is very small. All in all, this behaviour is described by an arctangent function as given in (4.26). In order to express the dependency of the temperature instead of the desorption time (3.6) is used. The resulting function is:

$$C_{\mathrm{Rn}}(T) = p0 \cdot \arctan\left(p1 \cdot \exp\left(\frac{-p2}{R \cdot T}\right) + p2\right) + p3 \tag{5.19}$$

where $C_{\mathrm{Rn}}(T)$ is the cluster rate at temperature T, $R = 8.314\,46\,\frac{\mathrm{J}}{\mathrm{mol\,K}}$ is the gas constant and p0 to p3 are arbitrary parameters. When either p0 or p1 are used as fit parameters the fits yields negative values. To prevent this non-physical parameter space the lower limit of $C_{\mathrm{Rn}}(T)$ is set to $0\,\mathrm{mcps}$ and the upper limit is set to the mean rate of the measurement 5 ($0.378\,\mathrm{mcps}$). This translates to:

$$C_{\mathrm{Rn}}(T) = 0.378\,\mathrm{mcps} \cdot \arctan\left(t1 \cdot \exp\left(\frac{-t2}{R \cdot T}\right) + t3\right) + 0.378\,\mathrm{mcps} \cdot \frac{\pi}{2} \tag{5.20}$$

where t1 to t3 are the parameters optimized by the arctangent fit to the data. The parameter t1 is a

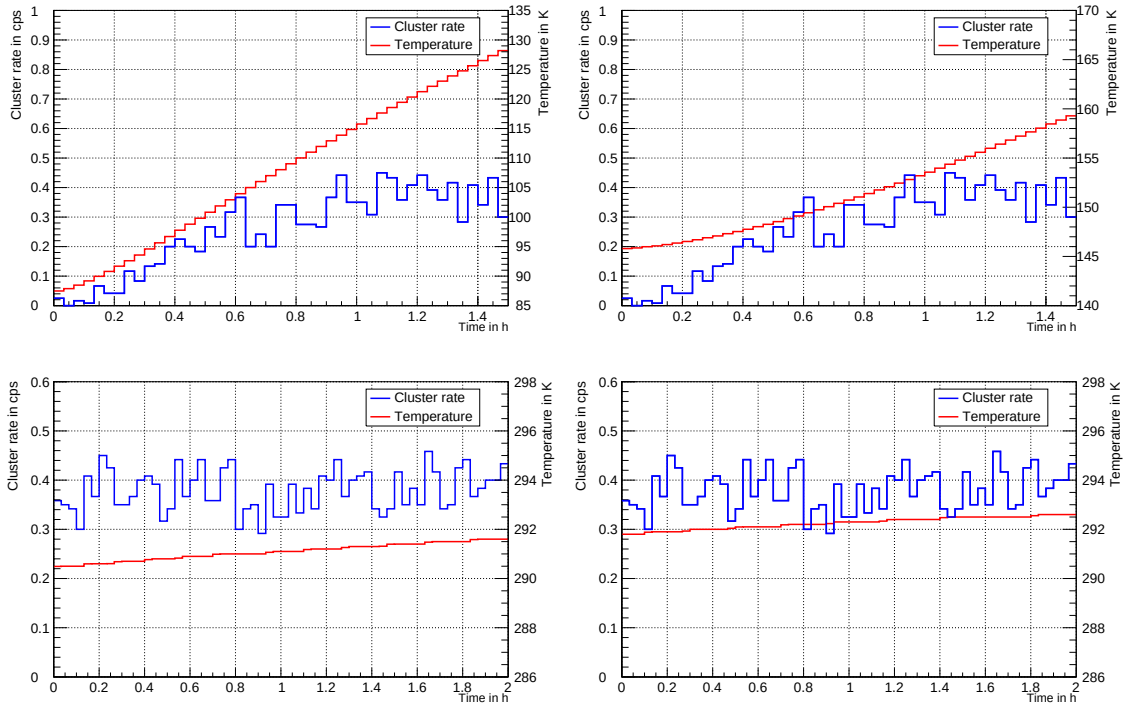

Figure 5.12: **The temperature and rate variations during (measurement 5) and after (measurement 6) the warm-up for the temperature sensors attached to baffle 3.** The temperature (red) and the cluster rate (blue) are plotted. The time bin width is set to 120 s. **Top left:** The temperature of the middle sensor is depicted during the warm-up. **Top right:** The corresponding plot is done for the sensor at the side of the baffle. The timescale on which the data is shown is only 1.5 h since this is the complete time during the warm-up. **Bottom left:** For measurement 6 the data of the sensor in the middle and the cluster rate are plotted. **Bottom right:** The same representation was done for the temperature of the sensor at the side.

superposition of the parameter p0 and the oscillation period τ_0 of (3.6), while t2 is the adsorption enthalpy and t3 is the shift of the arctangent function.

The time width of one bin is set to 120 s for all runs. The obtained temperature and cluster rate are re-binned in a single temperature histogram. The bin width is chosen as 1 K and the uncertainty on the temperature is set to 0.5 K due to the resolution of the bin width (see top graph of figure 5.13).

The large $\chi^2_{\mathrm{red}} = 16.6$ is a clear evidence that the whole set of data does not fit the expectations. A zoom on the temperature range in which the cluster rate changes (85 K to 130 K) reveals the reason (see bottom graph of figure 5.13). Measurements 1 to 4 can be separated by eye by looking for discontinuities in the data. The largest gap is between the data of measurement 4 and the warm-up measurement 5. Clearly, this combination of the data does not give a useful result. An explanation for the observed shifts is that the temperature distribution of the whole baffle is unknown. Only the temperature at its centre can be utilised. The fast cooling processes during cyclic temperature variations do not affect the whole baffle in the same way. Therefore, slower processes are preferred in order to avoid increased temperature gradients at the baffle.

As a next step the data was reduced to measurements 5 and 6 since they include the most valuable and reliable information. Measurement 5 covers the important temperature range (85 K to 130 K) while measurement 6 fixes the maximal cluster rate $C_{\mathrm{Rn,max}}$. They are more reliable since the temperature variation during the warm-up (measurement 5) is quite slow (27 $\frac{\mathrm{K}}{\mathrm{h}}$) and no fast cool-

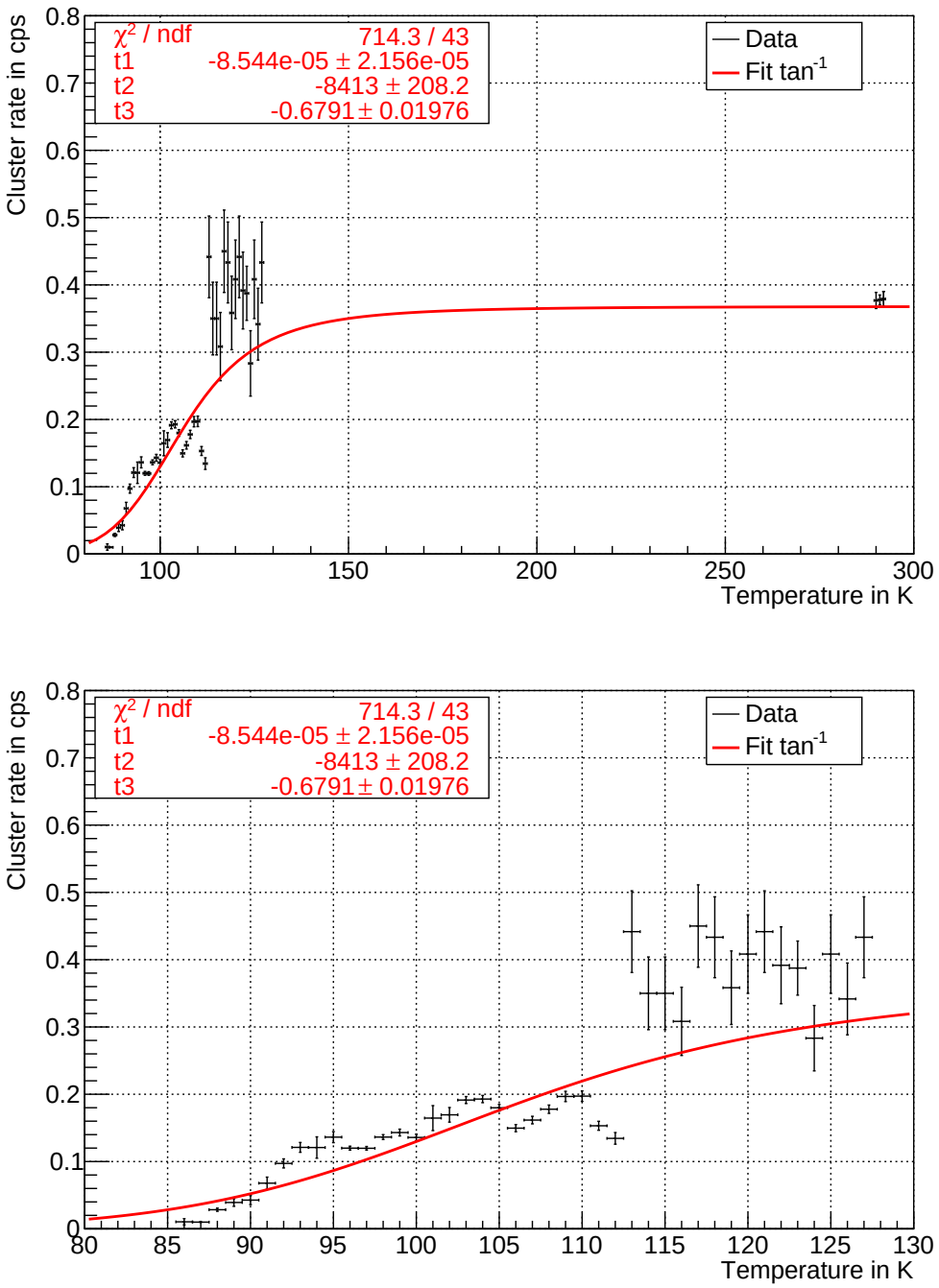

Figure 5.13: **The cluster rate as a function of the temperature of baffle 3 for measurements 1 to 6 summarised in table 5.4.** All measurements are combined and binned in 1 K bins. The uncertainty on the temperature is set to 0.5 K due to the resolution of the binning. Additionally, an arctangent function is fitted to the data. The parameters are depicted in the top left of the graph. **Top:** The whole temperature range is shown. **Bottom:** A zoom on the temperature ranging from 80 K to 130 K is shown.

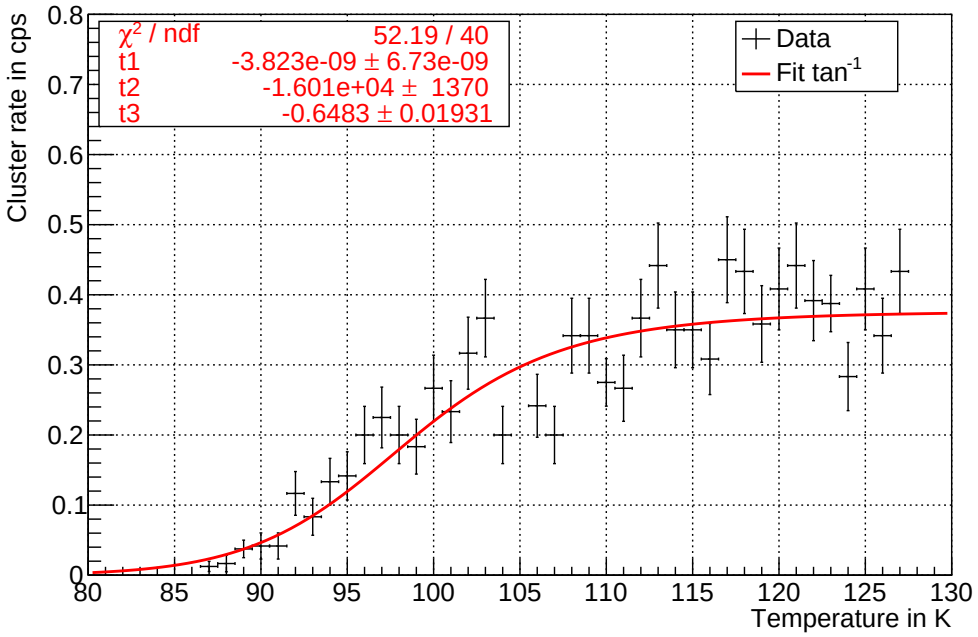

Figure 5.14: **The cluster rate as a function of the temperature of baffle 3 for measurements 5 and 6.** The range is restricted from 80 K to 130 K. Again, an arctangent function is fitted to the data.

down processes occur. In contrast, measurements 3 and 4 have temperature gradients greater than $40\,\frac{\mathrm{K}}{\mathrm{h}}$ during the entire cool-down processes. Measurement 2 has comparable temperature changes as measurement 5, but is excluded due to its cyclic nature and the possibility of the accumulation of a pronounced temperature gradient. The cluster rate as a function of the temperature is plotted in figure 5.14 in the relevant range for the measurements 5 and 6. The reduced chi-squared of $\chi^2_{\mathrm{red}} = 1.3$ is greatly improved by the constraint on these measurements. The change of the cluster rate takes place in a temperature range from 80 K to 120 K.

5.4.4 Translation of the temperature

By comparing the rate and temperature trends of measurements 2 to 4 a translation between these curves is evident. In order to account for this translation a simple time shift of the temperature in time is applied. This approach assumes that the baffle can be described with a single temperature value and that the response of the sensor in the middle of baffle 3 is delayed. Therefore, the deviations of the mean of the rate histogram is subtracted from the scaled deviation of the mean from the temperature histogram. This is used as a measure S for the overlap of the cyclic variations of the two functions:

$$S = \sum_{i=1}^{b_{\max}} \left| (T_i - \bar{T}) \cdot \frac{R_{\max} - R_{\min}}{T_{\max} - T_{\min}} - (R_i - \bar{R}) \right| \tag{5.21}$$

where i is the current time bin, $b_{\max}$ is the amount of bins of the histograms, $T_{\max}$ is the maximal temperature during the measurement, T_i is the temperature in bin i, $T_{\min}$ is the minimal temperature, $\bar{T}$ the mean temperature during the measurement, R_i is the rate in bin i, $R_{\max}$ is the maximal rate, $R_{\min}$ is the minimal rate and $\bar{R}$ is the mean rate.

In order to determine the best delay the temperature rate trend is shifted stepwise by t_{shift}. S is calculated in the range of $t_{\mathrm{shift}} \in [-3600\,\mathrm{s}; 3600\,\mathrm{s}]$ with a step size of 1 s. The dependency of the overlap S on the time translation t_{shift} for measurements 2 to 4 is depicted in figures 5.15 on the

right-hand side. To the left the rate and the temperature trend which is shifted by the best time translation are illustrated. The time shifts with the minimal value for S are $-145\,\mathrm{s}$ for measurement 2, $-255\,\mathrm{s}$ for measurement 3 and $-510\,\mathrm{s}$ for measurement 4. The cluster-rate trend and the temperature trend are in good agreement. One explanation for the decrease in translation from measurements 2 to 4 is the increased mean temperature of each measurement. As a consequence, the difference to liquid-nitrogen temperatures increases. This results in quicker cooling processes, and potentially in higher temperature gradients and the loss of direct relation between the temperature of the sensor and the cluster rate. Furthermore, the half-life of $^{220}\mathrm{Rn}$ is quite long with $55.6\,\mathrm{s}$. This means that cooling processes faster than this timescale are reflected only with a delay since radon which already reached the sensitive main-spectrometer volume decays with a time shift.

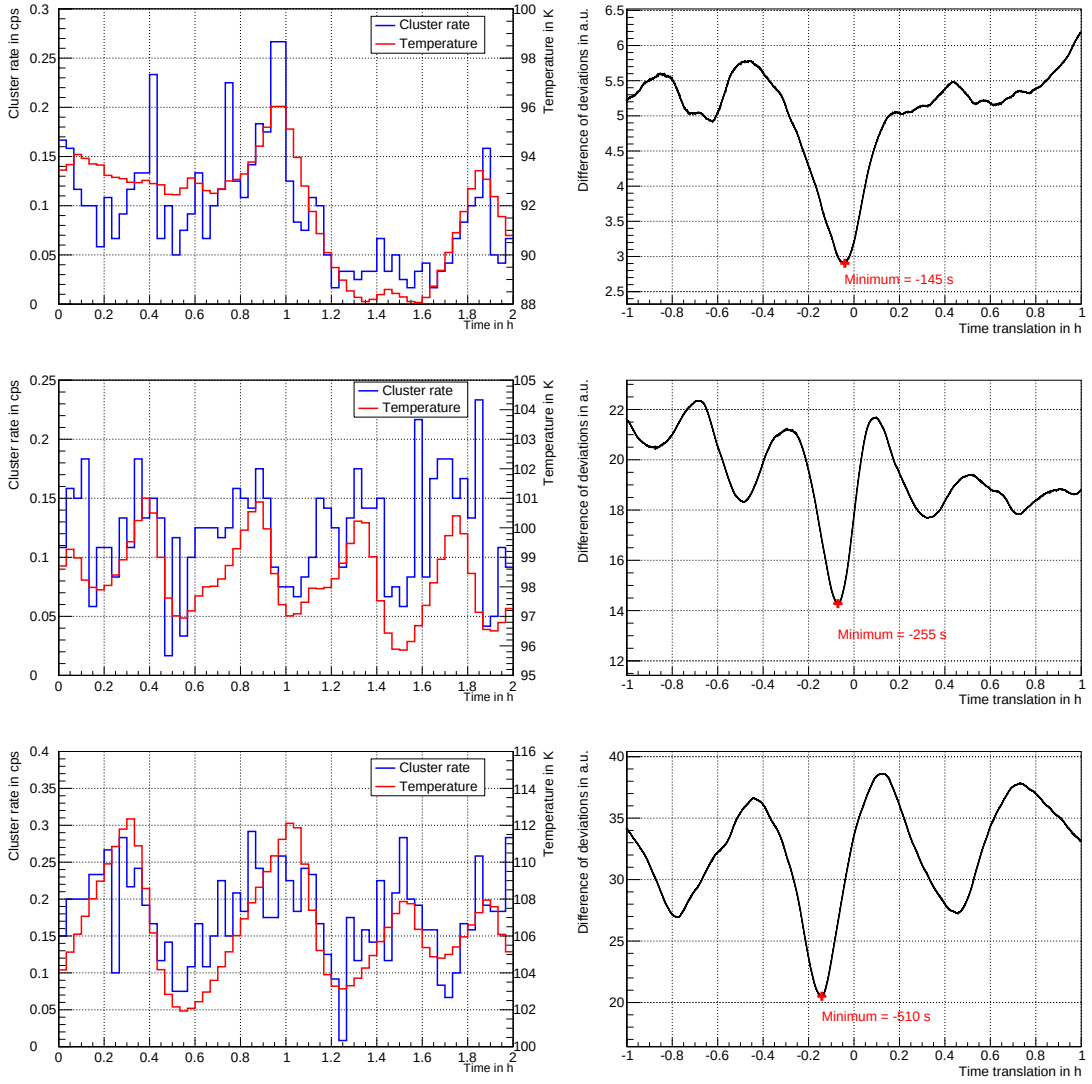

Figure 5.15: **The shifted temperature and rate variations of the measurement 2 to 4 (see table 5.4). Left-hand side:** The temperature (red) is shifted with respect to the cluster rate (blue) to match the trends. **Right-hand side:** The best translation is determined by calculating the difference between the relative deviations of the mean of both the temperature and cluster rate for different time translations of the temperature data. In addition, the minimum of the function is shown (red cross). The resulting graphs for measurement 2 (**top row**), measurement 3 (**middle row**) and measurement 4 (**bottom row**) are shown.

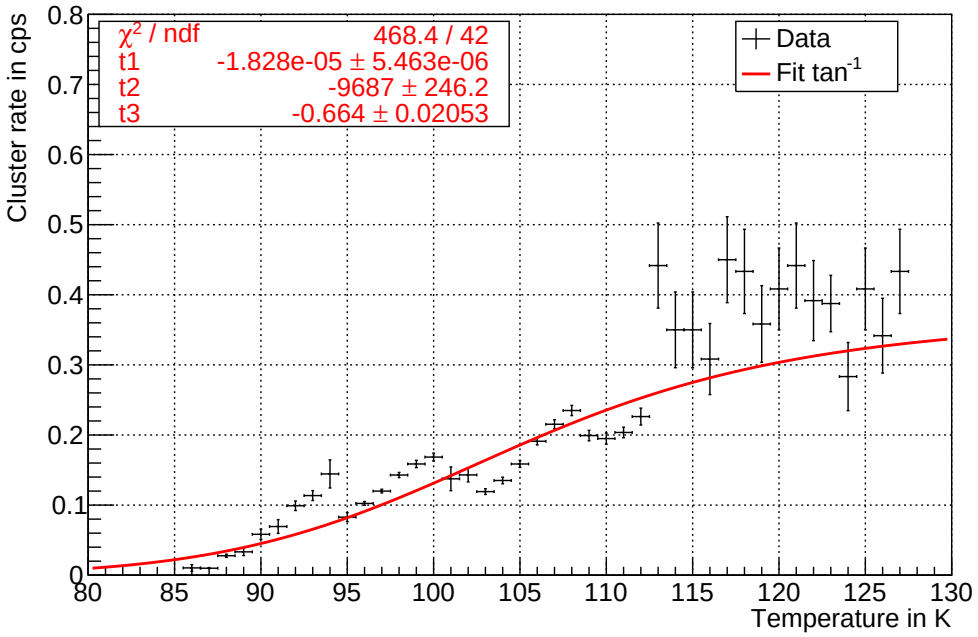

Figure 5.16: **The dependence of the cluster rate on the shifted temperature.** Again, the rate of the clusters is binned with respect to the best shifts obtained in section 5.4.4 (black). The temperature bin width is chosen as 1 K. An arctangent function is fitted to the obtained histogram (red line).

5.4.5 Dependency of the cluster rate on the translated temperature

The shifted temperature trend and the rate trend can be used to check whether the shift of the temperatures with respect to the cluster rate have a significant influence (see figure 5.16). However, the fit does not describe the measurements as signified by the large chi-squared value.

In order to obtain a better idea of the behaviour, results of the measurements 1 to 4 were plotted separately while those from measurements 5 and 6 were combined and fitted with an arctangent function and plotted as a reference (see figure 5.17). Measurements 2 to 4 now have similar slopes, but they are shifted with respect to each other. For increasing mean temperatures the displacement from the arctangent fit to higher temperatures increases. Furthermore, measurement 4 has a strange tail at temperatures above 108 K. This is possibly caused by the delayed response of the sensor in the middle of the baffle since it starts to cool from the bottom close to the liquid-nitrogen inlet. Hence, the temperature in the middle rises while it is already decreasing at the bottom.

The remaining question is why there is an additional shift. The rate determination is robust enough which leaves only an existing displacement of the baffle temperature. The possibility of temperature gradients due to cycling was shortly discussed in section 5.4.4 and is a possible explanation for this shift, too. In order to estimate the uncertainty on the parameters of this arctangent fit, measurements 5 and 6 were combined with measurements 1, 2, 3 and 4 separately. The resulting fit parameters can be used to determine the adsorption enthalpy, and the mean desorption time. First, the oscillation period τ_0 is estimated by using the parameter $p0 = (0.6002 \pm 0.0001)\,\mathrm{s}^{-1}$ from the arctangent fit of figure 4.9 with $\tau_0 = \frac{t1}{p0}$. Then, the mean desorption time can be calculated with (3.6). The fit parameters for these scenarios are summarised in table 5.8. The upper and lower limits contained within the one-sigma intervals are: $\mathrm{t1} \in \left[-9 \cdot 10^{-6}; -9 \cdot 10^{-9}\right]$, $\mathrm{t2} \in \left[-1.8 \cdot 10^{4}\,\frac{\mathrm{J}}{\mathrm{mol\,K}}; -1.18 \cdot 10^{4}\,\frac{\mathrm{J}}{\mathrm{mol\,K}}\right]$ and $\mathrm{t3} \in [-0.67; -0.58]$. As the oscillation period is off from the literature value $\tau_{0,\mathrm{Lit}} \approx 10^{-13}\,\mathrm{s}$ by several orders of magnitude the parameter t1 was restricted to $(1.5 \pm 0.5) \cdot 10^{-13}$ to cover the range predicted by the theory. The resulting fit param-

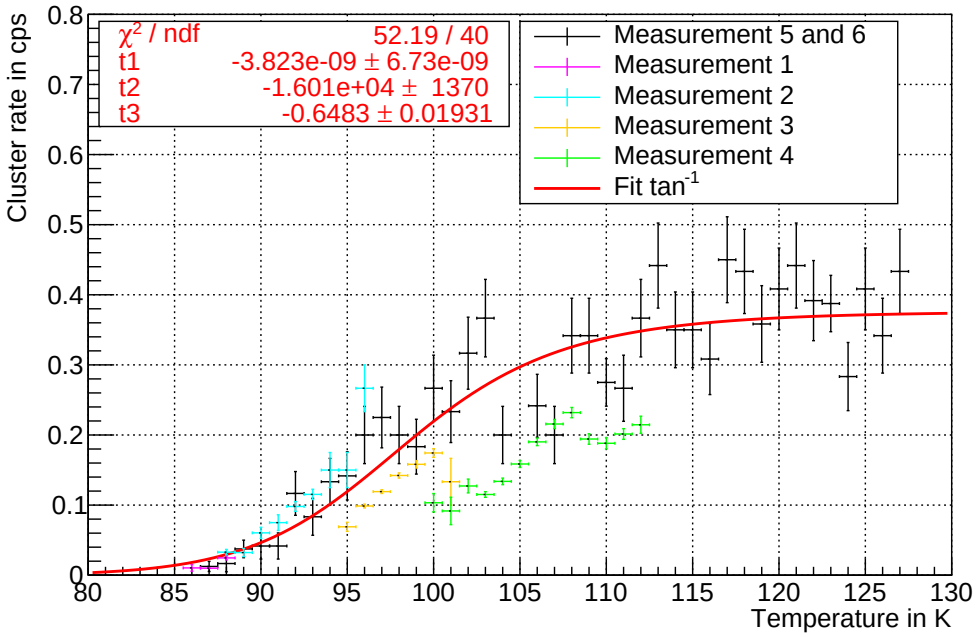

Figure 5.17: **The dependence of the cluster rate on the shifted temperature for all measurements.** Measurements 1 to 4 are plotted separately to gain a better insight into the shifts in-between them. Measurements 5 and 6 (black) are used as input for an arctangent fit (red) in order to be able to compare measurements 1 (magenta), 2 (cyan), 3 (blue) and 4 (orange) with them. In addition, the fit parameters of the arctangent function are shown. They are the same as in figure 5.14 as the used measurements 5 and 6 are unchanged.

eters and the derived parameters are summarised in the bottom part of table 5.8 for measurements 5 and 6 and measurements 2, 5 and 6. Measurement 2 was added since it shows good agreements with the warm-up measurement 5 and increases the statistics in the range of the increase.

Table 5.8: **Summary of the best fit parameters.** The parameters t1, t2 and t3 are summarised for different data samples taken as a basis for the arctangent fit according to (5.20). The parameter t1 contains information about τ_0, t2 is the adsorption enthalpy and t3 is the shift of the arctangent function. The χ^2-value and the degrees of freedom (Dof) give a measure for the goodness of the fit. The values seperated by the second line are obtained with an additional constraint (distinguished by an asterisk): the parameter t1 was set to $-1.5 \cdot 10^{-13}$ and excluded from the fit parameters. The uncertainty is chosen to cover the range of τ_0 indicated by literature. In the last column the corresponding value for the calculated desorption time is shown.

Measure-ments	t1	t2 in $\frac{\mathrm{J}}{\mathrm{mol}}$	t3	χ^2	Dof	τ_{des} in s
1; 5; 6	$(-8 \pm 3) \cdot 10^{-7}$	-12100 ± 300	-0.60 ± 0.02	127.8	43	30 ± 20
2; 5; 6	$(-5 \pm 4) \cdot 10^{-9}$	-17400 ± 600	-0.65 ± 0.02	73.15	49	30 ± 30
3; 5; 6	$(-4 \pm 1) \cdot 10^{-8}$	-14400 ± 200	-0.62 ± 0.02	74.25	47	40 ± 10
4; 5; 6	$(-5 \pm 4) \cdot 10^{-6}$	-11000 ± 600	-0.62 ± 0.02	251.5	53	80 ± 10
5; 6 *	$(-1.5 \pm 0.5) \cdot 10^{-13}$	-23700 ± 100	-0.62 ± 0.02	67.66	41	60 ± 20
2; 5; 6 *	$(-1.5 \pm 0.5) \cdot 10^{-13}$	-23600 ± 100	-0.62 ± 0.02	85.35	50	50 ± 20

5.5 Comparison with simulations and theoretical expectations

The arctangent function according to (5.19) and (5.20) describes the simulations of $^{219}\mathrm{Rn}$ emanating from the NEG material and $^{220}\mathrm{Rn}$ emanating from the main-spectrometer vessel well. This function is used as a fit for the measurements and describes the data reasonably well (e.g. see figure 5.14).

Moreover, the limits on the mean desorption time derived in the previous section 5.4.5 can be cross-checked by using the MOLFLOW model to obtain the suppression efficiencies corresponding to the mean desorption time (section 4.3) and by comparing them to the measurements. The mean desorption time of measurements 5 and 6 with the restraint on the parameter t1 is $\tau_{\mathrm{des}} \in [40\,\mathrm{s}; 80\,\mathrm{s}]$ (see table 5.8). This rather large desorption time implies that for the scenario with only $^{219}\mathrm{Rn}$ emanating from the getter the suppression efficiency is very close to the optimum. The results are summarised in table 5.9. The measurements and the evaluation of the simulation combined with the obtained values for the desorption time show reasonable consistency with the exception of the background measurements with baffles 2 and 3 cold.

The measurements yield an efficiency which is about 7 % lower than the expected one. One possi-

Table 5.9: **Suppression efficiencies derived from the mean desorption time and the simulation compared with the measured efficiencies.** The mean desorption time was chosen to $\tau_{\mathrm{des}} = (60 \pm 20)\,\mathrm{s}$. The simulations for $^{219}\mathrm{Rn}$ emanating from the two sets of NEG strips in pump ports 2 and 3 are used. The simulation values presented in this table assume that there is no other radon source in the main spectrometer.

Measurements	Baffles cold	Suppression efficiency in %	Corresponding simulated efficiency in %
Background	2	71^{+7}_{-10}	66.9 ± 0.5
Background	1; 2	66^{+10}_{-9}	72.4 ± 0.5
Background	2; 3	93^{+3}_{-2}	100.1 ± 0.6
Background	1; 2; 3	97^{+2}_{-3}	100.1 ± 0.6
Radon source	3	98^{+1}_{-2}	98.8 ± 0.6

ble explanation is the existence of an additional unidentified radon source. It is probable that some amount of $^{220}\mathrm{Rn}$ emanates from the main-spectrometer vessel. This effect is most pronounced with baffles 2 and 3 cold since radon from the getters is already suppressed efficiently, and $^{220}\mathrm{Rn}$ is only reduced by roughly $85\,\%$. It is recommended to test whether $^{220}\mathrm{Rn}$ emanating from the main-spectrometer walls is the source for the remaining radon-induced background. An alternative explanation is the low suppression efficiency of baffle 2 in the case in which the radon source is mounted to pump port 2 (see table 5.7).

In addition the simulations do not yet include imperfect adsorption. A particle which hits a surface is always adsorbed in the simulation. However, the chance of adsorption has been estimated to be about $80\,\%$ [Goe14]. This effect introduces an effective decrease of the desorption time which cannot be counteracted completely by cooling the baffles.

The adsorption enthalphy of radon on the copper surface of the baffles is $(-23\,700 \pm 100)\,\frac{\mathrm{J}}{\mathrm{mol\,K}}$ for the combination of measurements 5 and 6 with the constraint on parameter t1. It is in good agreement with the scenario of an oxidised baffle surface (see table 3.1). Surprisingly, the adsorption enthalpy of baffle 3 seems not to be dominated by ice on the surface although the main spectrometer was not baked out for the SDS-II commissioning phase. One reason might be that this baffle was cooled when the baffle 2 was already cold before the measurements with an additional radon source took place. Therefore, most of the water was frozen on baffle 2.

5.6 Conclusion

The radon-induced background is studied by measuring the background rate at elevated pressures in the main spectrometer ($1 \cdot 10^{-8}\,\mathrm{mbar}$) and by searching for five or more correlated events ($N \geq 5$) occurring within $\Delta t \leq 0.2\,\mathrm{s}$ to the proximate event.

It is confirmed that liquid-nitrogen cooled copper baffles installed between the sensitive main-spectrometer volume and the pump ports suppress the radon-induced background efficiently. In the scenario with three cold baffles the suppression efficiency is $97^{+2}_{-3}\,\%$. This results in a remaining radon-induced background rate of $(27 \pm 3)\,\mathrm{mcps}$. This is still a factor of 3 too high for the ambitious KATRIN background limit of $10\,\mathrm{mcps}$. At elevated pressures the remaining background which is not induced by radon α-decays is $(564 \pm 2)\,\mathrm{mcps}$. The suppression of the radon-induced background has revealed an additional background component which is not induced by high-energetic stored electrons.

Furthermore, it is shown that the cool-down of baffles 2 and 3 yields a suppression efficiency of $93^{+3}_{-2}\,\%$ which is greater than the efficiency of $66^{+10}_{-9}\,\%$ obtained from measurements with baffles 1 and 2 cold. It is deduced that the NEG strips are the dominant radon source in the main spectrometer.

In addition, the dependency of the radon-induced background on the temperature of the baffles is studied. It is indicated that the refilling of the liquid-nitrogen supply tank leads to a significant temperature variation of the baffle system. This fact may necessitate to exclude a time-period of about $4\,\mathrm{h}$ after the refill from the data analysis for neutrino mass measurements with the current setup.

The utilisation of an additional radon source allows to obtain measurements with high statistics. This enables to study the temperature dependency of baffle 3 in detail. The observed trend matches the shape observed for simulations (see section 4). It is implied that the mean desorption time of radon from the copper baffle surface is $\tau_{\mathrm{des}} \in [40\,\mathrm{s}; 80\,\mathrm{s}]$. By taking the performed simulations into account it is shown that this yields an almost full suppression efficiency for $^{219}\mathrm{Rn}$ emanating from the NEG strips mounted in pump ports 2 and 3. The measurements indicate slightly lower suppression efficiencies. All in all, both methods are in good agreement and show consistent results.

The measured baffle temperature is delayed in time during measurements with elevated temperatures when compared to the cluster rate. This effect is much more pronounced with higher temperature variations. This indicates that it is reasonable to take data with increased statistics at different temperatures with a low variation. For the KATRIN standard operation, it is essential to operate the baffle system at the lowest possible temperature and under stable conditions.

It is recommended to describe the data by a model including both $^{219}\mathrm{Rn}$ originating from the NEG strips and $^{220}\mathrm{Rn}$ emanating from the main-spectrometer vessel. By leaving the relative number of radon atoms inside the vessel volume as a free parameter, it can be tested whether $^{220}\mathrm{Rn}$ emanating from the main spectrometer vessel is a significant source of background in the main spectrometer.

6. Summary and outlook

The observation of neutrino oscillations requires neutrinos to be massive particles. Their mass impacts models describing the structure formation of the universe and other cosmological models. Therefore, it is important to determine the neutrino mass. However, neutrino oscillation experiments are not sensitive to the absolute neutrino mass-scale, so that dedicated experiments are required. The most promising method to determine the neutrino mass in a direct and model-independent way is the utilisation of high-precision β-spectroscopy. With this method, the most stringent limits are reached by the Mainz and Troitsk tritium experiments which utilised the MAC-E filter principle yielding an upper limit of $m_{\bar{\nu}_e} < 2\,\mathrm{eV/c^2}$.

The KATRIN experiment utilises this successful technique with an active MAC-E filter: The main spectrometer with a length of $23.3\,\mathrm{m}$ and a diameter of $10\,\mathrm{m}$ analyses the energy of the tritium β-decay electrons under ultra-high vacuum conditions ($10^{-11}\,\mathrm{mbar}$) while a segmented silicon detector connected to its downstream end counts the amount of transmitted electrons within a defined region of interest. It is designed to improve the sensitivity by a factor of 10 to $m_{\bar{\nu}_e} < 0.2\,\mathrm{eV/c^2}$ ($90\,\%$ C.L.). In order to reach this ambitious goal the background in the energy region of interest needs to be lower than $10\,\mathrm{mcps}$. The identified background consists of the intrinsic detector background, background due to residual-gas ionisation and background due to radioactive decays. Previous investigations have shown that electrons accompanying the α-decay of radon are stored in the spectrometer and create secondary electrons. Since radon is volatile and neutral it can desorb from a surface and propagate freely through the spectrometer before decaying. Therefore, it is a dominant source of background. It is known that the porous non-evaporable getter (NEG) strips currently mounted in pump ports 2 and 3 of the KATRIN main spectrometer emanate $^{219}\mathrm{Rn}$. However, these strips are required to achieve the excellent vacuum conditions in the experiment. In addition it is possible that welds of the main-spectrometer vessel emanate $^{220}\mathrm{Rn}$. As a passive reduction method liquid-nitrogen cooled copper baffles are installed in each of the three pump ports. Radon atoms cryosorb onto the cold surface and remain there until they either decay or desorb. For sufficiently long desorption times this setup efficiently reduces the amount of radon decaying in the sensitive main-spectrometer volume. As the desorption time is negatively correlated with the temperature of the baffles the functionality of the liquid-nitrogen supply system is important.

In the scope of this thesis the insulators of the high-voltage separators for the liquid-nitrogen supply system were tested thoroughly and implemented successfully for retarding potentials of $-18.6\,\mathrm{kV}$. This allows continuous high-voltage measurements with the baffle system operating at liquid-nitrogen temperatures. Due to this essential improvement not only this passive reduction technique is prepared for the neutrino-mass measurement, but the radon-induced background can

be studied in detail as well. Furthermore, the other background components can be investigated without having to accommodate radon-induced backgrounds while all three baffles are cold.

In order to calculate the expected suppression efficiency of radon-induced backgrounds by cryosorption onto the baffle surfaces the Simplified Model was used, which neglects desorptions. In order to determine the temperature dependence of the suppression efficiency the Numerical Model was created which expands the Simplified Model by including re-desorptions from the baffles. This model is restricted to radon emanating from the main-spectrometer vessel. Lastly, it is necessary to simulate radon sources at arbitrary positions to determine the simulation result which describes the observations best. This is possible with test-particle Monte-Carlo simulations based on a modified MOLFLOW+ version.

All simulations were compared and are in good agreement. It was shown that the deviations of the suppression efficiencies at the limits of the desorption time are small. Moreover, the dependence of the suppression efficiency on the mean desorption time based on the Numerical Model and the MOLFLOW+ simulations have the same shape. The shape is well described by an arctangent function for those scenarios for which $^{219}\mathrm{Rn}$ emanates from the NEG strips and $^{220}\mathrm{Rn}$ emanates from the main-spectrometer vessel. However, there is a shift of the suppression-efficiency trend to lower desorption times when comparing the Numerical Model with the MOLFLOW+ simulations. This can probably be negated by including a geometry factor into the Numerical Model which accommodates the shape of the baffle. All in all, the modified MOLFLOW+ version is best suited to simulate the suppression of radon-induced decays by the liquid-nitrogen cooled copper baffles since it is the most complete model and includes the most specific geometry.

The completion of the high-voltage separators allows to keep the baffles continuously at liquid-nitrogen temperatures for high-voltage measurements. During the second commissioning phase of the spectrometer and detector section (SDS) background measurements at elevated pressure in the main spectrometer ($10^{-8}\,\mathrm{mbar}$) were performed. The radon-induced background can be separated by searching for $N \geq 5$ correlated events which occur within $\Delta t \leq 0.2\,\mathrm{s}$ of the proximate event.

The best suppression efficiency with two getter pumps located in pump ports 2 and 3 and three cold baffles was determined to be $97^{+2}_{-3}\,\%$. Furthermore, the remaining radon-induced background is $(27 \pm 3)\,\mathrm{mcps}$ which is still above the design limit of $10\,\mathrm{mcps}$. Moreover, at elevated pressure the remaining background which is not induced by radon α-decays is $(564 \pm 2)\,\mathrm{mcps}$. Since the liquid-nitrogen supply system is fully operational it is possible to study this background without having to accommodate radon. Up to date the source of the remaining background has not been identified unambiguously.

The measurements with cold baffles in pump ports 2 and 3 show a lower radon-induced background than the measurements with cold baffles in pump port 1 and 2. It was concluded that the main source of radon are the NEG strips.

In order to study the temperature dependence of the suppression efficiency an additional $^{220}\mathrm{Rn}$ source was connected to pump port 3 and the temperature of baffle 3 was varied. It was shown that an arctangent function describes the measurements during the warm-up as it is predicted by the simulations. Based on fits of the arctangent function and the simulations the mean desorption time of radon from the copper baffle was estimated to be $(60 \pm 20)\,\mathrm{s}$. By combining these values with the simulations, the suppression efficiencies can be calculated and compared to the measurements. All in all, the results are in good agreement. Some tension remains for measurements with cold baffles 2 and 3. This might be an indication that the remaining radon-induced background is caused by $^{220}\mathrm{Rn}$ emanating from the main-spectrometer vessel.

Additional measurements at elevated temperatures exhibit a time shift between the cluster rate trend and the temperature trend. Even after a correction of the translation the measurements at elevated pressure do not match. It is recommended for further studies in the future to avoid large temperature fluctuations.

During the measurement with an additional radon source and three cold baffles the liquid-nitrogen supply vessel was refilled. This led to fluctuations of the temperatures of all baffles which is reflected in an increase of the observed cluster rate by a factor of two. Further studies need to validate whether these temperature variations influence the background induced by radon decays as pronouncedly as for the $^{220}\mathrm{Rn}$ source. In the worst case, this necessitates the exclusion of a 4-hour measurement-time interval after each refill of the liquid-nitrogen supply.

Further research is required to determine whether there is a component of $^{220}\mathrm{Rn}$ emanating from the main-spectrometer vessel. Also, the influence of accidental events on the background rates needs to be studied. In addition, it is necessary to determine the nature of the remaining background. The liquid-nitrogen cooled copper baffles will help to facilitate the analysis as the remaining radon-induced background is lower by a factor of 20 than the remaining unidentified background when the baffles are operated at liquid-nitrogen temperatures.

Once the unidentified background is eliminated the remaining radon-induced background will become problematic again since it is already larger than the design specification. Therefore, improvements to the liquid-nitrogen cooled copper baffles, its supply system and additional active reduction methods need to be considered. A simple improvement of the liquid-nitrogen supply system is an exchange of the weakly thermally-coupled temperature sensors. Moreover, further sensors could be added to measure the temperature profile of each baffle and, thus, improve its homogeneous cooling. One more fundamental and expensive change of the system is the implementation of an abrasive surface onto the baffles (i.e. porous ceramics) to increase the surface at which radon is effectively cryosorbed. Another possibility is the utilisation of a cooling system based on liquid helium instead of liquid nitrogen to decrease the temperature of the baffles. However, due to the worldwide shortage of helium, this might be difficult to realise from the technical point of view since a complex recovery system is required. Possible active reduction methods such as electron-cyclotron resonance, a static and a pulsed dipole or magnetic pulses are considered in the KATRIN collaboration.

Bibliography

[Ade14a] P. Ade et al., "Planck 2013 results. I. Overview of products and scientific results," *Astronomy & Astrophysics*, vol. 571, p. A1, 2014.

[Ade14b] P. Ade, et al., "Planck 2013 results. XVII. Gravitational lensing by large-scale structure," *Astronomy & Astrophysics*, vol. 571, p. A17, 2014.

[Ade14c] P. Ade et al., "Planck 2013 results. XXIX. The Planck catalogue of Sunyaev-Zeldovich sources," *Astronomy & Astrophysics*, vol. 571, p. A29, 2014.

[AF11] S. Agarwal and H. A. Feldman, "The effect of massive neutrinos on the matter power spectrum," *Monthly Notices of the Royal Astronomical Society*, vol. 410, no. 3, pp. 1647–1654, 2011.

[Ago13] M. Agostini et al., "Results on Neutrinoless Double-β Decay of Ge 76 from Phase I of the GERDA Experiment," *Physical Review Letters*, vol. 111, no. 12, p. 122503, 2013.

[AH38] N. Arley and W. Heitler, "Neutral particles in cosmic radiation," *Nature*, vol. 142, no. 1.58, 1938.

[Ale87] E. N. Alexeyev, L. N. Alekseeva, V. I. Volchenko, and I. V. Krivosheina, "Possible detection of a neutrino signal on 23 February 1987 at the Baksan underground scintillation telescope of the Institute of Nuclear Research," *JETP lett*, vol. 45, no. 589, pp. 247–248, 1987.

[Ale88] E. N. Alexeyev, L. N. Alexeyeva, I. V. Krivosheina and V. I. Volchenko, "Detection of the neutrino signal from SN 1987A in the LMC using the INR Baksan underground scintillation telescope," *Physics Letters B*, vol. 205, no. 2-3, pp. 209 – 214, 1988. [Online]. Available: http://www.sciencedirect.com/science/article/pii/0370269388916516

[ALE06] ALEPH Collaboration, the DELPHI Collaboration, the L3 Collaboration, the OPAL Collaboration and the SLD Collaboration, "Precision electroweak measurements on the Z resonance," *Physics Reports*, vol. 427, no. 5-6, pp. 257–454, 2006. [Online]. Available: http://www.sciencedirect.com/science/article/pii/S0370157305005119

[And63] P. W. Anderson, "Plasmons, gauge invariance, and mass," *Phys. Rev.*, vol. 130, pp. 439–442, Apr 1963. [Online]. Available: http://link.aps.org/doi/10.1103/PhysRev.130.439

[And12] L. Anderson et al., "The clustering of galaxies in the SDSS-III Baryon Oscillation Spectroscopic Survey: baryon acoustic oscillations in the Data Release 9 spectroscopic galaxy sample," *Monthly Notices of the Royal Astronomical Society*, vol. 427, no. 4, pp. 3435–3467, 2012.

[Ark01] N. Arkani-Hamed, S. Dimopoulos, G. Dvali and J. March-Russell, "Neutrino masses from large extra dimensions," *Phys. Rev. D*, vol. 65, p. 024032, Dec 2001. [Online]. Available: http://link.aps.org/doi/10.1103/PhysRevD.65.024032

[Ase11] V. Aseev, A. I. Belesev, A. I. Berlev, E. V. Geraskin, A. A. Golubev, N. A. Likhovid, V. M. Lobashev, A. A. Nozik, V. S. Pantuev, V. I. Parfenov, A. K. Skasyrskaya, F. V. Tkachov and S. V. Zadorozhny, "Upper limit on the electron antineutrino mass from the troitsk experiment," *Phys. Rev. D*, vol. 84, p. 112003, Dec 2011. [Online]. Available: http://link.aps.org/doi/10.1103/PhysRevD.84.112003

[Aug23] M. P. Auger, "Sur les rayons β^- secondaires produits dans un gaz par des rayons X," *Comptes rendus hebdomadaires des séances de l'Académie des sciences, Paris*, vol. 177, pp. 169–171, 1923. [Online]. Available: http://gallica.bnf.fr/ark:/12148/bpt6k3130n.image.f187.langFR

[Bab12] M. Babutzka et al., "Monitoring of the operating parameters of the KATRIN Windowless Gaseous Tritium Source," *New Journal of Physics*, vol. 14, no. 10, p. 103046, 2012.

[Bah63] J. N. Bahcall, W. A. Fowler, I. Iben Jr and R. L. Sears, "Solar neutrino flux." *The Astrophysical Journal*, vol. 137, pp. 344–346, 1963.

[Bah95] J. N. Bahcall and M. H. Pinsonneault and G. J. Wasserburg, "Solar models with helium and heavy-element diffusion," *Reviews of Modern Physics*, vol. 67, no. 4, p. 781, 1995.

[Bar14] J. Barrett et al., "Results of the first KATRIN SDS measurement phase," internal KATRIN document, 2014.

[Bas09] M. Basunia, "Nuclear Data Sheets for A = 187," *Nuclear Data Sheets*, vol. 110, no. 5, pp. 999 – 1238, 2009. [Online]. Available: http://www.sciencedirect.com/science/article/pii/S0090375209000301

[BC95] C. Benvenuti and P. Chiggiato, "Pumping characteristics of the St707 non-evaporable sgetter (Zr 70-V 24.6-Fe 5.4 wt%)," *J. Vac. Sci. Technol. A*, vol. 14, no. CERN-MT-95-10-SM, pp. 3278–3282. 18 p, Oct 1995. [Online]. Available: https://cds.cern.ch/record/292373

[BD76] J. N. Bahcall and R. Davis, "Solar Neutrinos - a Scientific Puzzle," *Science*, vol. 191, pp. 264–267, 1976. [Online]. Available: http://www.bnl.gov/bnlweb/raydavis/Science-01-23-76.pdf

[Bec00] A. H. Becquerel, "Sur la dispersion du rayonnement du radium dans un champ magnétique," *Comptes rendus de l'Académie des sciences, Paris*, vol. 130, pp. 372–376, 1900.

[Bel03] E. Bellotti, *Neutrino physics*. Ios Press, 2003, vol. 152.

[Ben13] C. Bennett et al., "Nine-year Wilkinson Microwave Anisotropy Probe (WMAP) observations: final maps and results," *The Astrophysical Journal Supplement Series*, vol. 208, no. 2, p. 20, 2013.

[Ber12] J. Beringer et al., "Status of higgs boson physics," *Phys. Rev. D*, vol. 86, p. 010001, 2012, Particle Data Group. [Online]. Available: http://pdg.lbl.gov

[Beu11] F. Beutler, C. Blake, M. Colless, D.H. Jones, L. Staveley-Smith, L. Campbell, Q. Parker, W. Saundersfbahcall and F. Watson, "The 6dF Galaxy Survey: baryon acoustic oscillations and the local Hubble constant," *Monthly Notices of the Royal Astronomical Society*, vol. 416, no. 4, pp. 3017–3032, 2011.

[Bio87] R. M. Bionta et al., "Observation of a neutrino burst in coincidence with supernova 1987a in the large magellanic cloud," *Phys. Rev. Lett.*, vol. 58, pp. 1494–1496, Apr 1987. [Online]. Available: http://link.aps.org/doi/10.1103/PhysRevLett.58.1494

[Bla12] C. Blake et al., "The wigglez dark energy survey: Joint measurements of the expansion and growth history at z < 1," *Monthly Notices of the Royal Astronomical Society*, vol. 425, no. 1, pp. 405–414, 2012.

[BM14] R. A. Battye and A. Moss, "Evidence for massive neutrinos from cosmic microwave background and lensing observations," *Phys. Rev. Lett.*, vol. 112, p. 051303, Feb 2014. [Online]. Available: http://link.aps.org/doi/10.1103/PhysRevLett.112.051303

[Bor05] L. Bornschein, "The KATRIN experiment - a direct measurement of the electron antineutrino mass in the sub-eV region," *Nuclear Physics A*, vol. 752, no. 0, pp. 14 – 23, 2005, proceedings of the 22nd International Nuclear Physics Conference (Part 2). [Online]. Available: http://www.sciencedirect.com/science/article/pii/S0375947405001478

[Bor08] B. Bornschein, "Determination of neutrino mass from tritium beta decay," *Fusion Science and Technology*, vol. 54, no. 1, pp. 59–66, 2008.

[BP34] H. Bethe and R. Peierls, "The "neutrino"," *Nature*, vol. 133, no. 3362, p. 532, 1934.

[Bra88] C. B. Bratton et al., "Angular distribution of events from SN1987A," *Phys. Rev. D*, vol. 37, pp. 3361–3363, Jun 1988. [Online]. Available: http://link.aps.org/doi/10.1103/PhysRevD.37.3361

[Bro01] E. Browne, "Nuclear Data Sheets for A = 215,219,223,227,231," *Nuclear Data Sheets*, vol. 93, no. 4, pp. 763–10 610, 2001. [Online]. Available: http://www.sciencedirect.com/science/article/pii/S009037520190016X

[Cap14] F. Capozzi, G. L. Fogli, E. Lisi, A. Marrone, D. Montanino and A. Palazzo, "Status of three-neutrino oscillation parameters, circa 2013," *Phys. Rev.*, vol. D89, no. 9, p. 093018, 2014.

[Cas00] J. A. Casas,J. R. Espinosa, A. Ibarra,and I. Navarro, "Nearly degenerate neutrinos, supersymmetry and radiative corrections," *Nuclear Physics B*, vol. 569, no. 1, pp. 82–106, 2000. [Online]. Available: http://www.sciencedirect.com/science/article/pii/S0550321399006057

[CER15] CERN, "Molflow+ A Monte-Carlo Simulator package developed at CERN," May 2015.

[Cha14] J. Chadwick, "Intensitaetsverteilung im magnetischen Spektren der β-Strahlen von Radium B + C," *Verhandlungen der Deutschen Physikalischen Gesellschaft*, vol. 16, pp. 383 – 391, 1914.

[CK35] D. Coster and R. D. L. Kronig, "New type of Auger effect and its influence on the X-ray spectrum," *Physica*, vol. 2, no. 1 - 12, pp. 13–24, 1935. [Online]. Available: http://www.sciencedirect.com/science/article/pii/S003189143590060X

[Cle98] B. T. Cleveland, T. Daily, R. Davis Jr, J. R. Distel, K. Lande, C. K. Lee, P. S. Wildenhain and J. Ullman, "Measurement of the Solar Electron Neutrino Flux with the Homestake Chlorine Detector," *The Astrophysical Journal*, vol. 496, no. 1, p. 505, 1998. [Online]. Available: http://stacks.iop.org/0004-637X/496/i=1/a=505

[Dan62] G. Danby, J.-M. Gaillard, K. Goulianos, L. M. Lederman, N. Mistry, M. Schwartz and J. Steinberger, "Observation of high-energy neutrino reactions and the existence of two kinds of neutrinos," *Phys. Rev. Lett.*, vol. 9, pp. 36–44, Jul 1962. [Online]. Available: http://link.aps.org/doi/10.1103/PhysRevLett.9.36

[Dav79] R. Davis Jr, J. C. Evans and B. T. Cleveland, "The solar neutrino problem," in *Long-Distance Neutrino Detection-1978: CL Cowan Memorial Symposium, Catholic University*, vol. 52, no. 1. AIP Publishing, 1979, pp. 17–27.

[DHH68] R. Davis, D. S. Harmer, and K. C. Hoffman, "Search for neutrinos from the sun," *Phys. Rev. Lett.*, vol. 20, pp. 1205–1209, May 1968. [Online]. Available: http://link.aps.org/doi/10.1103/PhysRevLett.20.1205

[Dre13] G. Drexlin, V. Hannen, S. Mertens and C. Weinheimer, "Current direct neutrino mass experiments," *Advances in High Energy Physics*, vol. 2013, 2013.

[Dyc93] R. S. V. Dyck, D. L. Farnham and P. B. Schwinberg, "Tritium–helium-3 mass difference using the Penning trap mass spectroscopy," *Phys. Rev. Lett.*, vol. 70, pp. 2888–2891, May 1993. [Online]. Available: http://link.aps.org/doi/10.1103/PhysRevLett.70.2888

[EB64] F. Englert and R. Brout, "Broken symmetry and the mass of gauge vector mesons," *Phys. Rev. Lett.*, vol. 13, pp. 321–323, Aug 1964. [Online]. Available: http://link.aps.org/doi/10.1103/PhysRevLett.13.321

[Eic08] F. Eichelhardt, B. Bornschein, L. Bornschein, O. Kazachenko, N. Kernert and M. Sturm, "First tritium results of the KATRIN test experiment TRAP," *Fusion Science and Technology*, vol. 54, no. 2, pp. 615–618, 2008.

[EK00] B. Eichler and J. V. Kratz, "Electrochemical deposition of carrier-free radionuclides," *Radiochimica Acta International journal for chemical aspects of nuclear science and technology*, vol. 88, no. 8/2000, p. 475, 2000.

[Elg02] O. Elgarøy et al., "New upper limit on the total neutrino mass from the 2 degree field galaxy redshift survey," *Phys. Rev. Lett.*, vol. 89, p. 061301, Jul 2002. [Online]. Available: http://link.aps.org/doi/10.1103/PhysRevLett.89.061301

[Eng12] A. V. Engelen et al., "A measurement of gravitational lensing of the microwave background using south pole telescope data," *The Astrophysical Journal*, vol. 756, no. 2, p. 142, 2012. [Online]. Available: http://stacks.iop.org/0004-637X/756/i=2/a=142

[ES02] R. Eichler and M. Schädel, "Adsorption of radon on metal surfaces: a model study for chemical investigations of elements 112 and 114," *The Journal of Physical Chemistry B*, vol. 106, no. 21, pp. 5413–5420, 2002.

[EV02] S. R. Elliott and P. Vogel, "Double beta decay," *Ann. Rev. Nucl. Part. Sci.*, vol. 52, pp. 115–151, 2002.

[EZG00] B. Eichler, H. Zimmermann, and H. Gäggeler, "Adsorption of radon on ice surfaces," *The Journal of Physical Chemistry A*, vol. 104, no. 14, pp. 3126–3131, 2000.

[Faj13] K. Fajans, "Radioactive transformations and the periodic system of the elements," *Berichte der Deutschen Chemischen Gesellschaft*, vol. 46, pp. 422–439, 1913.

[Fer34] E. Fermi, "Versuch einer Theorie der β-Strahlen I," *Zeitschrift fuer Physik*, vol. 88, no. 3-4, pp. 161–177, 1934. [Online]. Available: http://dx.doi.org/10.1007/BF01351864

[Fer46] E. Fermi, "The development of the first chain reaction pile," *Proceedings of the American Philosophical Society*, vol. 90, no. 1, pp. 20 – 24, January 1946. [Online]. Available: http://www.jstor.org/stable/3301034

[FGM58] R. P. Feynman and M. Gell-Mann, "Theory of the fermi interaction," *Physical Review*, vol. 109, no. 1, p. 193, 1958.

[Fis14] S. Fischer, "Commissioning of the KATRIN Raman system and durability studies of optical coatings in glove box and tritium atmospheres," Ph.D. dissertation, Karlsruhe, Karlsruher Institut fuer Technologie (KIT), July 2014.

[Fra10] F. Fraenkle, "Background Investigations of the KATRIN Pre-Spectrometer," Ph.D. dissertation, Karlsruhe, Karlsruher Institut fuer Technologie (KIT), July 2010.

[Fra11] F. Fraenkle, L. Bornschein, G. Drexlin, F. Glueck, S. Goerhardt, W. Kaefer, S. Mertens, N. Wandkowsky and J. Wolf, "Radon induced background processes in the KATRIN pre-spectrometer," *Astroparticle Physics*, vol. 35, no. 3, pp. 128–134, 2011.

[Fra14] F. M. Fraenkle et al., "Penning discharge in the katrin pre-spectrometer," *Journal of Instrumentation*, vol. 9, no. 07, p. P07028, 2014.

[Fre75] M. S. Freedman, "Ionization by Nuclear Transitions," Conference: Summer course in atomic physics, Carry-le-Rouet, France, 31 Aug 1975; Other Information: Orig. Receipt Date: 30-JUN-76, January 1975.

[Fuk98a] Y. Fukuda et al., "Evidence for oscillation of atmospheric neutrinos," *Phys. Rev. Lett.*, vol. 81, pp. 1562–1567, Aug 1998. [Online]. Available: http://link.aps.org/doi/10.1103/PhysRevLett.81.1562

[Fuk98b] Y. Fukuda et al., "Measurements of the Solar Neutrino Flux from Super-Kamiokande's First 300 Days," *Phys. Rev. Lett.*, vol. 81, pp. 1158–1162, Aug 1998. [Online]. Available: http://link.aps.org/doi/10.1103/PhysRevLett.81.1158

[Fur39] W. Furry, "On transition probabilities in double beta-disintegration," *Physical Review*, vol. 56, no. 12, p. 1184, 1939.

[Gal00] M. Galeazzi, F. Fontanelli, F. Gatti and S. Vitale, "End-point energy and half-life of the 187 re β decay," *Physical Review C*, vol. 63, no. 1, p. 014302, 2000.

[Gan13] A. Gando et al., "Limit on Neutrinoless $\beta\beta$ Decay of ^{136}Xe from the First Phase of KamLAND-Zen and Comparison with the Positive Claim in ^{76}Ge," *Phys. Rev. Lett.*, vol. 110, p. 062502, Feb 2013. [Online]. Available: http://link.aps.org/doi/10.1103/PhysRevLett.110.062502

[Gas14] L. Gastaldo et al., "The Electron Capture ^{163}Ho Experiment ECHos," *Journal of Low Temperature Physics*, vol. 176, no. 5-6, pp. 876–884, 2014. [Online]. Available: http://dx.doi.org/10.1007/s10909-014-1187-4

[GM35] M. Goeppert-Mayer, "Double beta-disintegration," *Phys. Rev.*, vol. 48, pp. 512–516, Sep 1935. [Online]. Available: http://link.aps.org/doi/10.1103/PhysRev.48.512

[Goe12] S. Goerhardt, "Reduktion der durch Radon induzierten Untergrundprozesse in den KATRIN Spektrometern," Master's thesis, Karlsruhe, Karlsruher Institut fuer Technologie (KIT), October 2012.

[Goe14] S. Goerhardt, "Background Reduction Methods and Vacuum Technology at the KATRIN Spectrometers," Ph.D. dissertation, Karlsruhe, Karlsruher Institut fuer Technologie (KIT), January 2014.

[Gol58] M. Goldhaber, L. Grodzins and A. W. Sunyar, "Helicity of neutrinos," *Phys. Rev.*, vol. 109, pp. 1015–1017, Feb 1958. [Online]. Available: http://link.aps.org/doi/10.1103/PhysRev.109.1015

[Gro09] S. Grohmann, "Stability analyses of the beam tube cooling system in the KATRIN source cryostat," *Cryogenics*, vol. 49, no. 8, pp. 413 – 420, 2009. [Online]. Available: http://www.sciencedirect.com/science/article/pii/S0011227509000952

[Gur64] G. S. Guralnik, C. R. Hagen and T. W. B. Kibble, "Global conservation laws and massless particles," *Phys. Rev. Lett.*, vol. 13, pp. 585–587, Nov 1964. [Online]. Available: http://link.aps.org/doi/10.1103/PhysRevLett.13.585

[Har15] F. Harms, "Experimental Study of Background Sources in the KATRIN Main Spectrometer," 2015, Ph.D. thesis in preparation.

[Hig64] P. W. Higgs, "Broken symmetries and the masses of gauge bosons," *Phys. Rev. Lett.*, vol. 13, pp. 508–509, Oct 1964. [Online]. Available: http://link.aps.org/doi/10.1103/PhysRevLett.13.508

[Hig08] H. Higaki, K. Ito, K. Kira and H. Okamoto, "Electrons confined with an axially symmetric magnetic mirror field," *AIP Conference Proceedings*, vol. 1037, no. 1, pp. 106–114, 2008. [Online]. Available: http://scitation.aip.org/content/aip/proceeding/aipcp/10.1063/1.2977830

[Hir87] K. Hirata et al., "Observation of a neutrino burst from the supernova SN1987A," *Phys. Rev. Lett.*, vol. 58, pp. 1490–1493, Apr 1987. [Online]. Available: http://link.aps.org/doi/10.1103/PhysRevLett.58.1490

[Hir88] K. S. Hirata et al., "Observation in the Kamiokande-II detector of the neutrino burst from supernova SN1987A," *Phys. Rev. D*, vol. 38, pp. 448–458, Jul 1988. [Online]. Available: http://link.aps.org/doi/10.1103/PhysRevD.38.448

[Jan15] A. Jansen, "The cryogenic pumping section of the KATRIN experiment - Design studies and experiments for the commissioning," Ph.D. dissertation, Karlsruhe, Karlsruher Institut fuer Technologie (KIT), February 2015.

[JET89] A. Junod, D. Eckert, G. Triscone, J. Müller, and W. Reichardt, "A study of the magnetic transitions in CuO: specific heat (1-330 K), magnetic susceptibility and phonon density of states," *Journal of Physics: Condensed Matter*, vol. 1, no. 43, p. 8021, 1989.

[JS06] A. K. Jain and B. Singh, "Nuclear Data Sheets for A = 218," *Nuclear Data Sheets*, vol. 107, no. 4, pp. 1027 – 1074, 2006. [Online]. Available: http://www.sciencedirect.com/science/article/pii/S0090375206000214

[KAT05] KATRIN collaboration, "KATRIN design report 2004," *FZKA scientific report*, vol. 7090, 2005.

[Kei07] P. Keil, D. Luetzenkirchenhecht, and R. Frahm, "Investigation of Room Temperature Oxidation of Cu in Air by Yoneda-XAFS," *AIP Conference Proceedings*, vol. 882, no. 1, pp. 490–492, 2007. [Online]. Available: http://scitation.aip.org/content/aip/proceeding/aipcp/10.1063/1.2644569

[Kil13] M. Kilbinger et al., "CFHTLenS: combined probe cosmological model comparison using 2D weak gravitational lensing," *Monthly Notices of the Royal Astronomical Society*, vol. 430, no. 3, pp. 2200–2220, 2013. [Online]. Available: http://mnras.oxfordjournals.org/content/430/3/2200.abstract

[KL13] S. F. King and C. Luhn, "Neutrino mass and mixing with discrete symmetry," *Reports on Progress in Physics*, vol. 76, no. 5, p. 056201, 2013.

[Kla01] H. V. Klapdor-Kleingrothaus, A. Dietz,H. L. Harney and I. V. Krivosheina, "Evidence for neutrinoless double beta decay," *Modern Physics Letters A*, vol. 16, no. 37, pp. 2409–2420, 2001. [Online]. Available: http://www.worldscientific.com/doi/abs/10.1142/S0217732301005825

[Kli13] F. Klinkhamer, "Neutrino mass and the standard model," *Modern Physics Letters A*, vol. 28, no. 05, 2013.

[Kod01] K. Kodama et al., "Observation of tau neutrino interactions," *Physics Letters B*, vol. 504, no. 3, pp. 218 – 224, 2001. [Online]. Available: http://www.sciencedirect.com/science/article/pii/S0370269301003070

[KP09] R. Kersevan and J.-L. Pons, "Introduction to MOLFLOW+: New graphical processing unit-based Monte Carlo code for simulating molecular flows and for calculating angular coefficients in the compute unified device architecture environment," *Journal of Vacuum Science & Technology A*, vol. 27, no. 4, pp. 1017–1023, 2009.

[Kra05] C. Kraus et al., "Final results from phase II of the Mainz neutrino mass searchin tritium decay," *The European Physical Journal C-Particles and Fields*, vol. 40, no. 4, pp. 447–468, 2005.

[Kra15] M. Krause, "MOLFLOW+ simulations of radon decays in the main spectrometer," 2015, internal KATRIN talk, 28th collaboration meeting. [Online]. Available: http://fuzzy.fzk.de/bscw/bscw.cgi/d950125/95-TRP-5803-A1.3-MKrause.pdf

[Lat95] R. V. Latham, *High voltage vacuum insulation: basic concepts and technological practice*. Elsevier, 1995.

[Leb10] M. L. Leber, "Monte carlo calculations of the intrinsic detector backgrounds for the karlsruhe tritium neutrino experiment," Ph.D. dissertation, University of Washington, 2010.

[Lid13] A. Liddle, *An introduction to modern cosmology*. John Wiley & Sons, 2013.

[Lin15] J. Linek, "Investigation of the muon induced background at the KATRIN main spectrometer," Master's thesis, Karlsruhe, Karlsruher Institut fuer Technologie (KIT), May 2015.

[LL02] T. J. Loredo and D. Q. Lamb, "Bayesian analysis of neutrinos observed from supernova SN 1987A," *Phys. Rev. D*, vol. 65, p. 063002, Feb 2002. [Online]. Available: http://link.aps.org/doi/10.1103/PhysRevD.65.063002

[Luo06] X. Luo, C. Day, V. Hauer, O. B. Malyshev, R. J. Reid and F. Sharipov, "Monte Carlo simulation of gas flow through the KATRIN DPS2-F differential pumping system," *Vacuum*, vol. 80, no. 8, pp. 864 – 869, 2006. [Online]. Available: http://www.sciencedirect.com/science/article/pii/S0042207X05003891

[MAB13] G. Mukherjee et al., "Nuclear Data Sheets for A = 215," *Nuclear Data Sheets*, vol. 114, pp. 2023–2078, 2013.

[Maj37] E. Majorana, "Teoria simmetrica dell'elettrone e del positrone," *Il Nuovo Cimento*, vol. 14, no. 4, pp. 171–184, 1937. [Online]. Available: http://dx.doi.org/10.1007/BF02961314

[Mak62] Z. Maki, N. Nakagawa and S. Sakata, "Remarks on the unified model of elementary particles," *Progress of Theoretical Physics*, vol. 28, no. 5, pp. 870–880, 1962.

[Mas07] S. S. Masood, S. Nasri, J. Schechter, M. A. Tortola, J. W. F. Valle and C. Weinheimer, "Exact relativistic β decay endpoint spectrum," *Physical Review C*, vol. 76, no. 4, p. 045501, 2007.

[Mei22] L. Meitner, "Über die Entstehung der β-Strahl-Spektren radioaktiver Substanzen," *Zeitschrift fuer Physik*, vol. 9, pp. 131–144, December 1922. [Online]. Available: http://dx.doi.org/10.1007/BF01326962

[Mer12] S. Mertens, "Study of Background Processes in the Electrostatic Spectrometers of the KATRIN Experiment," Ph.D. dissertation, Karlsruhe, Karlsruher Institut fuer Technologie (KIT), February 2012.

[Mer13] S. Mertens et al., "Background due to stored electrons following nuclear decays in the KATRIN spectrometers and its impact on the neutrino mass sensitivity," *Astroparticle Physics*, vol. 41, pp. 52–62, 2013.

[Nob03] Nobelprize.org. Nobel Media AB 2014, "The nobel prize in physics 1903," Web. 6 Apr 2015, 1903. [Online]. Available: http://www.nobelprize.org/nobel_prizes/physics/laureates/1903/

[Oli14] K. A. Olive et al., "Review of Particle Physics," *Chin. Phys.*, vol. C38, p. 090001, 2014.

[Pad12] N. Padmanabhan, X. Xu, D. J. Eisenstein, R. Scalzo, A. J. Cuesta, K. T. Mehta and E. Kazin, "A 2 per cent distance to z= 0.35 by reconstructing baryon acoustic oscillations–i. methods and application to the sloan digital sky survey," *Monthly Notices of the Royal Astronomical Society*, vol. 427, no. 3, pp. 2132–2145, 2012.

[Pau30] W. Pauli, "Offener Brief an die Gruppe der Radioaktiven bei der Gauvereins-Tagung zu Tuebingen"," 1930. [Online]. Available: http://www.symmetrymagazine.org/sites/default/files/legacy/pdfs/200703/logbook_letter.pdf

[Per75] M. L. Perl et al., "Evidence for anomalous lepton production in $e^+ - e^-$ annihilation," *Phys. Rev. Lett.*, vol. 35, pp. 1489–1492, Dec 1975. [Online]. Available: http://link.aps.org/doi/10.1103/PhysRevLett.35.1489

[Pon57] B. Pontecorvo, "Mesonium and antimesonium," *Zh. Eksp. Teor. Fiz.*, vol. 33, 1957.

[Pov14] B. Povh, K. Rith, C. Scholz, F. Zetsche and W. Rodejohann, *Teilchen und Kerne: eine Einführung in die physikalischen Konzepte*. Springer-Verlag, 2014.

[Pra11] M. Prall, "The Katrin experiment and the pre-spectrometer at reduced retarding potential," *Progress in Particle and Nuclear Physics*, vol. 66, no. 2, pp. 418 – 423, 2011, Particle and Nuclear Astrophysics International Workshop on Nuclear Physics, 32nd Course. [Online]. Available: http://www.sciencedirect.com/science/article/pii/S0146641011000457

[RC97] F. Reines and C. Cowan, "The Reines-Cowan Experiments - Detecting the Poltergeist," *Los Alamos Science*, vol. 25, pp. 4–27, 1997. [Online]. Available: http://library.lanl.gov/cgi-bin/getfile?25-02.pdf

[RPD14] S. Riemer-Sørensen, D. Parkinson, and T. M. Davis, "Combining Planck data with large scale structure information gives a strong neutrino mass constraint," *Phys.Rev.*, vol. D89, no. 10, p. 103505, 2014.

[Rut99] E. Rutherford, "VIII. Uranium radiation and the electrical conduction produced by it," *The London, Edinburgh, and Dublin Philosophical Magazine and Journal of Science*, vol. 47, no. 284, pp. 109–163, 1899.

[Sae00] A. Saenz, S. Jonsell and P. Froelich, "Improved molecular final-state distribution of HeT^+ for the β-decay process of T_2," *Phys. Rev. Lett.*, vol. 84, pp. 242–245, Jan 2000. [Online]. Available: http://link.aps.org/doi/10.1103/PhysRevLett.84.242

[Sch09] M. Schloesser, "First Laser Raman measurements with tritium for KATRIN and studies of systematic effects of the LARA-setup," Master's thesis, Diploma thesis, Karlsruhe Institute of Technology, 2009.

[Sch14] J. Schwarz, "The Detector System of the KATRIN Experiment - Implementation and First Measurements with the Spectrometer," Ph.D. dissertation, Karlsruhe, Karlsruher Institut fuer Technologie (KIT), July 2014.

[SD65] S. Szucs and J. M. Delfosse, "Charge spectrum of recoiling $^{216}\mathrm{Po}$ in the α decay of $^{220}\mathrm{Rn}$," *Phys. Rev. Lett.*, vol. 15, pp. 163 – 165, July 1965. [Online]. Available: http://link.aps.org/doi/10.1103/PhysRevLett.15.163

[Sha] "Upper Bound of 0.28 eV on Neutrino Masses from the Largest Photometric."

[Sis04] M. Sisti et al., "New limits from the Milano neutrino mass experiment with thermal microcalorimeters ", journal = "Nuclear Instruments and Methods in Physics Research Section A: Accelerators, Spectrometers, Detectors and Associated Equipment," vol. 520, no. 1-3, pp. 125 – 131, 2004, proceedings of the

10th International Workshop on Low Temperature Detectors. [Online]. Available: http://www.sciencedirect.com/science/article/pii/S0168900203031814

[SM03] E. Süli and D. F. Mayers, *An introduction to numerical analysis*. Cambridge University Press, 2003.

[Sod13] F. Soddy, "The radio elements and the periodic law," *Chem. News*, vol. 107, pp. 97–99, 1913.

[SV15] F. Siddi and P. Vazquez, "Blender," http://www.blender.org/, June 2015.

[Val10] K. Valerius, "The wire electrode system for the KATRIN main spectrometer," *Progress in Particle and Nuclear Physics*, vol. 64, no. 2, pp. 291–293, 2010.

[Wan13] N. Wandkowsky, "Study of background and transmission properties of the KATRIN spectrometers," Ph.D. dissertation, Karlsruhe, Karlsruher Institut fuer Technologie (KIT), July 2013.

[Wei35] C. Weizsaecker, "Zur Theorie der Kernmassen," *Zeitschrift fuer Physik*, vol. 96, no. 7-8, pp. 431–458, 1935. [Online]. Available: http://dx.doi.org/10.1007/BF01337700

[Wu07] S.-C. Wu, "Nuclear Data Sheets for A=216, Nuclear Data Sheets 108 (5) (2007) 1057-1092," pp. 1057–1092, July 2007. [Online]. Available: http://www.sciencedirect.com/science/article/pii/S0090375207000415

[WW95] J. Wetzer and P. Wouters, "HV design of vacuum components," *Dielectrics and Electrical Insulation, IEEE Transactions on*, vol. 2, no. 2, pp. 202–209, 1995.

[Zub11] K. Zuber, *Neutrino physics*. CRC Press, 2011.

7. Appendix

A Important decay chains concerning Radon

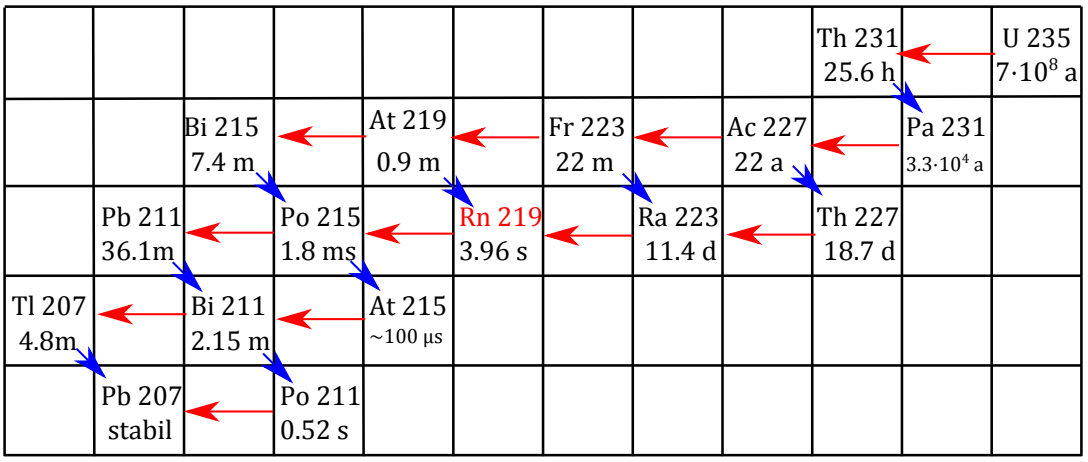

Figure A.1: **Decay chain for ^{219}Rn.** Figure and values adapted from [Goe14]. α-decays are indicated by red arrows while β-decays are indicated by blue arrows.

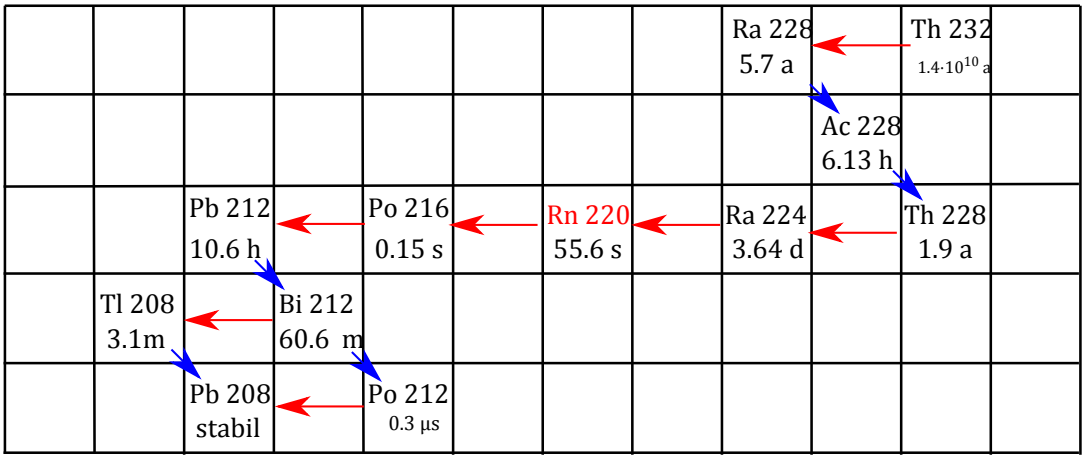

Figure A.2: **Decay chain for ^{220}Rn.** The colors are used as in figure A.1. Figure adapted from [Goe14].

B Positions of the radon source

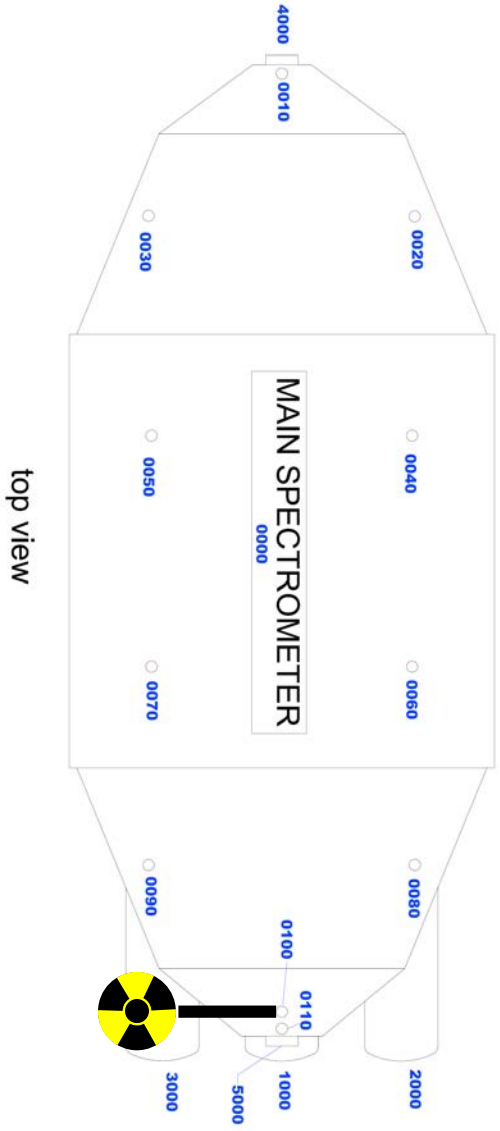

Figure B.3: **The position of the additional radon source when connected to the main-spectrometer vessel.** The radon source is connected to port 100 which is indicated with a symbol for radioactivity. Figure adapted from [Goe14].

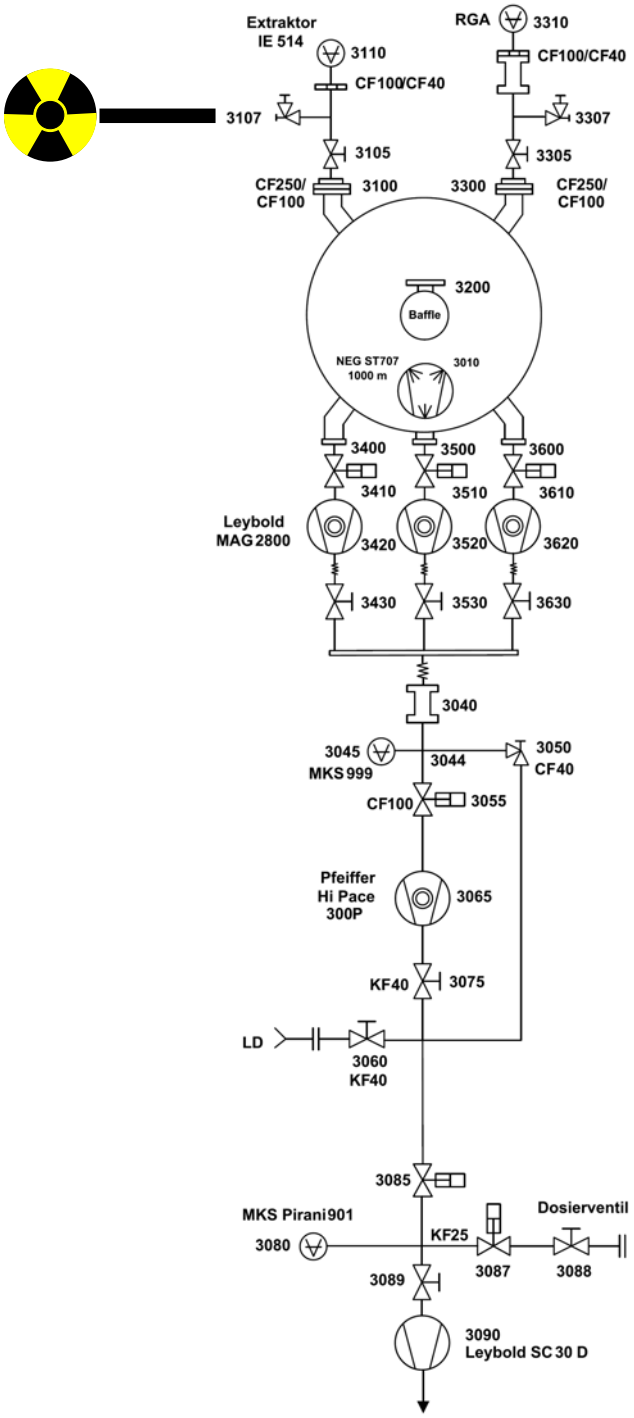

Figure B.4: **The position of the additional radon source when connected to pump port 3 is shown.** The radon source is indicated with a symbol for radioactivity. Figure adapted from [Goe14].

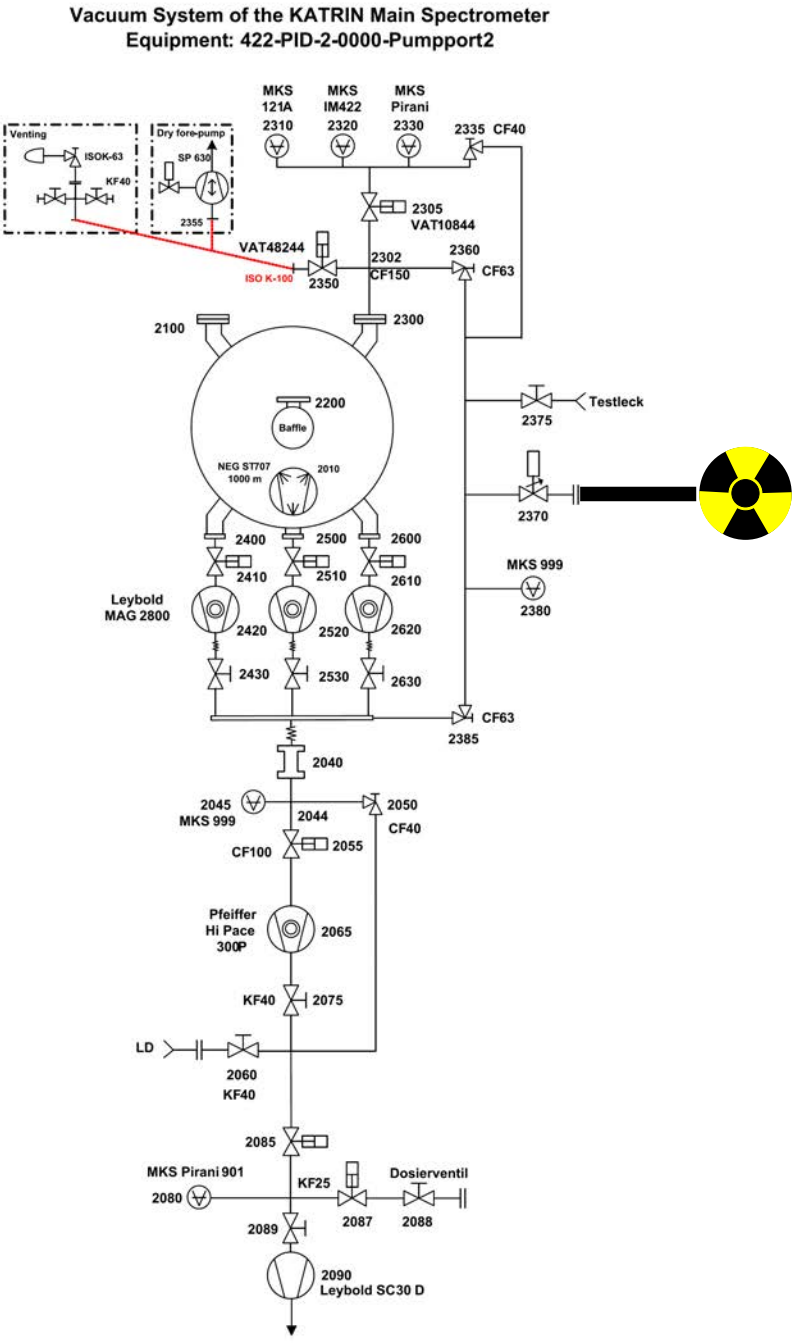

Figure B.5: **The position of the additional radon source when connected to pump port 2 is shown.** The radon source is indicated with a symbol for radioactivity. Figure adapted from [Goe14].

Acknowledgements

Während meiner Masterarbeit wurde ich von vielen Leuten unterstützt. Mein Dank gilt jedem Einzelnen. Insbesondere bedanke ich mich bei:

- Prof. G. Drexlin für die Möglichkeit ein Teil der KATRIN Kollaboration zu sein, für die ansteckende Begeisterung rund um die Neutrinophysik und für die guten Ideen und hilfreichen Diskussionen während der Masterarbeit.
- Prof. T. Müller für die Übernahme der Korreferenz und die unterhaltsamen und lehrreichen Vorlesungen.
- Dr. K. Schlösser für die Übernahme der Betreuung meiner Masterarbeit, die herausragende Betreuung und Hilfe bei den hardwarelastigen Arbeiten, die Korrekturvorschläge, und für seine erhellenden Lebensweisheiten und die Ruhe, die er insbesondere, als der Zeitdruck großwar, ausgestrahlt hat.
- Dipl.-Phys. F. Harms für die hervorragende Organisation und Umsetzung der Messungen des Radon-induzierten Untergrundes während SDS-II, für die Hilfe während dem Einstieg in die Datenanalyse und für gute Vorschläge bei der Analyse.
- Dr. J. Schwarz für die stete Unterstützung bei den vielfältigen Problemen während der Datenanalyse, die Korrekturvorschläge der Masterarbeit, Geduld und vor allem Hilfsbereitschaft.
- Dr. J. Wolf für die Beantwortung von unzähligen Fragen, die unersetzliche Unterstützung bei den Simulationen und die Korrekturvorschläge der Arbeit.
- M. Krause für seine Motivation, Hilfsbereitschaft und die Modifikationen von MOLFLOW+
- Dr. F. Fränkle für die Korrekturvorschläge, seine Ratschläge und Motivation.
- Allen Technikern, insbesondere K. Mehret, H. Frenzel, B. Bender und M. Jäger für die schnelle und zuverlässige Arbeit, insbesondere am HV-Trenner.
- Dr. A. Jansen für die ComSol-Simulationen und die Darts-Spiele
- Dr. S. Goerhardt für die Betreuung des ersten Monats meiner Masterarbeit
- Dr. R. Lietzow für die kurzfristige Bereitstellung der Babcock-Noell Isolatoren
- Dr. U. Thiele, Dr. P. Ranitzsch & Dr. K. Wierman für die Unterstützung beim Testen des HV-Trenners.
- Dipl.-Phys. F. Harms, Dr. K. Schlösser, Dipl.-Phys. D. Hilk und J. Weis für den Einbau der Radon-Quelle.
- Dipl.-Phys. Moritz Erhard & Dipl.-Phys. Marcel Kraus & Oliver Wack für ihre zahllosen Stunden zur Gewärleisung der Hochspannung und der Magnetfelder.
- K. Vogt für Ihre Hilfe rund um technische Zeichnungen
- Dr. T. Tümmler für die Organisation der Messphase

- MSc. Moritz Hackenjos und Dr. F. Fränkle für die gute Büroatmosphäre
- MSc. J. Linek für die Motivation und Unterhaltungen
- Der Eisrunde für die Gespräche, Unterhaltung und gute Laune
- Der gesamten KATRIN-Gruppe für die schöne Zeit.

Besonderer Dank gilt meiner Familie, die mich während meinem gesamten Studium insbesondere in stressigen Zeiten vollkommen unterstützt und motiviert hat und immer für mich da war.